



**HAL**  
open science

# Homogenization of mechanical and thermal properties of fired clay bricks: effects of porosity

Zeye Tian

► **To cite this version:**

Zeye Tian. Homogenization of mechanical and thermal properties of fired clay bricks: effects of porosity. Civil Engineering. INSA de Toulouse, 2018. English. NNT : 2018ISAT0010 . tel-01897937

**HAL Id: tel-01897937**

**<https://theses.hal.science/tel-01897937>**

Submitted on 17 Oct 2018

**HAL** is a multi-disciplinary open access archive for the deposit and dissemination of scientific research documents, whether they are published or not. The documents may come from teaching and research institutions in France or abroad, or from public or private research centers.

L'archive ouverte pluridisciplinaire **HAL**, est destinée au dépôt et à la diffusion de documents scientifiques de niveau recherche, publiés ou non, émanant des établissements d'enseignement et de recherche français ou étrangers, des laboratoires publics ou privés.



# THÈSE INSA TOULOUSE

En vue de l'obtention du

**DOCTORAT DE L'UNIVERSITÉ DE TOULOUSE**

Délivré par :

Institut National des Sciences Appliquées de Toulouse (INSA Toulouse)

---

---

Présentée et soutenue par:

**Zeye TIAN**

Le 28 Juin 2018

Titre:

**Homogenization of mechanical and thermal  
properties of fired clay bricks: effects of porosity**

---

---

École doctorale et spécialité :

MEGEP : Génie civil

Unité de Recherche :

Laboratoire Matériaux et Durabilité des Constructions

## JURY

J. ABSI	Professeur, GEMH, Université de Limoges	Président
J.F. SHAO	Professeur, LML, Université de Lille 1	Rapporteur
A. GIRAUD	Professeur, ENSG, Université de Lorraine	Rapporteur
D. KONDO	Professeur, IJRA, UPMC	Examineur
S. GEOFFROY	Professeur, LMDC, Université Paul Sabatier	Directeur
A. ABOU-CHAKRA	Maître de Conférences, LMDC, INSA Toulouse	Co-directeur



# Acknowledgements

The thesis is finished under the direction of professors Ariane Abou-Chakra and Sandrine Geoffroy. I am willing to thank them for patient guidance and much help in this field.

I would like to thank professor Djimédo Kondo, who provided invaluable suggestions for my thesis and offered me an opportunity of academic exchange in UPMC. His attitude towards pursuing the scientific truth influences me deeply. I express my heartfelt gratitude to professor Jian-fu Shao, professor Albert Giraud and professor Joseph Absi for being the members of my jury. I am thankful to professor Bernard Perrin for giving much advice on the research material. I also thank professor Aurélie Papon for providing helpful guidance on software.

I appreciate my friends Dr. Bin Li, Dr. Yun Huang, Dr. Xiucong Sun, Dr. Yi Wang, Dr. Long Cheng, Dr. Jin Wang, Dr. Peng Jing, Dr. Laila Aouba for helping me during my thesis. I also express my thankful feelings to my colleagues Dr. Aurélie Laborel-Préneron, Dr. Mustapha Sow, Dr. Isabelle Martin, Dr. Ilgar Allahyari, Dr. Nam Nguyen Vu, Dr. Biao Wang, Dr. Linwen Yu, Dr. Xiaoxiao Gao, Dr. Célimène Numaine, PhD Rudy Bui, PhD Souad Bouregaya, PhD Ferdiansyah Teuku, PhD Wulong Zhang, PhD Alexandre Bessa Martins, and many more. We often have funny chatting and activities. I really enjoy the days of living with the international family in the pink city.

I am indebted to my parents for their unconditional support and encouragement. Their love inspires me to challenge and overcome difficulties.

The research is realized by the cooperation project ‘UT/INSA-CSC’. The finance supporting on my research is provided by China Scholarship Council and the work is performed in LMDC. I express my thanks to the two organizations for providing an international research opportunity.



---

**Abstract** — Due to the environmental protection requirement, fired clay bricks are facing new development tendency. Fired clay bricks are not only satisfied with mechanical strength but also rising energy utilization. Thermal conductivity is a very important parameter to measure the energy utilization. On the premise of guaranteeing the basically mechanical properties, reducing thermal conductivity has been one of important development goals in building industry.

Based on the analysis of micro-structure, microscopic pores have an effect on macroscopic elastic constants and thermal conductivity. Parallel micropores resulting from producing methods cause the transverse isotropy of fired clay bricks. However, it is not clear that the influence of micropores on the macroscopic properties. Though some models studied the effect of porosity on mechanical properties of fired clay bricks, these models are empirical and ignored many microscopic information. One of the goals of the thesis is to analyze the influence of shape, orientation and spatial distribution of microscopic factors on mechanical properties and thermal conductivity in order to provide a reference to optimize the micro-structure of fired clay bricks.

Firstly, the relationships between elastic properties and porosity are derived by different homogenization methods. We compare the results from Mori-Tanaka ignoring spatial distribution of micropores and Ponte Castañeda-Willis considering the spatial distribution. We find that the prediction for anisotropy by Ponte Castañeda-Willis estimate is much stronger. Next, the prediction for thermal conductivity is also studied by homogenization technology. Similar conclusions are obtained.

Meanwhile, microcracks widely exist in fired clay bricks and cause the degradation of fired clay bricks. In this thesis, it is assumed that the orientations of microcracks are aligned and the spatial distribution is spherical. We build a micro-mechanical damage model by transforming open microcrack density into a parameter  $d$  to predict the mechanical behavior of fired clay bricks. Experimental validations demonstrate that homogenization technology is reliable to build a link between microscopic structure and macroscopic properties.

**Keywords:** Fired clay bricks, transverse isotropy, homogenization, micropores, microcracks, elastic properties, thermal conductivity, damage



# Contents

<b>Research Context</b>	<b>11</b>
<b>1 The material analysis of fired clay bricks</b>	<b>15</b>
1.1 Raw materials . . . . .	16
1.1.1 Crystal structure . . . . .	16
1.1.2 Types of clay minerals . . . . .	17
1.2 Manufacturing process . . . . .	19
1.3 Additives . . . . .	22
1.3.1 Inert materials . . . . .	22
1.3.2 Pore-forming agents . . . . .	23
1.4 Fired clay bricks . . . . .	24
1.4.1 The constituents of fired clay bricks . . . . .	24
1.4.2 The micro-structure of fired clay bricks . . . . .	26
1.5 The characteristics and properties of fired clay bricks . . . . .	28
1.5.1 The mechanical properties of fired clay bricks . . . . .	28
1.5.2 The thermal conductivity of fired clay bricks . . . . .	31
1.5.3 The transverse isotropy of fired clay bricks . . . . .	32
1.5.4 The effect of porosity on mechanical properties and thermal conductivity of fired clay bricks . . . . .	33
1.6 Conclusions . . . . .	35
<b>2 The effective elastic properties of fired clay bricks</b>	<b>37</b>
2.1 Introduction . . . . .	37

2.2	Basic concepts of micromechanics of materials . . . . .	39
2.2.1	The scale separation of characteristic Scale . . . . .	39
2.2.2	The methodology of micromechanics . . . . .	39
2.3	The representative volume element (RVE) for fired clay bricks . . . . .	40
2.4	Homogenization of the elastic properities . . . . .	41
2.5	Estimates of the effective stiffness tensor . . . . .	44
2.5.1	The Mori-Tanaka (MT) scheme . . . . .	44
2.5.2	The Ponte Castañeda-Willis (PCW) scheme . . . . .	45
2.6	The prediction for the effective elastic properties of fired clay bricks . . . . .	46
2.6.1	The MT estimate of elastic properties . . . . .	46
2.6.2	The PCW estimate of elastic properties . . . . .	50
2.6.3	The comparison of the prediction between MT and PCW schemes . . . . .	51
2.7	Calibrations and experimental validations . . . . .	53
2.8	Conclusions . . . . .	56
<b>3</b>	<b>The effective thermal conductivity of fired clay bricks</b>	<b>59</b>
3.1	Introduction . . . . .	59
3.2	Homogenization for stationary linear thermal conductivity . . . . .	60
3.3	Schemes of the effective thermal conductivity tensor . . . . .	63
3.3.1	The Mori-Tanaka estimate of the thermal conductivity . . . . .	63
3.3.2	The Ponte Castañeda-Willis estimate of the thermal conductivity . . . . .	64
3.4	The prediction for effective thermal conductivity of fired clay bricks . . . . .	64
3.4.1	The effective thermal conductivity tensor by Mori-Tanaka estimate . . . . .	65
3.4.2	The effective thermal conductivity tensor by Ponte Castañeda-Willis estimate . . . . .	67
3.5	The prediction for thermal conductivity and calibrations . . . . .	68

3.5.1	The relationship between thermal conductivity and porosity . . . . .	68
3.5.2	Calibrations and validations for thermal conductivity . . . . .	70
3.6	Conclusions . . . . .	73
<b>4</b>	<b>The micromechanical damage modeling for fired clay bricks</b>	<b>77</b>
4.1	Introduction . . . . .	77
4.2	The representative volume element (RVE) considering microcracks . . . . .	78
4.3	The effective stiffness of cracked fired clay bricks . . . . .	78
4.3.1	The MT estimate for open microcracks . . . . .	80
4.3.2	The MT estimate for closed microcracks . . . . .	81
4.3.3	The PCW estimate for open microcracks of isotropic distribution . . . . .	83
4.3.4	The PCW estimate for closed microcracks of isotropic distribution . . . . .	85
4.4	Thermodynamic potential and state laws . . . . .	87
4.5	The study on parameters of the damage model . . . . .	89
4.5.1	The study on parameter $\eta$ . . . . .	90
4.5.2	The study on parameter $R_0$ . . . . .	91
4.5.3	The study on parameter $f_p$ . . . . .	91
4.5.4	The study on parameter $X$ . . . . .	93
4.5.5	The comparison between PCW scheme and MT scheme . . . . .	94
4.6	Calibrations and experimental validations of the micromechanical model . . . . .	96
4.7	Conclusions . . . . .	98
	<b>Conclusions and perspectives</b>	<b>101</b>
	<b>A Walpole's notation</b>	<b>105</b>
	<b>B Eshelby tensor in linear elasticity</b>	<b>109</b>

<b>C</b>	<b>The calculations of transversely isotropic stiffness tensor</b>	<b>113</b>
C.1	The calculation of elastic stiffness tensor of Mori-Tanaka estimate . . . . .	113
C.2	The calculation of elastic stiffness tensor of Ponte Castañeda-Willis estimate	116
C.3	The calculation of stiffness tensor of Ponte Castañeda-Willis estimate considering damage . . . . .	118
<b>D</b>	<b>Eshelby's problem in linear thermal conduction</b>	<b>123</b>
D.1	The thermal conductivity inclusion problem . . . . .	124
D.2	The second-order hill tensor . . . . .	126
D.3	The inhomogeneity problem . . . . .	127
	<b>Bibliography</b>	<b>129</b>

# List of Figures

1.1	The tetrahedral layer [1] . . . . .	16
1.2	The octahedral layer [1] . . . . .	17
1.3	The image of clay minerals from CTTB (Centre Technique des Tuiles et Briques) . . . . .	17
1.4	The ancient manufacturing process of fired clay bricks [2] . . . . .	19
1.5	The modern manufacturing process of fired clay bricks (from FFTB) . . . . .	20
1.6	SEM image of fired clay bricks at $10\mu m$ scale [3] . . . . .	25
1.7	SEM image of fired clay bricks at $2\mu m$ scale [3] . . . . .	25
1.8	The XRD spectra of fired clay bricks without additives [4] . . . . .	26
1.9	The XRD spectra of fired clay bricks with additives [5] . . . . .	26
1.10	The microstructure of fired bricks produced by extruding [4] (the extruded direction from left to right) . . . . .	27
1.11	The microstructure of fired bricks produced by extruding [4] (the extruded direction normal to the image plane) . . . . .	28
1.12	The stress-strain curve of fired extruded bricks from [6] . . . . .	29
1.13	The stress-strain curve of fired molded bricks from [2] . . . . .	29
2.1	The relationship between peak strength and porosity . . . . .	38
2.2	The prolate micropore in extruded bricks . . . . .	40
2.3	The oblate micropore in moulded bricks . . . . .	41
2.4	The representative volume element for extruded bricks . . . . .	41
2.5	The representative volume element for moulded bricks . . . . .	42
2.6	The spherical distribution with spheroidal inclusions . . . . .	45
2.7	The relationships between elastic constants and porosity by MT estimate . . . . .	49

2.8	The relationships between elastic constants and porosity by PCW estimate	52
2.9	The prediction for Young's modulus of extruded bricks . . . . .	53
2.10	The prediction for Young's modulus of molded bricks . . . . .	53
2.11	The prediction for shear modulus of extruded bricks . . . . .	54
2.12	The prediction for shear modulus of molded bricks . . . . .	54
2.13	The workflow of calibration in <i>modeFRONTIER</i> . . . . .	55
2.14	10% sands . . . . .	56
2.15	5% sands . . . . .	56
3.1	The normalized thermal conductivity of extruded bricks . . . . .	69
3.2	The normalized thermal conductivity of molded bricks . . . . .	69
3.3	The prediction for $\lambda_{33}$ by Ponte Castañeda-Willis scheme . . . . .	70
3.4	The prediction for $\lambda_{11}$ by Ponte Castañeda-Willis scheme . . . . .	70
3.5	The data containing 10% sands (by hot plate apparatus) [7] . . . . .	72
3.6	The data containing 5% sands (by hot plate apparatus) [7] . . . . .	72
3.7	The data containing 10% sands (by NF EN 1745) [7] . . . . .	73
3.8	The data containing 5% sands (by NF EN 1745) [7] . . . . .	73
3.9	The samples fired at 1000°C [3] . . . . .	74
3.10	The samples fired at 1300°C [3] . . . . .	74
4.1	The RVE for extruded bricks at one microscale . . . . .	79
4.2	The penny-shaped microcrack . . . . .	79
4.3	The relation between normalized $E_3$ and $d$ for open microcracks by MT . .	82
4.4	The relation between normalized $G_{23}$ and $d$ for open microcracks by MT .	82
4.5	The relation between normalized $G_{23}$ and $d$ for closed microcracks by MT .	83
4.6	The relation between normalized $E_3$ and $d$ for closed microcracks by PCW	86

4.7	The relation between normalized $G_{23}$ and $d$ for closed microcracks by PCW	86
4.8	The relation between normalized $G_{23}$ and $d$ for closed microcracks by PCW	88
4.9	The stress-strain curves by PCW estimation under different values of $\eta$	90
4.10	The relationships between damage parameter $d$ and the axial strain $E_{33}$	91
4.11	The stress-strain curves by PCW estimation under different values of $R_0$	92
4.12	The relationships between $d$ and the axial strain $E_{33}$ under different $R_0$	92
4.13	The stress-strain curve for different porosity when $\eta = 0.1$	93
4.14	The stress-strain curve for different porosity when $\eta = 30$	93
4.15	The relationship between peak strength and porosity by PCW	94
4.16	The stress-strain curves under $\eta = 30$ and $f_p = 20\%$	95
4.17	The stress-strain curves under $\eta = 0.1$ and $f_p = 20\%$	95
4.18	The stress-strain curves under $\eta = 0.1$ and $f_p = 0$	96
4.19	The comparison between our modeling and experimental results of extruded bricks [6]	97
4.20	The comparison between our modeling and experimental results of molded bricks [2]	98



# List of Tables

1.1	The comparison between several kinds of clay minerals [8] . . . . .	18
1.2	Young's modulus and Poisson's ratio of fired molded bricks [2] . . . . .	30
1.3	The effect of transverse isotropy on thermal conductivity [9] . . . . .	31
1.4	The anisotropic ratio of Young's modulus and compressive strength [8] . .	32
1.5	The anisotropic ratio of Young's modulus and compressive strength [10] .	32
1.6	The anisotropic ratio of Young's modulus and compressive strength [2] . .	33
1.7	The effect of porosity on peak strength [5] . . . . .	34
1.8	The effect of porosity on thermal conductivity [5] . . . . .	34
1.9	The effect of porosity on mechanical properties [11] . . . . .	34
1.10	The effect of porosity on thermal conductivity [11, 12] . . . . .	35
4.1	Parameters of the damage modeling . . . . .	90
4.2	Predictions for peak stress and Young's modulus on different directions . .	97
4.3	Predictions for peak stress and Young's modulus on different directions . .	97
4.4	The comparison between experimental data and modeling results . . . . .	98
A.1	The products of Walpole tensor elements . . . . .	106



# Research Context

As an artificial composite material, transversely isotropic fired clay bricks have kept the top position in building materials for thousands of years. In ancient, green clay bricks were dried in the sun and used to build the wall for a long time. Subsequently, fired clay bricks burnt in a kiln became more and more popular because of better performance. Some fired clay buildings are very time-honored in the world, such as Albi Cathedral in France, the Great Wall in China and the Moscow Kremlin. In the historical course, the components of fired clay bricks are always changing to adapt to the need of construction. In the past, the traditional function of fired clay bricks was just satisfied with mechanical capacity. In France, fired clay bricks have to meet the mechanical standard NF EN 771 concerning masonry elements. Nowadays, under the requirements of sustainable development, it is obvious that the development trend of fired clay bricks is lightweight, low thermal conduction, and so on. In summary, on the premise of guaranteeing the basically mechanical property, reducing energy consumption has been one of important development goals in building industry.

As one of the countries complying with the Kyoto Protocol, France has made a commitment that involves reducing the carbon dioxide emissions of 75% by 2050 (from French national commitments). Fired clay industry, which has cost lots of energy consumption and resources, is confronted with serious challenges in France. As for the manufacture process and application of fired clay products, the fired clay industry still has a great potential to develop. In Europe, more than 700 companies work on the fired clay industry and invest a lot of funds in product development and manufacturing process every year. These measures improve the function of fired clay products and promote the development of fired clay industry. More importantly, the technological progress can reduce emissions of pollutants and energy consumption, and enhance the energy efficiency. According to French thermal regulation RT2012, the product will have to contribute to the reduction of the energy demand fixed at  $50 \text{ kWhEP/m}^2/\text{year}$ . As one of modes of heat transfer, thermal conductivity is a very important index to measure the energy utilization. There have been a lot of studies to reduce the thermal conductivity of fired clay bricks. As is known to us, fired clay bricks is a porous material containing lots of voids at the micro-scale. Due to the low thermal conduction of voids, researchers are devoted to mixing pore-forming agents with clay together in order to develop new types of fired clay bricks [3, 7, 13]. For example, the project 'Bioclay' from the cooperation of TERREAL (a manufacturer of fired clay), ARTERRIS (an agricultural cooperative) and other laboratories (ARMINES, LCA and LMDC) focuses on developing new types of fired clay bricks mixed with agricultural products and by-products [11, 14]. On one hand, these plants can be burnt during the firing process and increase porosity of fired clay. On the other hand,

these additives can be decomposed and release space occupied by particles to provide the micro-structure and properties we want. In a word, the research goal is to reach a compromise between mechanical and thermal performance. These experimental studies make it possible to validate the relationship between macroscopic behavior and their microscopic characteristics. Now that the macroscopic properties of fired clay bricks can be regulated by changing their micro-structure, the optimization of micro-structure is an issue to reach the best compromise between mechanical and thermal properties. As mentioned above, lots of researchers are interested in this topic, but most work on experiments and few on macroscopic empirical modeling [11, 14] which didn't build a link between macroscopic behavior and micro-structure together. Studying a micro-macro link to predict the properties of fired clay bricks is the research goal in this thesis.

According to the analysis of micro-structure and experimental results from other researchers [4, 7, 11, 13, 14, 15], it is seen that the effective stiffness and thermal conductivity depend on the volume fraction, geometric shape and spatial distribution of each components. So it is feasible to control the effective stiffness and thermal conductivity by selecting proper additives or improving producing technology. To help engineers find a optimum solution between mechanical property and thermal conductivity, building the theoretical modeling to predict the mechanical property and thermal conductivity with the variation of porosity is quite essential.

In the Chapter 1, we focus on the analysis of fired clay material. At first, the crystal structures of clay minerals determining the layer characteristic are introduced based on others' research. Next, the producing processes for extruded and molded bricks are expounded. The transversely isotropy of clay bricks is brought in the shaping step. Then, for new types of bricks, a variety of additives are briefly summarized from others' research. Subsequently, the constituents and micro-structure of fired clay bricks are detailed analyzed on the basis of others' experiments [3, 4]. Lastly, experimental results containing porosity and anisotropy are summarized in tables.

In Chapter 2, the prediction for elastic properties of fired clay bricks is studied. According to micro-structure, a simplified representative volume element is presented. Two homogenization methods are applied to predict the 5 independent elastic constants. The difference of the two methods are compared. Parameter calibrations and experimental validations are implemented to highlight the advantage of homogenization.

The prediction for thermal conductivity will be demonstrated in the Chapter 3 of the thesis. The Eshelby problem of linear conduction is briefly explained at first. Secondly, three homogenization methods are introduced and applied to the prediction of thermal conductivity. Parameter calibrations and experimental validations are studied.

In the production process of fired clay bricks, lots of micro-cracks can generate and

will grow in the process of serving. The existence and evolution of micro-cracks could cause the degradation of mechanical properties. So the influence of micro-cracks on elastic properties and mechanical behavior of fired clay bricks is studied in the Chapter 4. A micro-mechanical damage modeling of transversely isotropic fired clay bricks considering micro-cracks is built by homogenization scheme under the framework of energy dissipative mechanism in the thesis.

The prediction of the multi-physics phenomena which determine the behavior of porous materials is a crucial technological problem for building materials. The aim of the research project is to build tools to predict the multi-physics phenomena which determine the behavior of porous materials such as fired clay bricks and to help designers to reach performances referring to physical or mechanical characteristics.



# The material analysis of fired clay bricks

---

## Contents

<b>1.1</b>	<b>Raw materials</b> . . . . .	<b>16</b>
1.1.1	Crystal structure . . . . .	16
1.1.2	Types of clay minerals . . . . .	17
<b>1.2</b>	<b>Manufacturing process</b> . . . . .	<b>19</b>
<b>1.3</b>	<b>Additives</b> . . . . .	<b>22</b>
1.3.1	Inert materials . . . . .	22
1.3.2	Pore-forming agents . . . . .	23
<b>1.4</b>	<b>Fired clay bricks</b> . . . . .	<b>24</b>
1.4.1	The constituents of fired clay bricks . . . . .	24
1.4.2	The micro-structure of fired clay bricks . . . . .	26
<b>1.5</b>	<b>The characteristics and properties of fired clay bricks</b> . . . . .	<b>28</b>
1.5.1	The mechanical properties of fired clay bricks . . . . .	28
1.5.2	The thermal conductivity of fired clay bricks . . . . .	31
1.5.3	The transverse isotropy of fired clay bricks . . . . .	32
1.5.4	The effect of porosity on mechanical properties and thermal conductivity of fired clay bricks . . . . .	33
<b>1.6</b>	<b>Conclusions</b> . . . . .	<b>35</b>

---

As mentioned in research context, improving macroscopic properties by changing micro-structural information has been the development trend of new types of fired clay bricks. Because the micro-structural information is affected by the whole production process and constituents, it is necessary to analyze and understand this material of fired clay bricks before studying the effect of micro-information on their macroscopic properties. In this chapter, the crystal structure of clay minerals are introduced firstly. Secondly, the ancient

and modern manufacturing processes are depicted in detail. During the firing process, clay minerals can occur physical and chemical reactions and can be transformed into a ‘glassy’ ceramic material. In shaping step, both extrusion and pressing will cause the transversely isotropy of fired clay bricks. Next, many kinds of additives are summarized by literature. In modern, many new types of additives are mixed with clay minerals in order to produce new types of fired clay bricks. Then, the micro-information and macro-properties of fired clay bricks are analyzed, including components, micro-structure, macroscopic mechanical and thermal properties, as well as influence factors. From mechanical experiments, fired clay bricks are the elastic-brittle material. Lastly, some points in our research are concluded.

## 1.1 Raw materials

As one of the most abundant natural resources on the earth, clay minerals are formed by the weathering of rocks under the physical and chemical erosion over a long period of time. Clay minerals are hydrous aluminium phyllosilicates containing different ions, such as silicon, aluminium, oxygen and hydroxyl ions. The ‘phyllo-’ means that the minerals exist in the form of sheets.

### 1.1.1 Crystal structure

The feature of crystal structure of these minerals is a two-layered structure [16]. The tetrahedral layer is composed of 1 silicon atom and 4 oxygen atoms around the silicon atom Figure 1.1. The octahedral layer is based on the gibbsite. The octahedral has 6 hydroxyl ions and a central aluminium ion. Clay minerals are constituted of tetrahedral layer or octahedral layer connected each other (Figure 1.2).

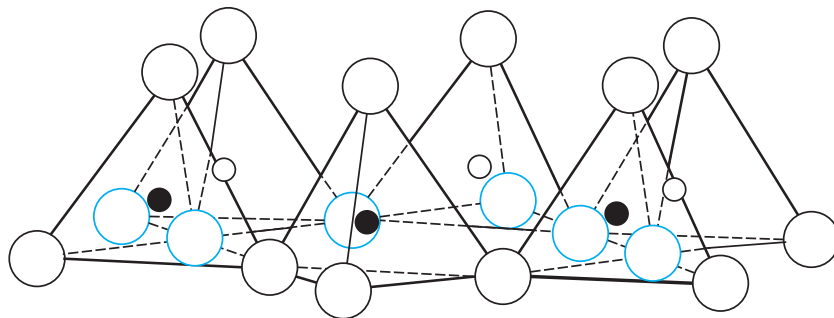


Figure 1.1: The tetrahedral layer [1]

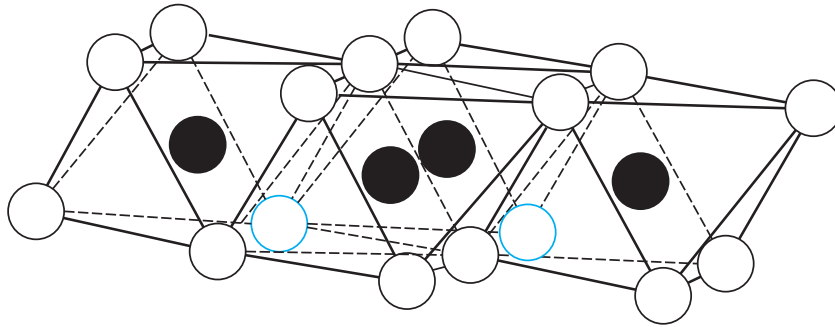


Figure 1.2: The octahedral layer [1]

For clay minerals generated from fragment rocks, the shapes of crystals may be plateplet, discoideus, plate-like or sheet. In the Figure 1.3, the micro-structure of layer of clay minerals is observed by SEM.

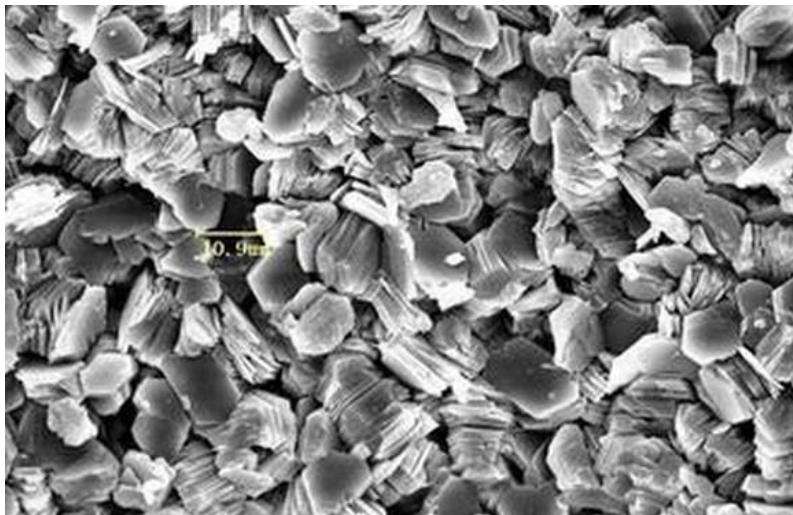


Figure 1.3: The image of clay minerals from CTTB (Centre Technique des Tuiles et Briques)

### 1.1.2 Types of clay minerals

Due to the variability of crystal structures, it is demonstrated that more than 80 kinds of clay minerals exist in the world [8]. In this chapter, we only introduce several widely distributed clay minerals.

## Kaolinite

The equivalent chemical formula is  $2SiO_2 \cdot Al_2O_3 \cdot 2H_2O$ . Kaolinite is the mineral composed of two layers of T-O. The thickness of the sheet is at  $7.2\text{\AA}$ . The configuration of kaolinite is very stable, so the kind of clay mineral can't expand after absorbing water. Kaolinite has a good plasticity, and low shrinkage during drying and firing steps. So kaolinite needs high fired temperature during the firing process, and has the excellent refractory performance after fired.

## Smectite

Smectite is the mineral composed of three layers of T-O-T. The thickness of the sheet is between  $10\text{\AA}$  and  $21\text{\AA}$ . Because of the strong ability of ion exchanging, smectite has the high plasticity, the water absorption, the heavy shrinkage and expansion.

## Illite

Illite is the clay mineral that consists of T-O-T layer. The thickness of the structure is a constant at  $10\text{\AA}$ . Illite is the most widely distributed clay mineral on the earth, and also the most popular material in the fired clay industry. Because of rich potassium  $K$  in illite, the initial melt temperature is not high, approximately  $1050^\circ\text{C}$ .

## Chlorite

Like illite, chlorite is the compound of the layer structure T-O-T. Chlorite is also widely used in the clay industry. The exchange capacity of ion is limited, and the thickness of the structure is static at  $14.1\text{\AA}$ .

The following Table 1.1 shows the comparison of basic information from different clay minerals.

Mineral	Layer	Thickness ( $\text{\AA}$ )	The cation exchange capacity, mol(+)/kg	Expansion capacity	Specific surface ( $m^2/g$ )
Kaolinite	TO	7	3~15	Never	5~20
Smectite	TOT	10~21	80~150	Strong	700~800
Illite	TOT	10	10~40	Weak	50~200
Chlorite	TOT	14.1	10~40	Never	5~20

Table 1.1: The comparison between several kinds of clay minerals [8]

## 1.2 Manufacturing process

Because the advantage of wide distribution and easy extraction of clay minerals, clay bricks are the most oldest and popular construction materials. Long before, clay bricks were shaped by a mold and hardened by drying in the sunshine. Then these dried bricks (unfired bricks) were directly used to build constructions. Later, fired clay bricks appeared with the advent of kilns. At that time, the manufacture of fired clay bricks mainly depended on the labor. After the invention of machines, the process of the production of fired clay bricks come into the mechanization age. Generally speaking, the production process of fired clay bricks contains 5 steps: (1) Extraction (2) Preparation (3) Shaping (4) Drying (5) Firing.

In ancient, fired clay bricks were produced manually, as shown Figure 1.4. In autumn, man extracted clay minerals in the open air. Then the clay minerals were kept in storage in winter. In spring, the clay would be crushed and mixed with water. Because these clay minerals have the good plasticity, they would be put into mold to shape. After the shaping step, it is necessary to drive off water for these shaped bricks in the sunshine. In fact, clay bricks will have shrinkage about 5% during drying, so man will put some leaning agent to diminish the shrinkage. At last, dried bricks would be put into the kiln to make green bodies into ceramic materials.

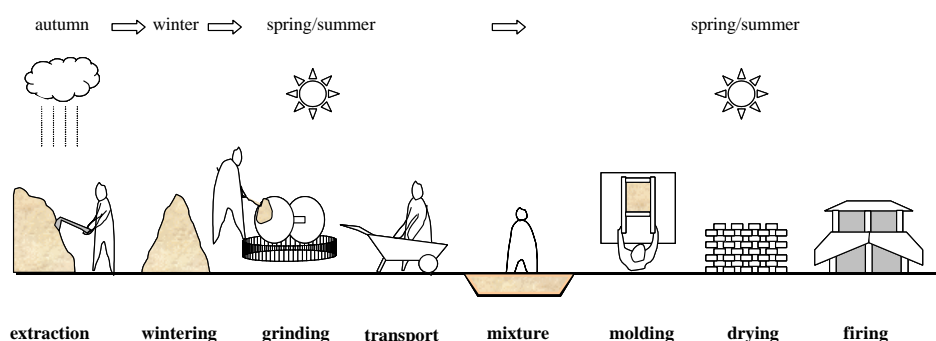


Figure 1.4: The ancient manufacturing process of fired clay bricks [2]

In modern, the production process of fired clay bricks are operated by a series of auto-machines. A simplified flow diagram of production process from FFTB (Fédération Française Tuiles et Briques) is depicted in Figure 1.5. Compared with the old manufacturing method, the modern technology of producing bricks is automatic, which contributes to saving more personal labor and making the process more effective and ecologic. The modern manufacturing process of fired clay bricks will be explained in the following paragraphs.

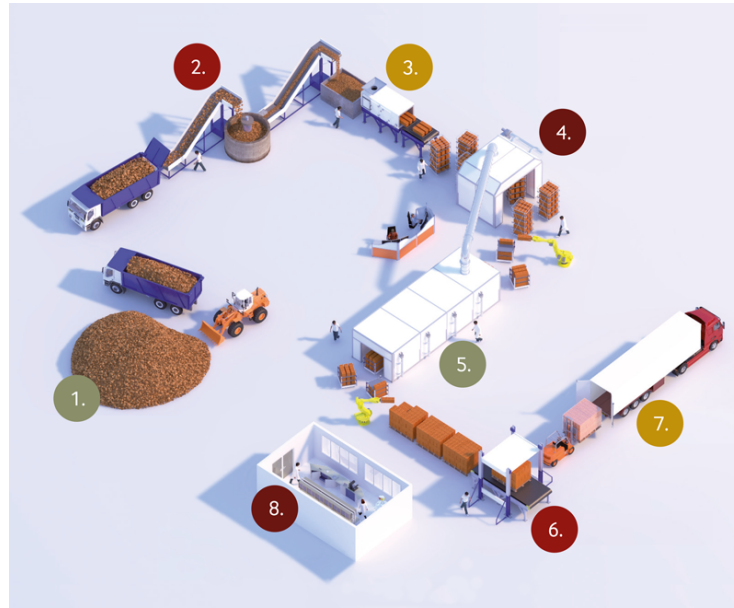


Figure 1.5: The modern manufacturing process of fired clay bricks (from FFTB)

### 1. Extraction

Unlike ancient producing methods, clay minerals are exploited and collected by machines in the open air. Subsequently, these minerals will be put in trucks and transported to factories.

### 2. Preparation

The preparation of raw materials is very important. In order to produce qualified clay bricks, the requirement of characteristics of clay minerals must comply with the national standard, such as the particle size, water content, and so on.

- To eliminate impurities, such as grass, tree roots, and so on.
- To smash clay minerals to get appropriate sizes of clay particles.
- To analyze physical and chemical compositions of clay minerals.
- To mix water and additives with clay homogeneously.

Firstly, clay minerals are screened and impurities are eliminated. Then clay materials are transported to a separator in order to remove out oversize particles. The crusher can smash clay particles to make their size smaller. Lastly, clay particles having the qualified size are transported into a storage to mix with water and additives.

### 3. Shaping

Most clay bricks are shaped by an extruder, however, some kinds of bricks are shaped by a pressing mold.

In the extrusion step, raw materials are sent into shaping workshop and grind. Then they are mixed appropriate amount of water before transporting into a vacuum extrusion machine. If we obtain the qualified plasticity, these mixtures will be sent into the extrusion machine. In the extrusion machine, wet green bodies are formed and extruded according to our demand. Due to the pressure direction in a vacuum machine, extruded bricks possess the oriented properties. For the directionality, it will be explained in the later part of this chapter.

For molding, a green body is shaped in a mold which is usually made from woods or metal. In general, this method demands that raw materials keep low water content. These mixtures are put into a mold and compressed with a metal tool at an appropriate compressive load. Similarly, the molding method can also lead to the transverse isotropy of bricks.

#### 4. Drying

Drying is a quite important step for producing fired bricks. If we want to get the high quality of fired clay products, we must finish this step cautiously. There is about 15% ~ 30% water (the data is based on the mass percentage of dry matter, called dry weight) in the green body before firing, so it must be dried to drain most moisture off. If moisture can't be removed, the water will steam so quickly that lots of microcracks will generate in the firing step. After dried, the content of water in the green body should be smaller than 1% ~ 2%.

#### 5. Firing and cooling

A green body from drying chamber doesn't possess the ceramic performance. The green body must be fired around 1000°C for 10 ~ 40 hours to obtain satisfactory characteristics. The fired temperature and fired time are also dependent on the types of kilns. The most common type of kiln is the tunnel kiln, followed by the periodic kiln. For fuels, the most popular fuels are mainly natural gas, then LPG (liquefied petroleum gas) and heavy fuel oil. Generally speaking, Light-colour fired clay products require higher firing temperature than dark-colour ones. So we have to rigidly control some parameters about firing process, such as the firing temperature, firing time, and so on.

During the firing process, complex physical and chemical reactions will occur between different compositions [17]. Most solid components will turn into glassy matrix. The 'glassy' phase, which may account for more than half of the total mass of the fired brick, provides the bond for the coarse and fine aggregates. All the solid phases, together with micropores constitute the complex microstructure of a fired clay brick with specific mechanical

and physical properties. [18] studied the effect of fired temperature on the microstructure of clay minerals. They found that higher fired temperature can generate stronger glassy phase, and micropores in glassy matrix start to sphere. For the microstructure of fired clay bricks, we will analyze in detail later.

After the firing temperature arrives at the maximum and is kept for a prescribed time, fired clay products go into the cooling stage. Cooling time of products depend on the type of kilns. Like firing temperature, the rate of cooling also has an evident effect on the color of products. During cooling process, the transform of quartz can cause fissures. So in order to avoid fissures, the reduction of the cooling speed is quite essential.

## 6. Storage

After getting fired products, the storage of fired clay bricks is necessary to keep high quality of fired products. The fired bricks should be far away from moist environment, the large difference in temperature and strongly corrosive conditions. The bricks should be placed on a solid, hard-to-water surface on the ground. To prevent collapse, the height of stacked bricks should not be too high. In addition, fired clay bricks should be put into engineering sites as soon as possible.

## 7. Transportation

Fired bricks should be avoided colliding and dumping in the transportation.

## 8. Construction

In the last step, fired clay bricks are applied to constructions as showed in Figure 1.5.

# 1.3 Additives

## 1.3.1 Inert materials

Clay minerals usually have high plasticity, which brings out many difficulties (the slow drying speed, the strong shrinkage in the drying step) in the manufacturing process. It is necessary to put some inert and non-plastic materials in the clay mixtures in order to give off the gas and reduce the shrinkage in the drying step and firing step. Importantly, these inert materials still keep inert in high temperature, and reduce the phenomena of ‘black heart’ in the inner of fired clay bricks. The inert materials mostly used in fired clay bricks are:

1. Sands.

In modern technology, sands are the necessary additive to improve the production process of fired products. Generally speaking, the sizes of sands are  $0.2 \sim 1.0$  mm.

## 2. Chamotte.

Chamotte usually refers to smashed fired clay wastes. This kind of additives enhance the ability to resist thermal effect, and reduce thermal expansion.

Other inert materials are pulverized ash, smashed rocks, and so on.

### 1.3.2 Pore-forming agents

Engineers or researchers always take many measures to reduce the thermal conductivity so as to raise the energy utilization in clay industry. Meanwhile, they also try to reduce the weight and cut the cost of products. The use of pore-forming agents is one of the most popular methods to increase porosity and improve performance of new fired clay bricks now [19, 20]. During firing process, pore-forming agents are burnt, some of which become micropores, some are burnt into residues mixing with glassy phase. Considering the environmental problems and sustainable development, recycling industrial and agricultural waste is energetically advocated to save sources and reduce emission. There are two types of pore-forming agents: renewable resources and mineral resources. The details for the two resources will be explained in the following paragraphs.

#### 1. Renewable resources

Because lots of residues from the industry and agriculture are not properly disposed, applying residues for the fired clay industry is a quite practicable method. The advantage of these residues are low cost, large quantities and environmentally friendly. Most importantly, the experimental results for fired bricks mixed with renewable resources are optimistic. This type of additives can burn, give off  $CO_2$  and create micropores during the firing step. Especially, more and more organic wastes are incorporated with clay to produce new bricks. [21] and [22] have published their reviews for pore-forming agents applied for fired clay industry, in which the author thoroughly summarizes a variety of types of renewable or mineral wastes.

(1) Agricultural wastes. Lots of agricultural wastes have been used for clay industry, such as wheat straw [7], rice husk [23, 24], rice husk ash [24], sunflower seed shell [25], and so on.

(2) Industrial wastes. This type of wastes have also been incorporated into clay products, such as waste marble powder [15], coffee grounds [26], resinous wood fibers [27], sludge [28], spent grains [29], tobacco waste [30], and so on.

## 2. Mineral resources

The mineral resources are also used to improve the performance of fired products and create micropores, but sometimes give off polluted gas. In addition, more mineral residues are needed to achieve the same performance of fired products compared with those from renewable resources. These different additives can be: Ashes and dust [31, 32], Marble residues [33, 34], Phosphogypsum [35], Waste glass [36, 37]. Other additives are perlite, vermiculite, diatomite [38, 39, 40], which will occur thermal expansion during firing process.

Using pore-forming agents can generate some problems: (1) additives can reduce the plasticity of green bodies. (2) Agents containing water can increase the water content of green bodies. (3) The using of agents can reduce the mechanical property of fired products. So how to produce better products requires that researchers keep exploring.

Besides those materials mentioned above, there are still other additives used to improve the performance of fired clay bricks.  $MnO_2$  and  $TiO$  are used to adjust the color of products.  $CaO$  is used to reduce the water content of green bodies.  $Na_2CO_3$  and  $Na_3PO_4$  are used to improve the plasticity.  $BaCO_3$  is used for improving the phenomenon of efflorescence.

## 1.4 Fired clay bricks

At high fired temperature, a series of chemical and physical reactions occur in clay bricks, which causes the change of density, porosity, micro-structure, size of pores, etc. As a porous composite material, the study on inner constituents and micro-structure is quite necessary to understand the link between microscopic information and macroscopic properties. The constituents and micro-structure of fired clay bricks will be presented in the following subsections.

### 1.4.1 The constituents of fired clay bricks

By scanning electron microscope (SEM), we can find that the constituents of fired clay bricks are made up of fired clay (also named ‘glassy’ matrix), unfired silts and sands, other residues. Figure 1.6 is the SEM image of fired clay brick at the scale of  $10\mu m$ . It is clear that there are many micro-voids exist in the solid phases. Figure 1.7 is the image of the solid phase of fired clay bricks at  $2\mu m$  scale, which obviously displays the glassy characteristic of fired clay.

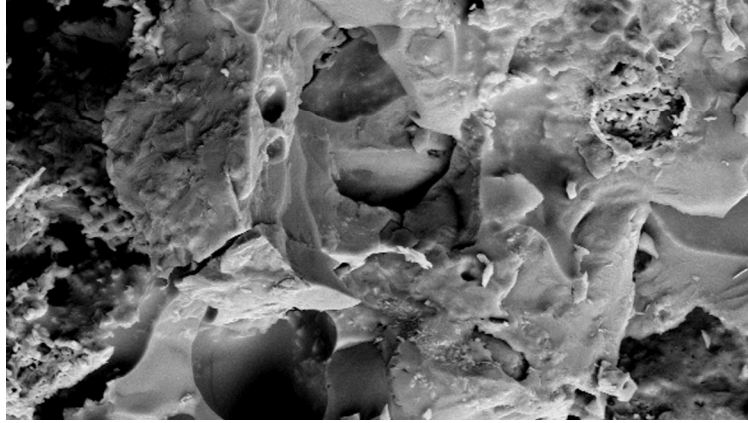


Figure 1.6: SEM image of fired clay bricks at  $10\mu m$  scale [3]

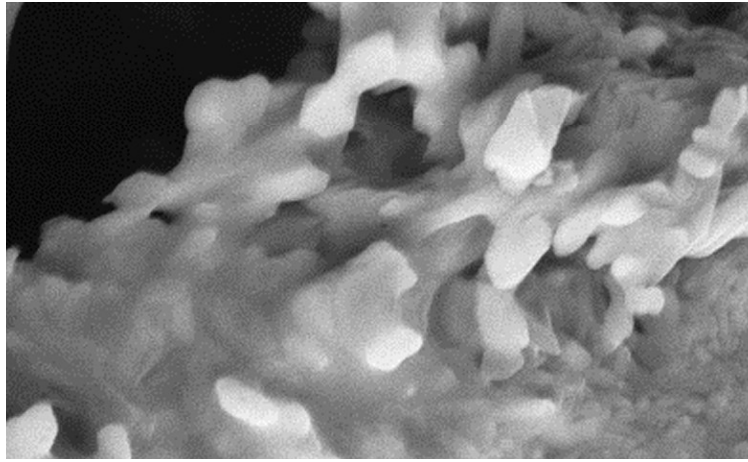


Figure 1.7: SEM image of fired clay bricks at  $2\mu m$  scale [3]

[4] studied the phase identification of fired clay bricks without additives under different fired temperatures in Figure 1.8. The XRD spectra was collected in the  $2\theta$  intervals from  $10^\circ \sim 70^\circ$ , in which the fired temperature of B1 sample is higher than that of B2 sample. Besides studying on those without additives, [5, 13, 15] also analyzed the constituents of fired bricks with additives (paper residues, expanded vermiculite, waste marble powder). The XRD spectra of fired clay bricks with different content of paper residues were obtained in the  $2\theta$  intervals from  $5^\circ \sim 55^\circ$ , shown in Figure 1.9. From the two diagrams, it can be concluded that fired clay bricks without additives are mainly composed of quartz, feldspar and K-feldspar after firing, even if their raw materials may be from different kinds of clay minerals. These amorphous glassy phases form the backbone of fired bricks. The content of noncrystalline solid phases can increase at higher temperature. From Figure 1.9, the constituents of fired clay bricks with additives are still mainly quartz and hematite, but a small part of anorthite and gehlenite which are dependent on additives.

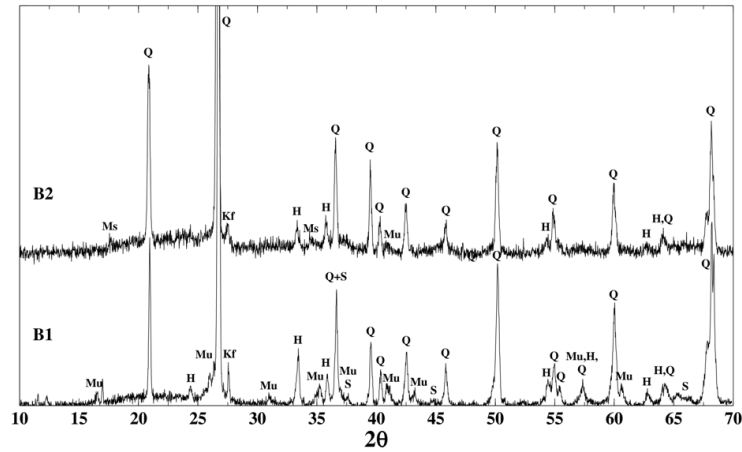


Figure 1.8: The XRD spectra of fired clay bricks without additives [4]

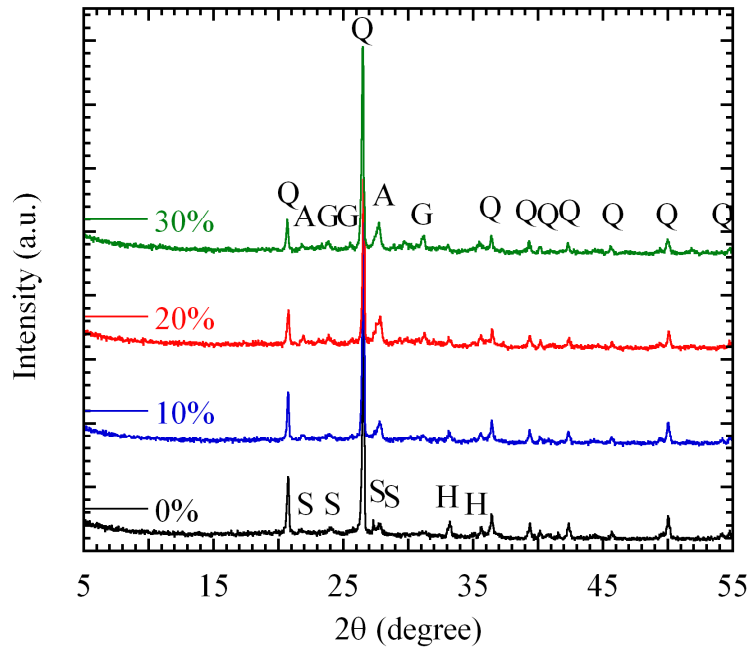


Figure 1.9: The XRD spectra of fired clay bricks with additives [5]

### 1.4.2 The micro-structure of fired clay bricks

As explained above, fired clay bricks are mainly composed of solid glassy phase and micropores. We focus on the analysis of the micro-structure now. In general, the properties of fired bricks are not isotropic, because each product can memorize the mode of production (extruding or molding) which can cause different shapes, orientations or distributions of micropores. Micropores are generated in the production process and possess the oriented

feature. In the states of drying and baking, the transverse isotropy of fired clay bricks will be retained [8].

To some extent, the constituents of fired bricks can be regarded as homogeneous at a relatively large observed scale. However, the material can also be seen as heterogeneous at a smaller observed scale. This is the multi-scale phenomenon of fired clay bricks, which has been showed in [4]. [4] studied the micro-structure of extruded clay bricks by SEM, EDX and MIP. In Figure 1.10, the author found that extruded clay bricks possessed a hierarchical micro-structure due to different neo-crystals. The solid system of crystallization phases forms the backbone for macroscopic performance of the bricks. It is apparent that the micropores (black area) has an obvious orientation (from left to right), which is the same as extruded direction. These micropores are approximately prolate ellipsoidal and the orientation of the major axes of micropores are parallel to the extruded direction at the  $50\mu m$  scale. Then we can see Figure 1.11, the microscopic SEM image of fired bricks whose extruded direction is normal to the paper surface. In this figure, micropores is randomly orientated. Summarizing the two figures, that is the reason why the properties of extruded clay bricks are transversely isotropic.

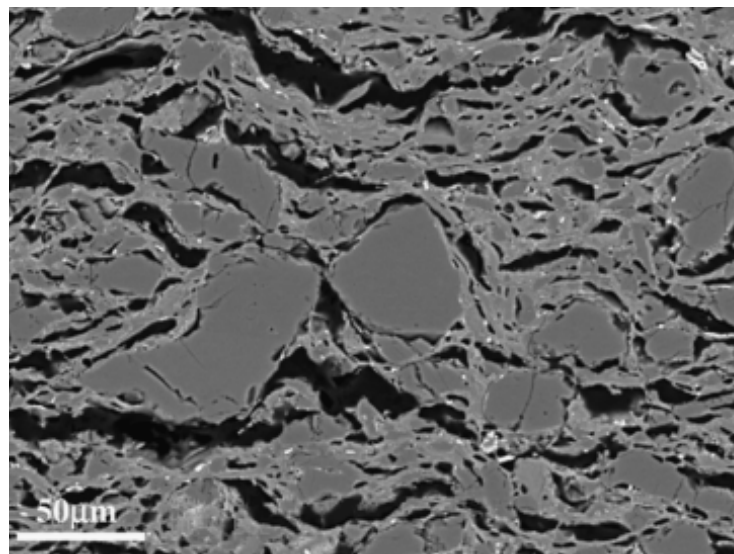


Figure 1.10: The microstructure of fired bricks produced by extruding [4] (the extruded direction from left to right)

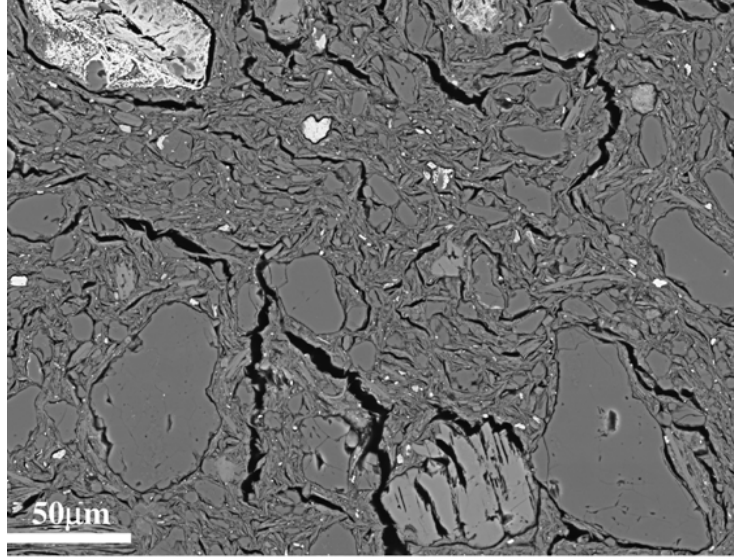


Figure 1.11: The microstructure of fired bricks produced by extruding [4] (the extruded direction normal to the image plane)

## 1.5 The characteristics and properties of fired clay bricks

After the discussion on the micro-structure of fired clay bricks, their physical characteristics, mechanical and thermal properties will be sketched in this part. Firstly, mechanical properties and thermal conduction of fired clay bricks are introduced based on experimental results. Subsequently, as observed in SEM images, the porous structure and the orientation of micropores are very important characteristics of fired clay bricks. The effects of anisotropy and porosity on properties are summarized.

### 1.5.1 The mechanical properties of fired clay bricks

#### 1. The mechanical behavior of fired clay bricks

The uniaxial compressive property of fired clay bricks is the basically mechanical property, which is the foundation of studying the capacity and deformation of masonry structures. The stress-strain relationship of fired clay bricks is the reflection of macroscopic mechanical properties, such as the peak strength or the ultimate deformation.

[6] studied the uniaxial compressive experiments of fired extruded bricks and got the load-unload curves shown in Figure 1.12. It is obvious that fired clay bricks are brittle

materials, and the cyclic behavior allows to highlight the degradation of elastic modulus. The peak strength and the fracture strength are the same. Before getting to the peak point, the stage between the initial point and the peak point is almost linear except for so-called compression process. After the peak point, the strength sharply decreases.

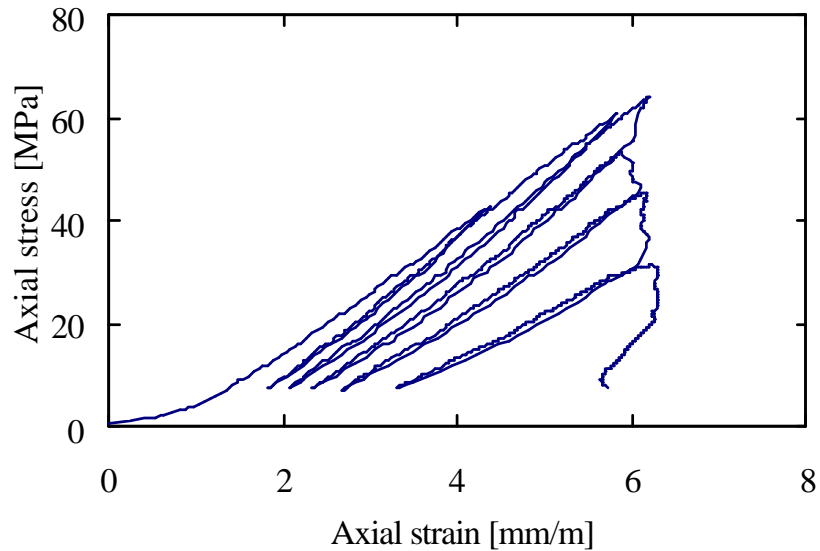


Figure 1.12: The stress-strain curve of fired extruded bricks from [6]

[2] studied the mechanical behavior of fired molded bricks under the uniaxial compressive loading. The curves in the right part result from the direction of the uniaxial loading. The curves show the linear behavior up to 50% of peak stress. After the linear stage, the modulus decreases as the increase of strain.

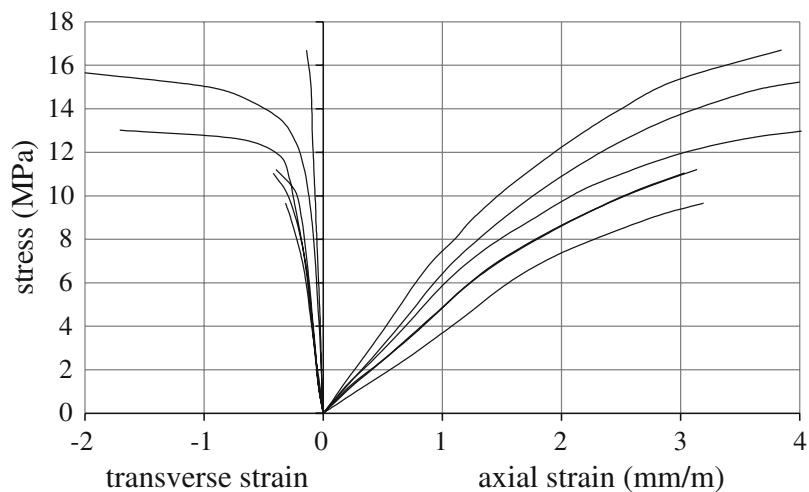


Figure 1.13: The stress-strain curve of fired molded bricks from [2]

## 2. Elastic modulus and Poisson's ratio

Elastic modulus is used to evaluate elastic deformation of fired clay bricks under the load. In principle, Young's modulus under pressure is similar to that under tension in isotropic material. For anisotropic material, there are 9 different elastic moduli: 3 Young's moduli, 3 Poisson's ratios and 3 shear moduli. Due to the extruded or pressed direction, extruded and molded bricks are transversely isotropic materials and possess 5 independent elastic constants [8]. In engineering notation, the stress-strain relationship can be shown by the transversely isotropic stiffness matrix:

$$\begin{pmatrix} E_{11} \\ E_{22} \\ E_{33} \\ 2E_{23} \\ 2E_{13} \\ 2E_{12} \end{pmatrix} = \begin{pmatrix} \frac{1}{E_1} & -\frac{\nu_{12}}{E_1} & -\frac{\nu_{31}}{E_3} & 0 & 0 & 0 \\ -\frac{\nu_{12}}{E_1} & \frac{1}{E_1} & -\frac{\nu_{31}}{E_3} & 0 & 0 & 0 \\ -\frac{\nu_{13}}{E_1} & -\frac{\nu_{13}}{E_1} & \frac{1}{E_3} & 0 & 0 & 0 \\ 0 & 0 & 0 & \frac{1}{G_{23}} & 0 & 0 \\ 0 & 0 & 0 & 0 & \frac{1}{G_{23}} & 0 \\ 0 & 0 & 0 & 0 & 0 & \frac{1}{G_{12}} \end{pmatrix} \begin{pmatrix} \Sigma_{11} \\ \Sigma_{22} \\ \Sigma_{33} \\ \Sigma_{23} \\ \Sigma_{13} \\ \Sigma_{12} \end{pmatrix} \quad (1.1)$$

where  $E_{ij}$  ( $i, j = 1, 2, 3$ ) represents the macroscopic strain and  $\Sigma_{ij}$  the macroscopic stress.

[2] studied on Young's moduli and Poisson's ratios of fired molded bricks, showed in Table 1.2. The difference of tests on three samples is the position of strain gauges. All of them are applied by a load on the 2-axis. The strains  $\varepsilon_{11}$  and  $\varepsilon_{22}$  are measured in Sample 1 and 2 both of which are parallel experiments. For Sample 3, the strains  $\varepsilon_{22}$  and  $\varepsilon_{33}$  are measured in order to obtain Poisson's ratio  $\nu_{23}$ .

Sample ( $N^\circ$ )	1	2	3	Mean value
Peak strength (MPa)	20.73	20.45	27.06	22.58
$E_2(= E_1)$ (MPa)	21773	13220	15025	16673
Poisson's ratio	$\nu_{21} = 0.255$	$\nu_{21} = 0.303$	$\nu_{23} = 0.155$	

Table 1.2: Young's modulus and Poisson's ratio of fired molded bricks [2]

## 3. Compressive strength

Compressive strength is an important property of bricks, presenting the ability of resisting to the load. [2] studied on the mechanical properties of molded bricks. The mechanical properties are carried out on two types of samples. The results showed an mechanical behavior shown as in Table 1.6. The bricks failure stress reached 22.58 MPa in the transverse direction, and 13.76 MPa in the pressed direction. Young's modulus  $E_3$  along the pressed direction is equal to 5524 MPa. It is about three times lower than the  $E_1$  modulus by hypothesis equal to  $E_2$  modulus measured at 16673 MPa.

## 1.5.2 The thermal conductivity of fired clay bricks

Thermal conductivity represents the level of difficulty of heat transfer, and plays a crucial role in energy transfer of fired clay bricks. As above mentioned, fired clay bricks are the matrix-inclusions materials. The macroscopic thermal conductivity is also determined by microscopic factors. In the thesis, we will study the effective thermal conductivity of fired clay bricks by homogenization approach. In the Law of Fourier, the thermal conductivity can be described by a second-order tensor.

$$\underline{Q} = -\underline{\lambda} \cdot S \frac{dT}{d\underline{x}} \quad (1.2)$$

where  $Q$  indicates the macroscopic heat flux ( $W$ ) vector.  $S$  denotes the cross sectional area ( $m^2$ ).  $dT/d\underline{x}$  represents the thermal gradient ( $K/m$ ) vector.  $\underline{\lambda}$  is the thermal conductivity tensor of material ( $W/m \cdot K$ ), depending on microstructure of material, density or porosity of material. The minus means the heat transfers from the position of high temperature to the position of low temperature.

For transversely isotropic fired clay bricks, the second-order thermal conductivity tensor can be written as:

$$\underline{\lambda} = \lambda_{11} \cdot (\underline{e}_1 \otimes \underline{e}_1 + \underline{e}_2 \otimes \underline{e}_2) + \lambda_{33} \cdot (\underline{e}_3 \otimes \underline{e}_3) \quad (1.3)$$

where  $\underline{e}_3 = (0, 0, 1)$  is the symmetric axis.

The thermal conductivity is sensitive to many faults (porosity, inclusion, crystal interface) [8]. In addition to that, anisotropy has an effect on thermal conductivity as mentioned above. [9] studied the thermal conductivities of clay green bodies in different directions (Table 1.3). These data in different directions exhibits an obvious transverse isotropy.

No. of samples	Perpendicular to extrusion ( $W/m \cdot K$ )	Parallel to extrusion ( $W/m \cdot K$ )	Anisotropic ratio
B1	$0.66 \pm 0.05$	$1.10 \pm 0.02$	1.67
B2	$0.66 \pm 0.06$	$0.93 \pm 0.05$	1.41
B3	$0.69 \pm 0.04$	$1.24 \pm 0.02$	1.80
B4	$0.57 \pm 0.08$	$0.86 \pm 0.08$	1.51
B5	$0.62 \pm 0.04$	$0.72 \pm 0.04$	1.16

Table 1.3: The effect of transverse isotropy on thermal conductivity [9]

### 1.5.3 The transverse isotropy of fired clay bricks

Based on experimental results [2, 8, 7], the mechanical properties of fired bricks are transversely isotropic due to the orientation of micropores caused by their producing technology. Anisotropy has an important effect on mechanical properties and conduction. Even though under the conditions of drying and baking, the oriented characteristic can't be changed or vanished, and just be diminished because of vitrification and recrystallization.

Young's modulus and compressive strength of fired bricks on three axial directions have been studied by [8] and the anisotropic ratio is given in Table 1.4. The anisotropic ratio of Young's modulus is approximately 1.30. The ratio of compressive strength which generally depends on the geometry of samples is about 1.39.

Orientation	Parallel	Perpendicular1	Perpendicular2
Young's modulus ( <i>GPa</i> )	$44.3 \pm 1$	$33.9 \pm 3.5$	$33.7 \pm 2.4$
Anisotropic ratio (%)	1.30	1	1
Compressive strength ( <i>MPa</i> )	169	120	119
Anisotropic ratio (%)	1.39	1	1

Table 1.4: The anisotropic ratio of Young's modulus and compressive strength [8]

[10] studied Young's modulus and compressive strength of different shape of samples in the extruded direction and another orthogonal direction. For prismatic samples (PS) and cylindrical samples (CS), the measured experimental results are shown in the following Table 1.5.

Orientation	Horizontal PS	Vertical PS	Vertical CS
Young's modulus ( <i>MPa</i> )	10450	12750	12830
Anisotropic ratio	1	1.22	1.23
Compressive strength ( <i>MPa</i> )	51	56.8	60.6
Anisotropic ratio	1	1.11	1.19

Table 1.5: The anisotropic ratio of Young's modulus and compressive strength [10]

For prismatic samples, Young's modulus in vertical direction is 1.22 times as the value in horizontal direction. The compressive strength in the vertical direction is about 1.11 times as the value in the horizontal direction. For vertical samples, Young's modulus of cylindrical samples is similar to (1.006 times) the value of prismatic samples. It has been verified that the material constant isn't affected by the geometry of bricks. The peaks stress of cylindrical samples is nearly equal to (1.067 times) the value of prismatic samples. In fact, the strength of sample is dependent on its geometry. But the effect of geometry can be ignored for the two shape of samples within a certain size.

The transverse isotropy of fired molded bricks have also been studied by experiments [2]. The results are exhibited in the following Table 1.6. Young's modulus in the transverse direction is 3.02 times as values in pressed direction. Compressive strength in transverse direction is about 1.64 times as values in the pressed direction.

Direction	Pressed direction	Transverse direction
Young's modulus ( <i>MPa</i> )	5520	16670
Anisotropic ratio	1	3.02
Compressive strength ( <i>MPa</i> )	13.8	22.6
Anisotropic ratio	1	1.64

Table 1.6: The anisotropic ratio of Young's modulus and compressive strength [2]

#### 1.5.4 The effect of porosity on mechanical properties and thermal conductivity of fired clay bricks

The physical properties of fired clay bricks include shape, porosity, water absorption, and so on. Porosity is one of the most important parameters, affecting properties of fired clay bricks. Micropores may be open or closed, and the shape of micropores may be spherical or flat oblate. The shapes, the volumes and the sizes of micropores can determine the mechanical properties, thermal property and durability of fired bricks [5, 41, 42, 43]. Generally speaking, the porosity of fired clay bricks means open porosity, because closed micropores are formed in high fired temperature [8]. The total porosity and the diameter of micropore can be measured by mercury porosimetry [44]. MIP (mercury intrusion porosimetry) could provide a good estimation for the open porosity and of the distribution of micropores with  $r < 1\mu m$  [17]. The porosity of fired clay bricks is affected by many factors, such as content of additives. Engineers always take interesting measures to change the porosity of fired bricks in order to improve their properties.

The effects of porosity of fired molding bricks on their mechanical strength and thermal conductivity have been studied (see [5]). In the research, recycled paper processing residues are used to be pore-forming agents to create micropores during the firing stage. The effect of porosity on peak strength is given in the Table 1.7.

In this research, it is found that the additives could contribute the 50% reduction of energy consumption by application of paper residues. The reason is that the additives are not only used to create micropores, but also to mix with clay to reduce the thermal conductivity of solid matrix. Table 1.8 indicates the thermal conductivity under different porosities.

[11] studied the effect of porosity on mechanical property and thermal conductivity of

Weight content (%)	Porosity (%)	Pressed direction (MPa)	Transverse direction (MPa)
0	30.8	40	45
10	38.9	16	23.5
20	46.2	7.6	15
30	52	5.1	7.4

Table 1.7: The effect of porosity on peak strength [5]

Weight content (%)	Porosity (%)	Thermal conductivity (W/m · K)
0	30.8	0.83 ± 0.03
10	38.9	0.59 ± 0.03
20	46.2	0.48 ± 0.01
30	52	0.42 ± 0.02

Table 1.8: The effect of porosity on thermal conductivity [5]

fired extruded bricks by adding two different agricultural solid wastes. The experimental results are shown in the Table 1.9. Wheat straw residue is abbreviated to WSR and olive stone flour is to OSF. The function of additives has two facets. On the one hand, they are fired to create micropores. On the other hand, they are mixed with clay to improve the performance of matrix.

Additives	Porosity (%)	Compressive strength (MPa)	Flexural strength (MPa)	Young's modulus (MPa)
WSR	27.9	36.2	13.37	23000
	32.6	26.6	12.42	17339
	39.5	21.4	8.4	14741
	43.5	18.1	7.1	13472
OSF	29.6	34	14.22	18572
	31.2	31.5	12.81	17830
	34.5	30.5	11.02	17460
	40.6	24.8	8.13	13765

Table 1.9: The effect of porosity on mechanical properties [11]

Table 1.10 shows that the effect of porosity on thermal conductivity from [11] in extruded direction. From these results, we can find that the mechanical properties and thermal conductivity decrease with the increase of porosity. The decrease tendency will be studied in the following chapters.

Additives	Porosity (%)	Thermal conductivity ( $W/m \cdot K$ )	Thermal conductivity ( $W/m \cdot K$ )
WSR	27.9	$0.49 \pm 0.02$	0.45
	32.6	$0.44 \pm 0.05$	0.41
	39.5	$0.36 \pm 0.03$	0.38
	43.5	$0.3 \pm 0.1$	0.34
OSF	29.6	$0.49 \pm 0.04$	0.43
	31.2	$0.45 \pm 0.06$	0.42
	34.5	$0.44 \pm 0.09$	0.41
	40.6	$0.39 \pm 0.11$	0.35

Table 1.10: The effect of porosity on thermal conductivity [11, 12]

## 1.6 Conclusions

As multiphased and porous materials, fired clay bricks having excellent mechanical and heat insulating performances. The micro-structure plays an important role in macroscopic properties. Based on the microscopic and macroscopic analysis, several conclusions about fired clay products can be obtained:

Firstly, micropores widely exist in fired clay bricks, and have a strong influence on mechanical properties and thermal conductivity.

Secondly, comparing experimental results, the mechanical properties and thermal conductivity of fired clay bricks display the transverse isotropy, including extruded and molded bricks. As shown in SEM images, the transverse isotropy is induced by the parallel orientation of micropores related with production technology.

The following research deals with the effect of microscopic information on the mechanical properties and thermal conductivity of fired clay bricks by homogenization theory, including porosity, the shapes and orientations of micropores and microcracks, as well as their spatial distributions. The objectives are also to propose a framework of behavior law to take into account for the anisotropy induced by micropores and microcracks.



# The effective elastic properties of fired clay bricks

---

## Contents

<b>2.1</b>	<b>Introduction</b>	<b>37</b>
<b>2.2</b>	<b>Basic concepts of micromechanics of materials</b>	<b>39</b>
2.2.1	The scale separation of characteristic Scale	39
2.2.2	The methodology of micromechanics	39
<b>2.3</b>	<b>The representative volume element (RVE) for fired clay bricks</b>	<b>40</b>
<b>2.4</b>	<b>Homogenization of the elastic properites</b>	<b>41</b>
<b>2.5</b>	<b>Estimates of the effective stiffness tensor</b>	<b>44</b>
2.5.1	The Mori-Tanaka (MT) scheme	44
2.5.2	The Ponte Castañeda-Willis (PCW) scheme	45
<b>2.6</b>	<b>The prediction for the effective elastic properties of fired clay bricks</b>	<b>46</b>
2.6.1	The MT estimate of elastic properties	46
2.6.2	The PCW estimate of elastic properties	50
2.6.3	The comparison of the prediction between MT and PCW schemes	51
<b>2.7</b>	<b>Calibrations and experimental validations</b>	<b>53</b>
<b>2.8</b>	<b>Conclusions</b>	<b>56</b>

---

## 2.1 Introduction

The limitation of the traditional phenomenology methods and the invention of advanced experimental techniques promote the development of micromechanics of porous media. The main idea of micromechanics characterizes macroscopic properties and behaviors based

on microscopic structures of porous materials, namely, homogenization [45, 46]. In this chapter, we will introduce the homogenization theory to deal with the problem of linear elasticity.

The mechanical properties of fired clay bricks, containing elastic property and mechanical behavior, play an important role in engineering design of masonry structures. As the analysis of micro-structure in chapter 1, fired clay bricks are the transversely isotropic porous material whose stiffness tensor has 5 independent elastic constants. For fired clay bricks, micro-void is a quite important characteristic affecting the mechanical properties. So far, there have been some models used to predict mechanical properties with the consideration of porosity of fired clay bricks [47, 48, 49, 50, 51, 52, 53]. Figure 2.1 shows the comparison between models and experimental results. Most of them exhibit a good prediction under moderate porosity. But these models are empirical and don't build a micro-macro relationship. Based on these reasons, the prediction for elastic constants of fired clay bricks is studied by making use of homogenization theory in this chapter. Referring to mechanical behavior of fired clay bricks, it will be studied in Chapter 4.

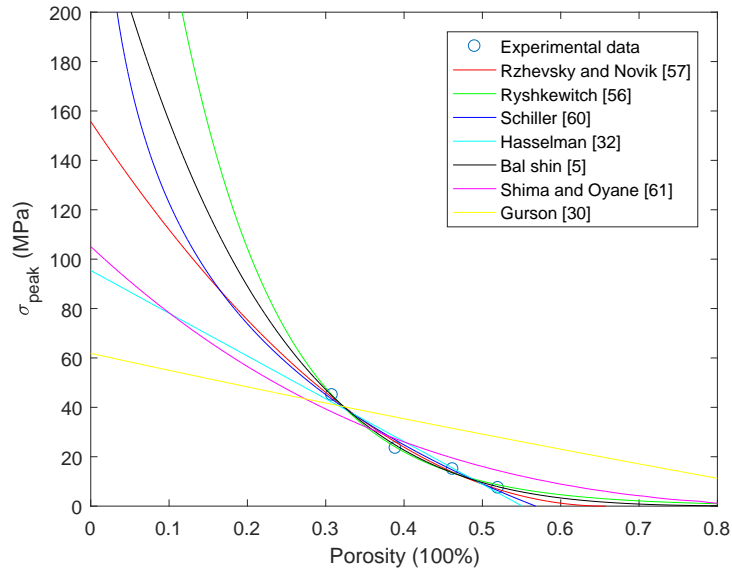


Figure 2.1: The relationship between peak strength and porosity

Firstly, the basic principle and concepts of micromechanics are introduced in detail. Next, two different shaping technologies of extruded and molded bricks are described to explain the transverse isotropy. And the simplified representative volume elements (RVE) are proposed for extruded and molded bricks. Then, the local problem for linear elasticity and the homogenization method are presented. Subsequently, we present the Mori-Tanaka (MT) scheme, which is classically used for the case of taking account of interactions between inclusions. We also introduce the Ponte Castañeda-Willis (PCW) scheme bound, in which

a distinguish between geometry and spatial distribution of inclusions. For each model, the transversely isotropic stiffness tensor is calculated and numerical predictions of elastic constants are achieved in order to quantify the influence of porosity. Finally, parameter calibrations and experimental validations are carried out.

## 2.2 Basic concepts of micromechanics of materials

### 2.2.1 The scale separation of characteristic Scale

The characteristic lengths of RVE and the lengths of macro-structure are defined as  $l$  and  $L$ , respectively. On the one hand,  $l \ll L$  is to make the scale of RVE small enough to satisfy the basic assumption of continuum mechanics. On the other hand, the length of RVE should be large enough to contain adequate micro-information and allow the statistical average behavior of local continuum medium. If  $d$  is defined as the characteristic length of local heterogeneities, there will be  $d \ll l$ . In a word, the scale conditions on the RVE are [54]:

$$d \ll l \ll L$$

### 2.2.2 The methodology of micromechanics

The method of micromechanics aims to replace heterogeneous medium by homogenized equivalent medium or effective medium. There are three steps for homogenization procedure:

1. The mathematical representation of medium at the microscale, including the definition of phases, the description of geometry and spatial distribution, the description of local property.
2. The localization, building the quantitative relationship between microscopic phases and the macroscopic boundary condition applied on the RVE.
3. The homogenization, to obtain the effective property of material based on the micro-information of heterogeneous material.

## 2.3 The representative volume element (RVE) for fired clay bricks

The produce process and the microstructure of fired clay bricks have been described in the preceding chapter. In other words, the produce technology affects the microscopic information and macroscopic properties of clay products. The influence of produce technology on products will be expounded in this section.

Based on the information of microstructure studied by [4], fired clay bricks mainly contain glassy phase, sands and silts, micropores. To simplify the research problem, all solid phases are considered as a unique solid matrix. The solid matrix and the micropores are regarded as the two main factors determining the performance of products.

For extruded bricks, in the shaping step, raw materials are pushed by a pushing spiral in a vacuum environment from one side, and go through from the other side (the machine head). Between the two sides, all materials are enclosed in the vacuum environment, and evenly suffered loading all around. This condition can lead to analogously parallel and spheroidal area showed in Figure 1.10. That is the reason why extruded bricks are transversely isotropic. A schematic diagram of extruded process has been given in Figure 2.2, including 2-dimensional extruded technology, 3-dimensional brick and 3-dimensional geometry of micropore. It is assumed that the geometries of all micropores are prolate spheroids. The extruded direction is parallel to the long 3-axis of prolate spheroid.  $m_1$  and  $m_3$  represent the semi-axis of ellipsoid on 1-axis and 3-axis, and  $m_1 = m_2$ .

For molded bricks, a brick is shaped and applied a pressure in a mold showed in 3-dimensional Figure 2.3. The shape of micropore is oblate spheroidal. The short 3-axis of oblate spheroid is parallel to the pressure direction. The difference between extruded bricks and moulded bricks is the shape and the orientation of micropores. Likewise, the 3-axis (pressure direction) is also the symmetric axis, and  $m_1 = m_2$ .

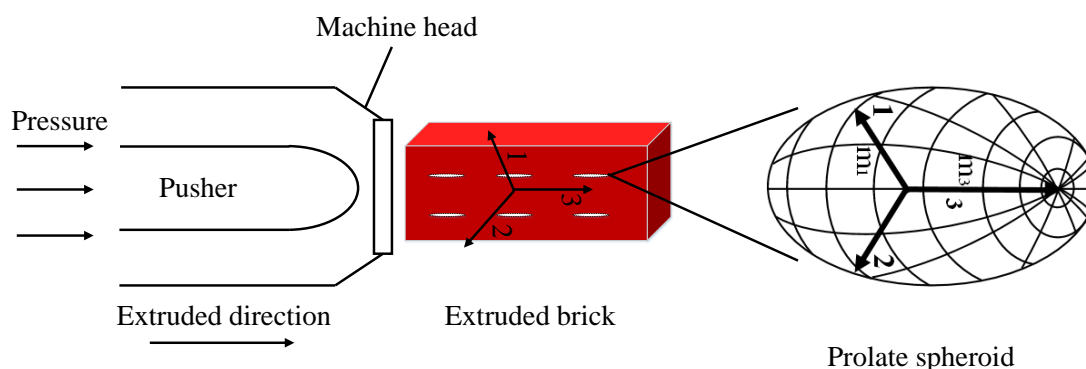


Figure 2.2: The prolate micropore in extruded bricks

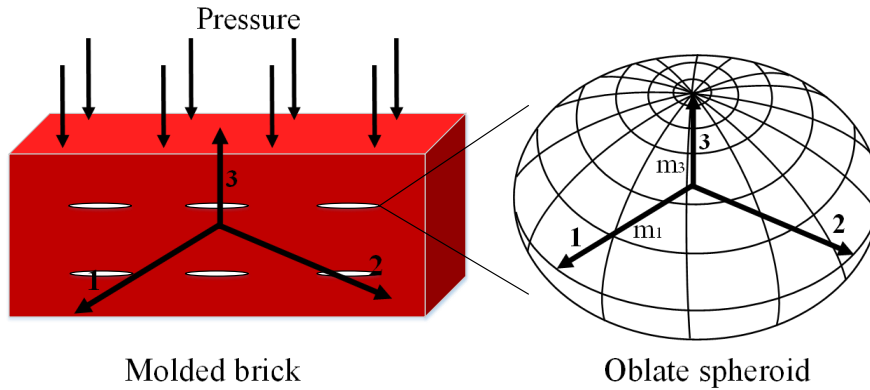


Figure 2.3: The oblate micropore in moulded bricks

In order to characterize the heterogeneous characteristics of fired clay bricks, a simplified 3-dimensional RVE for fired clay bricks at one microscale is showed as the following Figure 2.4 and Figure 2.5. The section of the RVE is taken from the plane that parallels to our paper in the 3-dimensional brick. The RVE in Figure 2.4 represents extruded bricks, and another RVE in Figure 2.5 describes moulded bricks. It should be obvious that the difference of geometry of micropores between two types of bricks result from different produce technology. Both the physical properties of solid matrix are considered as isotropic.

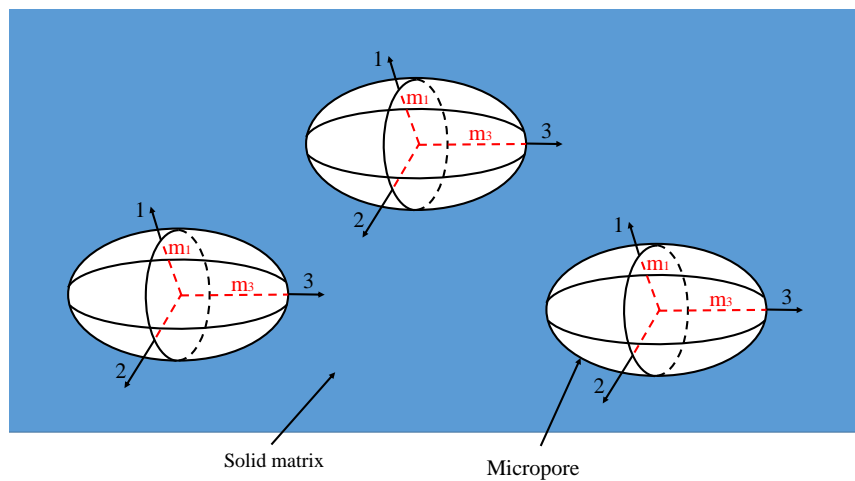


Figure 2.4: The representative volume element for extruded bricks

## 2.4 Homogenization of the elastic properties

We consider the RVE of a material as the domain  $\Omega$ , and  $\partial\Omega$  denotes the boundary of the domain. The microscopic strain and stress fields in RVE are equal to zero if there is

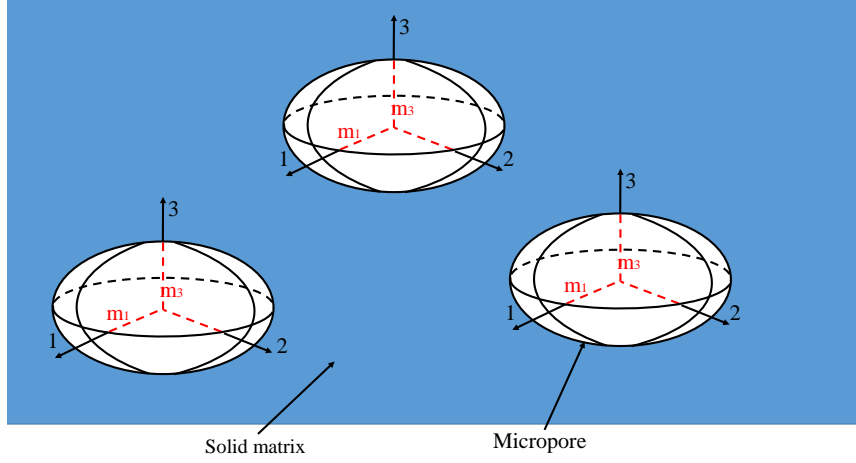


Figure 2.5: The representative volume element for moulded bricks

no external disturbance on the boundary. In the case of ignoring the volume force, the infinite boundary is subjected to the macroscopic uniform strain tensor  $\underline{\underline{E}}$ . The link between the microscopic displacement field and the macro-scale strain field on the boundary is  $\underline{u}(\underline{z}) = \underline{\underline{E}} \cdot \underline{z}$ . According to Gauss' Divergence theorem, it can be proved that:

$$\langle \underline{\underline{\varepsilon}} \rangle = \frac{1}{|\Omega|} \int_{\Omega} \underline{\underline{\varepsilon}}(\underline{z}) d\Omega = \underline{\underline{E}} \quad (2.1)$$

We adopt  $\underline{\underline{\sigma}}(\underline{z})$  and  $\underline{\underline{\varepsilon}}(\underline{z})$  to represent the local stress tensor and local strain tensor at the microscale, respectively. The solutions of the homogenization problem can be obtained from the following equations:

$$\begin{cases} \nabla \cdot \underline{\underline{\sigma}}(\underline{z}) = 0 \\ \underline{\underline{\sigma}}(\underline{z}) = \mathbb{C}(\underline{z}) : \underline{\underline{\varepsilon}}(\underline{z}) \\ \underline{\underline{\varepsilon}}(\underline{z}) = \frac{1}{2} [\underline{\underline{gradu}} + (\underline{\underline{gradu}})^T] \\ \underline{u}(\underline{z}) = \underline{\underline{E}} \cdot \underline{z}, \quad \forall \underline{z} \in \partial\Omega \end{cases} \quad (2.2)$$

where  $\mathbb{C}(\underline{z})$  represents the fourth-order stiffness tensor at point  $\underline{z}$ .

The microscale strain  $\underline{\underline{\varepsilon}}(\underline{z})$  can be linearly expressed by the macroscale strain  $\underline{\underline{E}}$  using a fourth-order strain concentration tensor  $\mathbb{A}$ :

$$\underline{\underline{\varepsilon}}(\underline{z}) = \mathbb{A}(\underline{z}) : \underline{\underline{E}} \quad (2.3)$$

It follows that:

$$\langle \underline{\underline{\varepsilon}} \rangle = \langle \mathbb{A} : \underline{\underline{E}} \rangle = \langle \mathbb{A} \rangle : \underline{\underline{E}} \quad (2.4)$$

which, by comparison with (2.1) yields:

$$\langle \mathbb{A} \rangle = \mathbb{I} \quad (2.5)$$

where  $\mathbb{I}$  is the fourth-order unit tensor.

Combining the local constitutive equation and (2.3), one gets:

$$\underline{\underline{\sigma}}(z) = \mathbb{C}(z) : \underline{\underline{\varepsilon}}(z) = \mathbb{C}(z) : \mathbb{A}(z) : \underline{\underline{E}} \quad (2.6)$$

By average, it is readily obtained:

$$\underline{\underline{\Sigma}} = \langle \underline{\underline{\sigma}}(z) \rangle = \mathbb{C}^{hom} : \underline{\underline{E}} \quad (2.7)$$

which represents the macroscopic stress-strain relationship, with

$$\mathbb{C}^{hom} = \langle \mathbb{C}(z) : \mathbb{A}(z) \rangle \quad (2.8)$$

where  $\mathbb{C}^{hom}$  is the macroscopic fourth-order effective stiffness tensor. For a RVE composed of matrix and inclusions, it is assumed that all properties are same in the  $r$ -th phase. We define  $|\Omega_r|$  as the volume of the  $r$ -th phase in the material.  $\mathbb{C}_r$  is the stiffness tensor in the  $r$ -th phase.  $f_r$  is the volume fraction of the  $r$ -th phase. The concentration tensors  $\mathbb{A}(z)$  is replaced by  $\mathbb{A}_r$ . The effective stiffness tensor can be recast as:

$$\mathbb{C}^{hom} = \sum_{r=0}^N f_r \mathbb{C}_r : \mathbb{A}_r \quad (2.9)$$

where  $r = 0$  represents the solid matrix, which will be signified by the subscript  $s$  in what follows. Recalling relation (2.5), the concentration tensor  $\mathbb{A}_0$  of solid matrix can be expressed by the concentration tensors of inclusions:

$$f_s \mathbb{A}_s = \mathbb{I} - \sum_{r=1}^N f_r \mathbb{A}_r \quad (2.10)$$

It follows that the effective stiffness tensor (2.9) could be recast as another formation:

$$\mathbb{C}^{hom} = \mathbb{C}_s + \sum_{r=1}^N f_r (\mathbb{C}_r - \mathbb{C}_s) : \mathbb{A}_r \quad (2.11)$$

It is obvious that the calculation for localization tensor  $\mathbb{A}_r$  is crucial to obtain the effective stiffness tensor. The concentration tensor can be determined by means of three classical schemes (dilute, Mori-Tanaka, Ponte Castañeda-Willis). Dilute scheme is assumed that there is no interaction between inclusions and fit for the case of small concentration

of inclusions. The solution of the localization problem for a single ellipsoidal inclusion embedded in an infinite matrix is provided by solving the so-called Eshelby's inclusion problem [55]. The solution of this problem is:

$$\mathbb{A}_r = [\mathbb{I} + \mathbb{P}_r^\epsilon : (\mathbb{C}_r - \mathbb{C}_s)]^{-1} \quad (2.12)$$

with

$$\mathbb{P}_r^\epsilon = \mathbb{S}_r^\epsilon : \mathbb{C}_s^{-1} \quad (2.13)$$

where the subscript  $\epsilon$  indicates the shape and orientation of inclusion.  $\mathbb{P}_r^\epsilon$  is the fourth-order Hill tensor [56].  $\mathbb{S}_r^\epsilon$  is the Eshelby tensor which is dependent on the shape of inclusion and the stiffness of matrix.  $\mathbb{C}_s$  is the stiffness tensor of solid matrix.

In the following parts, the above mentioned homogenization schemes based on different tensors  $\mathbb{A}_r$  will be introduced briefly.

## 2.5 Estimates of the effective stiffness tensor

In this section, we will briefly describe two homogenization schemes, including Mori-Tanaka approach [57] and Ponte Castañeda-Willis approach [58] for multi-phase media by virtue of the solution of single-inclusion derived by [55]. Both the two approximations consider the interaction of inclusions, but the difference between them is the consideration of spatial distributions of inclusions.

### 2.5.1 The Mori-Tanaka (MT) scheme

Mori-Tanaka scheme takes into account the interactions between inclusions, and it is fit for the case of inclusions with moderate concentration [57]. In the new framework, the macroscopic strain boundary condition is no longer  $\underline{\underline{E}}$ . We assume that the inclusion of the  $r$ -th phase suffers the uniform strain field  $\underline{\underline{E}}^0$  at infinity. The microscopic strain of the  $r$ -th phase can be written as:

$$\underline{\underline{\varepsilon}}_r = \mathbb{A}_r^0 : \underline{\underline{E}}^0 \quad (2.14)$$

where  $\mathbb{A}_r^0$  is the local localization tensor:

$$\mathbb{A}_r^0 = [\mathbb{I} + \mathbb{P}_r^\epsilon : (\mathbb{C}_r - \mathbb{C}_s)]^{-1} \quad (2.15)$$

Hill tensor  $\mathbb{P}_r^\epsilon$  was given in (2.13).

According to the law of volume average  $\langle \underline{\underline{\varepsilon}} \rangle = \underline{\underline{E}}$ , the tensor  $\underline{\underline{\varepsilon}}_0$  can be expressed by  $\underline{\underline{E}}$ :

$$\underline{\underline{E}}^0 = \left[ \sum_{r=0}^N f_r \mathbb{A}_r^0 \right]^{-1} : \underline{\underline{E}} \quad (2.16)$$

Accordingly, the overall localization tensor  $\mathbb{A}_r^{MT}$  of the  $r$ -th phase is:

$$\mathbb{A}_r^{MT} = \mathbb{A}_r^0 : \left[ \sum_{r=0}^N f_r \mathbb{A}_r^0 \right]^{-1} \quad (2.17)$$

## 2.5.2 The Ponte Castañeda-Willis (PCW) scheme

The scheme, which is based on the extension of the Hashin-Shtrikman bound, separates the shape of inclusion and the spatial distribution of inclusion by two independent tensor functions [58]. Based on the microstructure of fired clay bricks, it is assumed that the spatial distribution of parallel micropores is spherical. As shown in Figure 2.6, red inclusions aligned with a symmetric direction are micropores and these circles represents the spherical distribution.

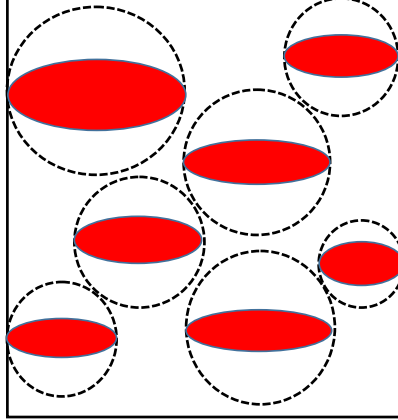


Figure 2.6: The spherical distribution with spheroidal inclusions

The fourth-order strain concentration tensor is in the form of [58, 59]:

$$\mathbb{A}_r^{PCW} = [\mathbb{I} + \mathbb{P}_r^\epsilon : (\mathbb{C}_r - \mathbb{C}_s)]^{-1} : \left\{ f_s \mathbb{I} + \sum_{r=1}^N f_r [\mathbb{I} + (\mathbb{P}_r^\epsilon - \mathbb{P}_r^d) : (\mathbb{C}_r - \mathbb{C}_s)] : [\mathbb{I} + \mathbb{P}_r^\epsilon : (\mathbb{C}_r - \mathbb{C}_s)]^{-1} \right\}^{-1} \quad (2.18)$$

where the subscript  $\epsilon$  and  $\mathbb{P}_r^\epsilon$  has been pointed that represents the shape. Another subscript

$d$  denotes the spatial distribution, and  $\mathbb{P}_r^d$  represents the spatial distribution tensor of the  $r$ -th phase.

## 2.6 The prediction for the effective elastic properties of fired clay bricks

In this section, the effective elastic properties of fired clay bricks will be deduced by MT and PCW approaches. It is noted that, for the case of aligned inclusions, the stiffness tensor by MT scheme can be derived from PCW formula if the distribution function  $\mathbb{P}_r^d$  is identical to their shape function  $\mathbb{P}_r^\epsilon$  [60, 61]. However, for randomly oriented ellipsoidal inclusions, the Mori-Tanaka result cannot be derived from the PCW estimation [62].

### 2.6.1 The MT estimate of elastic properties

The prediction for elastic properties by MT scheme will be analyzed in the part. As is shown in Figure 2.4 and Figure 2.5, heterogeneous fired bricks can be regarded as a two-phase material composed of solid phase (subscript  $s$ ) and pore phase (subscript  $p$ ). Expanding formula (2.17), the fourth-order strain concentration tensor of micropores yields:

$$\mathbb{A}_p^{MT} = \left[ \mathbb{I} + \mathbb{P}_p^\epsilon : (\mathbb{C}_p - \mathbb{C}_s) \right]^{-1} : \left\{ f_s \mathbb{I} + f_p \left[ \mathbb{I} + \mathbb{P}_p^\epsilon : (\mathbb{C}_p - \mathbb{C}_s) \right]^{-1} \right\}^{-1} \quad (2.19)$$

The fourth-order effective stiffness tensor of MT estimation can be expressed as:

$$\mathbb{C}^{MT} = (1 - f_p) \mathbb{C}_s : \left[ (1 - f_p) \mathbb{I} + f_p (\mathbb{I} - \mathbb{S}_p)^{-1} \right]^{-1} \quad (2.20)$$

As described in our RVE, micropores are parallel and symmetric about the 3-axis and the solid matrix is considered to be isotropic, which induce the transversely isotropic properties of fired clay bricks. Walpole's notation, which has been described in Appendix A, is used to represent transversely isotropic tensor by the decomposition of unit tensor in micromechanics [63]. Based on that, the effective stiffness tensor (2.20) of fired bricks can be expressed by the following form:

$$\mathbb{C}^{MT} = [C_1, C_2, C_3, C_4, C_5, C_5] \quad (2.21)$$

where the calculated results of  $C_1, C_2, C_3, C_4, C_5$  have been given in C.15.

The corresponding fourth-order effective compliance tensor can be expressed by stiffness tensor components:

$$\mathbb{S}^{MT} = [S_1, S_2, S_3, S_4, S_5, S_5] \quad (2.22)$$

with

$$S_1 = \frac{C_2}{\Delta_1}, S_2 = \frac{C_1}{\Delta_1}, S_3 = \frac{1}{C_3}, S_4 = \frac{1}{C_4}, S_5 = -\frac{C_5}{\Delta_1} \quad (2.23)$$

and

$$\Delta_1 = C_1 \cdot C_2 - 2 \cdot C_5^2 \quad (2.24)$$

It is known that the macroscopic stress-strain relationship:

$$\underline{\underline{E}} = \mathbb{S}^{MT} : \underline{\underline{\Sigma}} \quad (2.25)$$

Based on the Voigt notation in Appendix A, the transversely isotropic compliance tensor  $\mathbb{S}^{PCW}$  can be represented by the following matrix:

$$\mathbb{S}^{MT} \equiv \begin{pmatrix} \frac{1}{2}(S_1 + S_3) & \frac{1}{2}(S_1 - S_3) & S_5 & 0 & 0 & 0 \\ \frac{1}{2}(S_1 - S_3) & \frac{1}{2}(S_1 + S_3) & S_5 & 0 & 0 & 0 \\ S_5 & S_5 & S_2 & 0 & 0 & 0 \\ 0 & 0 & 0 & S_4 & 0 & 0 \\ 0 & 0 & 0 & 0 & S_4 & 0 \\ 0 & 0 & 0 & 0 & 0 & S_3 \end{pmatrix} \quad (2.26)$$

The five elements in the matrix (2.26) are given in (2.23). Combining matrixes (2.26) and (1.1), it is readily to obtain 5 elastic constants of fired clay bricks showed in following expressions.

The longitudinal Young's modulus is:

$$E_3^{MT} = \frac{1}{S_2} \quad (2.27)$$

The transverse Young's modulus is:

$$E_1^{MT} = E_2^{MT} = \frac{2}{S_1 + S_3} \quad (2.28)$$

The shear modulus are:

$$\begin{aligned}
G_{23}^{MT} &= \frac{1}{2S_4} \\
G_{12}^{MT} &= \frac{1}{2S_3}
\end{aligned}
\tag{2.29}$$

Poisson's ratio is:

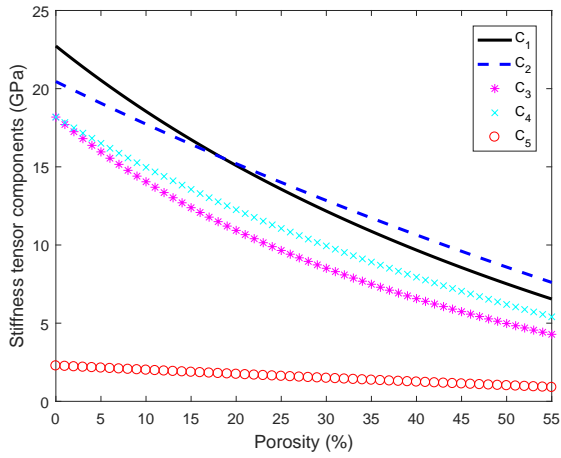
$$\nu_{13}^{MT} = -E_1 S_5 \tag{2.30}$$

Subsequently, the relationships between elastic constants and porosity are illustrated in following figures. The aspect ratio  $X = m_3/m_1 > 1$  of micropores stands for extruded bricks, and  $X = m_3/m_1 < 1$  represents molded bricks. At first, the relationship between stiffness tensor components and porosity is drawn under the fixed parameters  $E_s = 20000(MPa)$ ,  $\nu_s = 0.1$ ,  $X = 2$ , showed in Figure 2.7 (a). The stiffness tensor components are represented by Walpole's notation (shown as C.1). It can be seen that the stiffness decreases obviously as porosity increases, in which  $C_1/2$  represents the compression modulus,  $C_3/2$  denotes the transverse shear modulus,  $C_4/2$  represents the axial shear modulus.  $C_2$  and  $C_5$  are constants related with Young's modulus and Poisson's ratio.

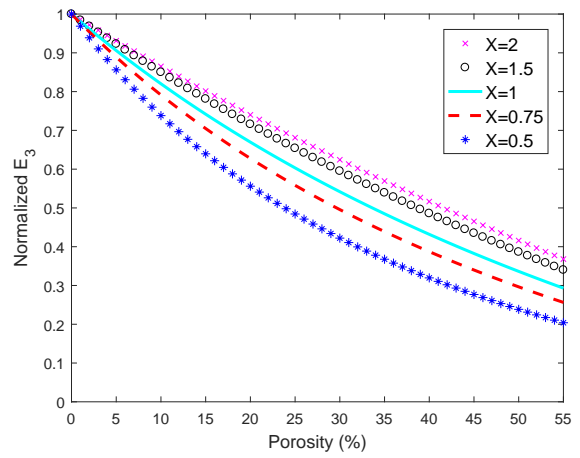
Figure 2.7 (b) and Figure 2.7 (c) display the relationships between normalized Young's moduli ( $E^{MT}/E_s$ ) and porosity under different aspect ratios of micropores. Figure 2.7 (b) depicts the variation of normalized  $E_3$ , and Figure 2.7 (c) is for normalized  $E_1$ . From the two figures, Young's modulus  $E_3$  corresponding to  $X = 2$  is the largest on the 3-axis. Conversely, Young's modulus  $E_3$  is the smallest on the 1-axis when  $X = 2$ . It means that Young's modulus on the major axis is larger than those on other orientations. Young's modulus on the minor axis is the smallest.

Figure 2.7 (d) and Figure 2.7 (e) show the relationships between normalized shear moduli ( $G^{MT}/G_s$ ) on two coordinate planes and porosity under different aspect ratios of micropores. It is also obvious that shear moduli decrease with the increasing of porosity. From two figures, it can be concluded that the shear modulus on the plane paralleling to the major axis of micropore is greater than those on other planes. The effect of aspect ratio on shear modulus  $G_{12}$  appears more clearly.

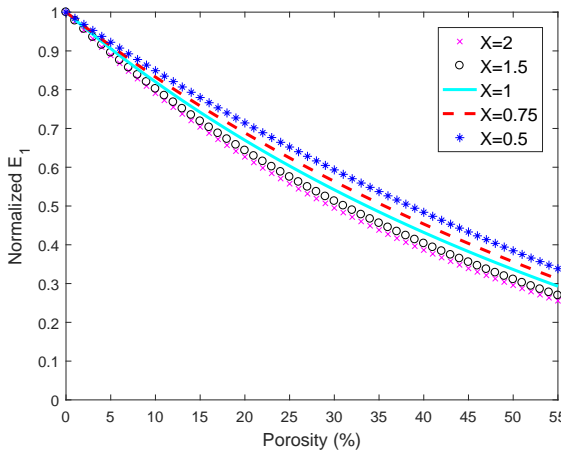
Figure 2.7 (f) plots the variation of normalized Poisson's ratio  $\nu_{13}$  as porosity increases. The aspect ratio obviously affects the  $\nu_{13}$  of molded bricks.



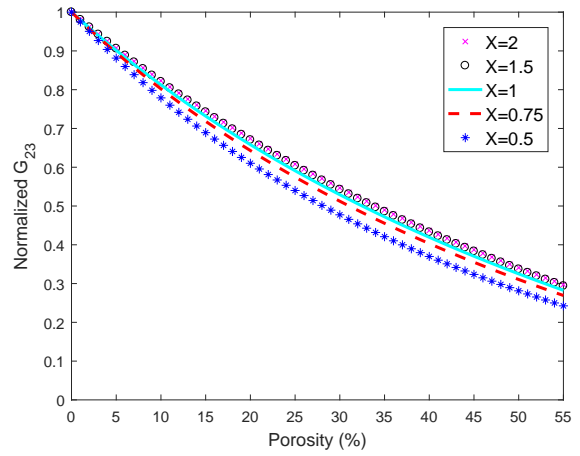
(a) The prediction for stiffness tensor



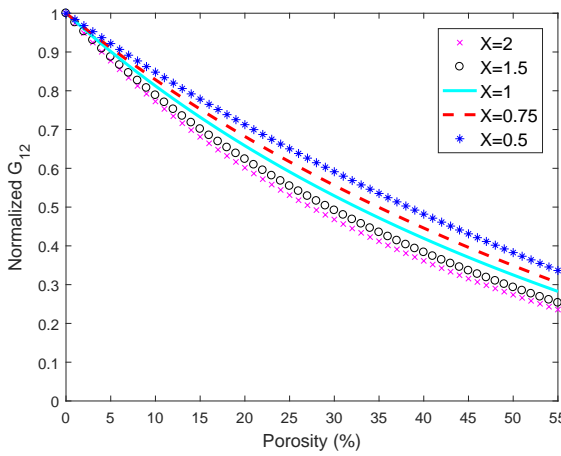
(b) The prediction for  $E_3$



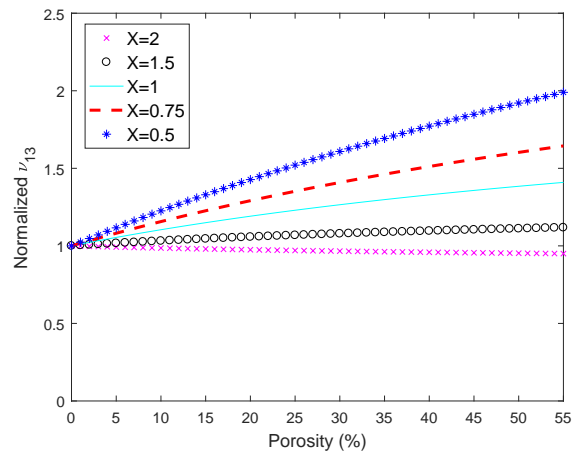
(c) The prediction for  $E_1$



(d) The prediction for  $G_{23}$



(e) The prediction for  $G_{12}$



(f) The prediction for  $\nu_{13}$

Figure 2.7: The relationships between elastic constants and porosity by MT estimate

## 2.6.2 The PCW estimate of elastic properties

As mentioned above, the PCW estimation considers the spatial distribution of micropores compared with MT method. For micropores, the strain concentration tensor (2.18) can be recast as:

$$\begin{aligned} \mathbb{A}_p^{PCW} = & \left[ \mathbb{I} + \mathbb{P}_p^\epsilon : (\mathbb{C}_p - \mathbb{C}_s) \right]^{-1} \\ & : \left\{ f_s \mathbb{I} + f_p [\mathbb{I} + (\mathbb{P}_p^\epsilon - \mathbb{P}_p^d) : (\mathbb{C}_p - \mathbb{C}_s)] : [\mathbb{I} + \mathbb{P}_p^\epsilon : (\mathbb{C}_p - \mathbb{C}_s)]^{-1} \right\}^{-1} \end{aligned} \quad (2.31)$$

It is assumed that the spatial distribution of micropores is spherical. So the tensorial function of the spatial distribution can be expressed as [64]:

$$\mathbb{P}_p^d = \frac{\alpha}{3k_s} \mathbb{J} + \frac{\beta}{2\mu_s} \mathbb{K} \quad (2.32)$$

with

$$\begin{aligned} \alpha &= \frac{3k_s}{3k_s + 4\mu_s} \\ \beta &= \frac{6(k_s + 2\mu_s)}{5(3k_s + 4\mu_s)} \end{aligned} \quad (2.33)$$

where  $k_s$  is the bulk modulus of solid matrix and  $\mu_s$  is the shear modulus of solid matrix.

The stiffness tensor of micropores  $\mathbb{C}_p$  is equal to 0, so equation (2.31) can be simplified as:

$$\mathbb{A}_p^{PCW} = (\mathbb{I} - \mathbb{S}_p^\epsilon)^{-1} : [\mathbb{I} + f_p(\alpha \mathbb{J} + \beta \mathbb{K}) : (\mathbb{I} - \mathbb{S}_p^\epsilon)^{-1}]^{-1} \quad (2.34)$$

As in the previous section, the effective stiffness tensor of fired clay bricks by PCW estimation can be derived and expressed by Walpole's notation [63]:

$$\mathbb{C}^{PCW} = [C_1, C_2, C_3, C_4, C_5, C_5] \quad (2.35)$$

where the calculated results of  $C_1, C_2, C_3, C_4, C_5$  have been given in C.2.

In order to exhibit the relationship between stiffness tensor components and porosity, the following hypothetical parameters are still taken:  $E_s = 20000(MPa)$ ,  $\nu_s = 0.1$  and  $X = 2$ . Figure 2.8 (a) gives the variation of stiffness tensor components. Compared with results from MT method, the predictions for  $C_1$  and  $C_3$  by PCW scheme decline much steeper. In other words, the spatial distribution has a stronger influence on the two elastic constants.

Figure 2.8 (b) and Figure 2.8 (c) illustrate that the relations between normalized Young's moduli and porosity under different aspect ratios. From two figures, we can find that Young's modulus on the 3-axis is greater than that on the 1-axis. Combining two figures, it is seen that the aspect ratio has a more sensible effect on Young's modulus  $E_3$ .

Figure 2.8 (d) and Figure 2.8 (e) exhibit the variation between normalized shear moduli and porosity under different aspect ratios. It is clear that shear moduli decline with the increase of porosity. From the two figures, it can be concluded that the shear modulus on the plane paralleling to the long axis of micropore is greater than those on other planes. From extruded bricks, the aspect ratio has little influence on  $G_{23}$ .

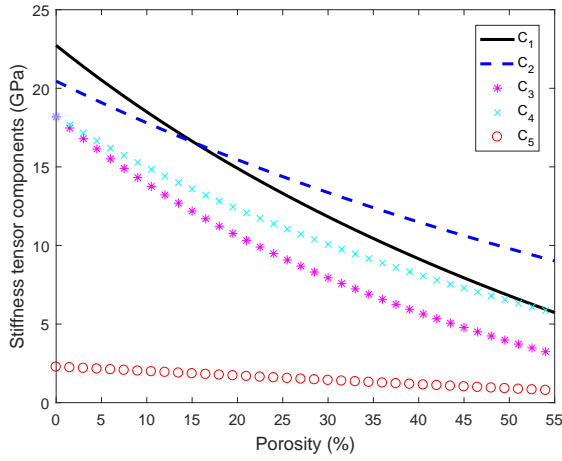
Figure 2.8 (f) depicts the variation of normalized Poisson's ratio. We can find that porosity has a stronger influence on  $\nu_{13}$  of molded bricks than that of extruded bricks. In all word, the five independent constants can entirely represent elastic properties of fired clay bricks.

### 2.6.3 The comparison of the prediction between MT and PCW schemes

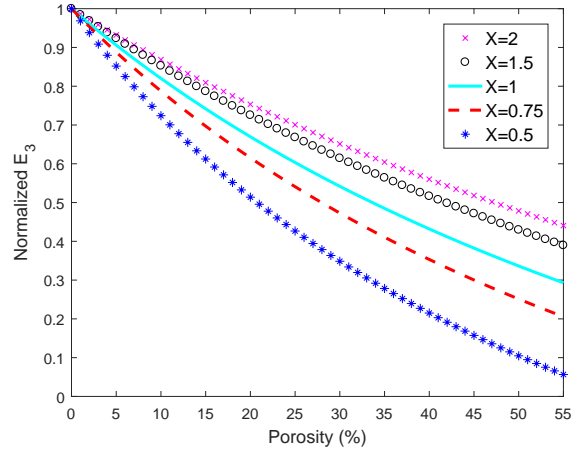
The difference of the prediction for normalized Young's modulus between MT and PCW schemes is illustrated in following figures.

Figure 2.9 plots the prediction for normalized Young's modulus of fired extruded bricks by two schemes. It is assumed that the aspect ratio of micropores is equal to 2 and Poisson's ratio of solid matrix is 0.1. In this figure, Young's modulus along the orientation of the major 3-axis of prolate ellipsoid is greater than that on the 1-axis. In fact, Young's modulus along the major axis is the maximum and the value along the minor axis is the minimum. Young's modulus on other orientations can be calculated by rotation matrix. Moreover, compared with the prediction of MT scheme, the prediction by PCW scheme considering spatial distribution exhibits the greater ratio of modulus, that is  $E_3^{PCW}/E_1^{PCW} > E_3^{MT}/E_1^{MT}$ . Figure 2.10 draws the prediction for normalized Young's modulus of fired molded bricks by two schemes. The assumed parameters are the aspect ratio of micropores  $X = 0.5$  and Poisson's ratio of solid matrix  $\nu_s = 0.1$ . It can be summarized similar conclusions.

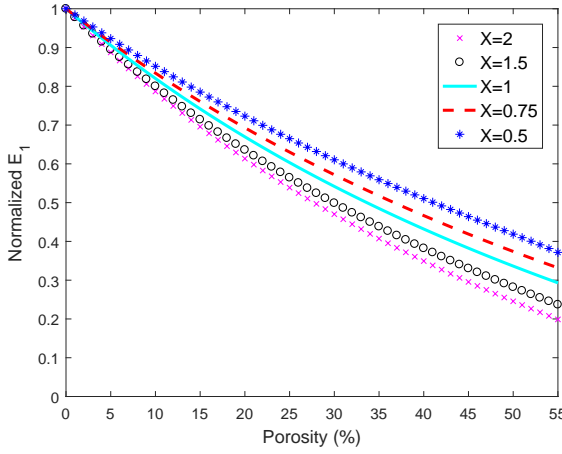
Figure 2.11 and 2.12 are the comparison of normalized shear modulus between MT scheme and PCW scheme. Like Young's modulus, the prediction of shear modulus by PCW estimate also exhibits a greater ratio of shear modulus than that by MT approach. For extruded and molded bricks, the shear modulus  $G_{23}$  perpendicular to the isotropic plane is always greater than shear moduli on other planes.



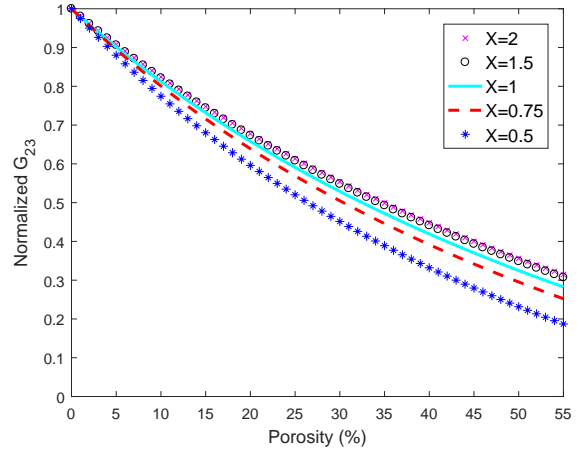
(a) The prediction for stiffness tensor



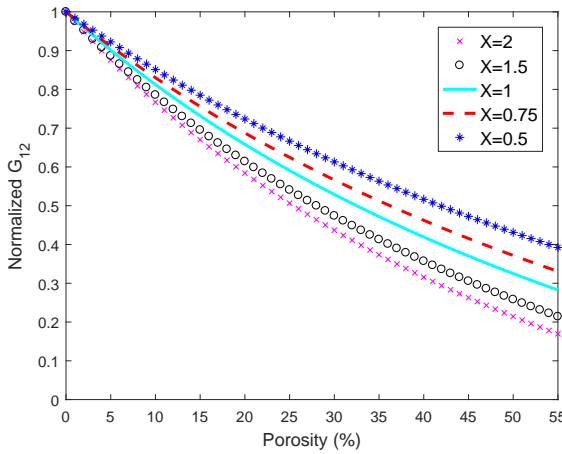
(b) The prediction for  $E_3$



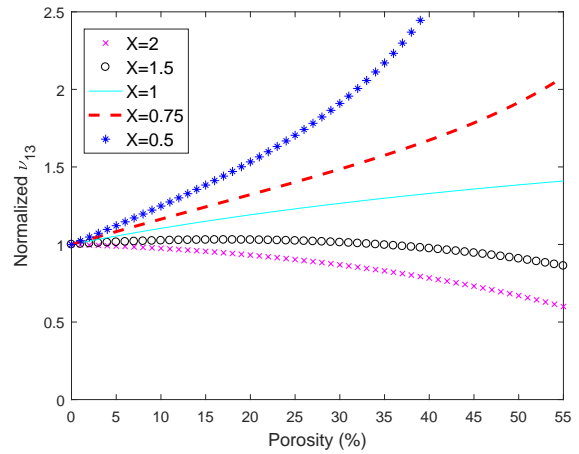
(c) The prediction for  $E_1$



(d) The prediction for  $G_{23}$



(e) The prediction for  $G_{12}$



(f) The prediction for  $\nu_{13}$

Figure 2.8: The relationships between elastic constants and porosity by PCW estimate

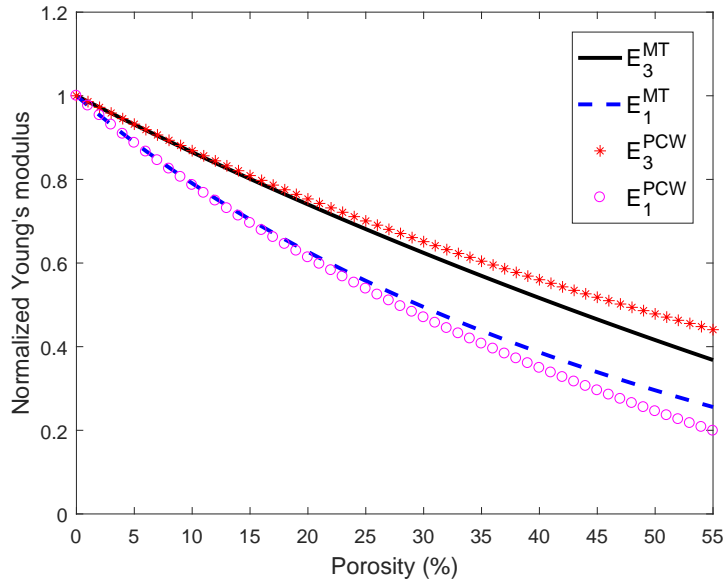


Figure 2.9: The prediction for Young's modulus of extruded bricks

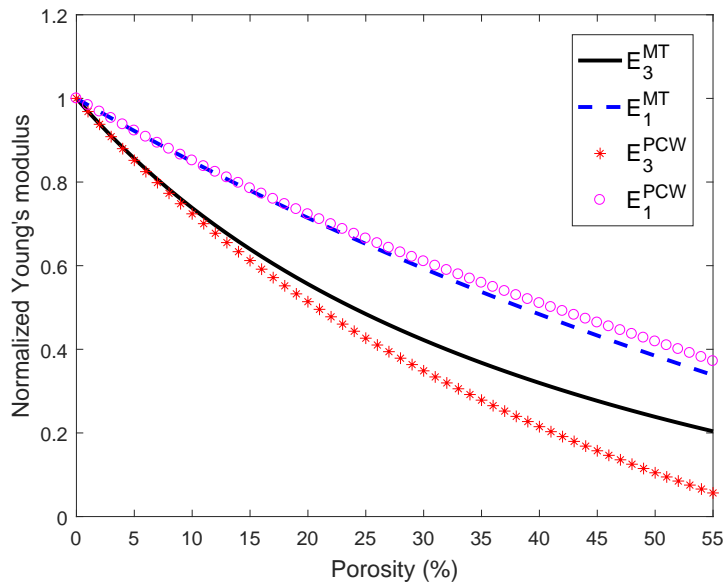


Figure 2.10: The prediction for Young's modulus of molded bricks

## 2.7 Calibrations and experimental validations

The effective elastic properties derived by homogenization approaches have been analyzed above. In this part, calibrations and experimental validations are implemented by an optimization software named *modeFRONTIER*, which is especially applied for the multi-

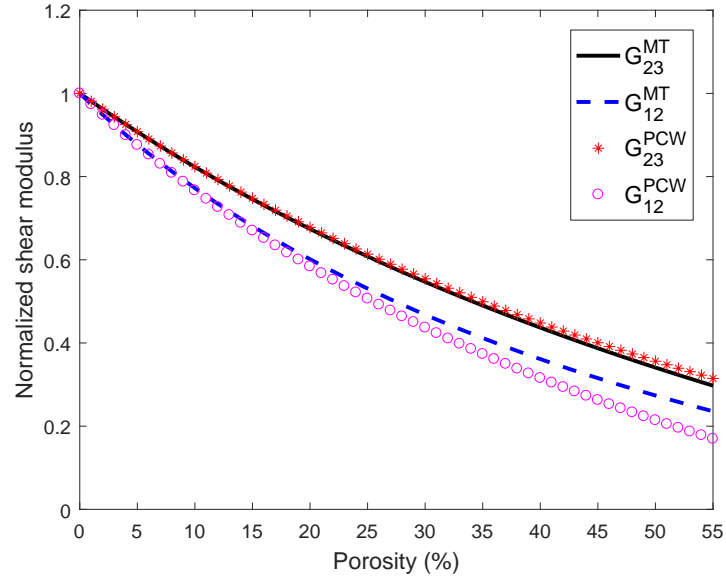


Figure 2.11: The prediction for shear modulus of extruded bricks

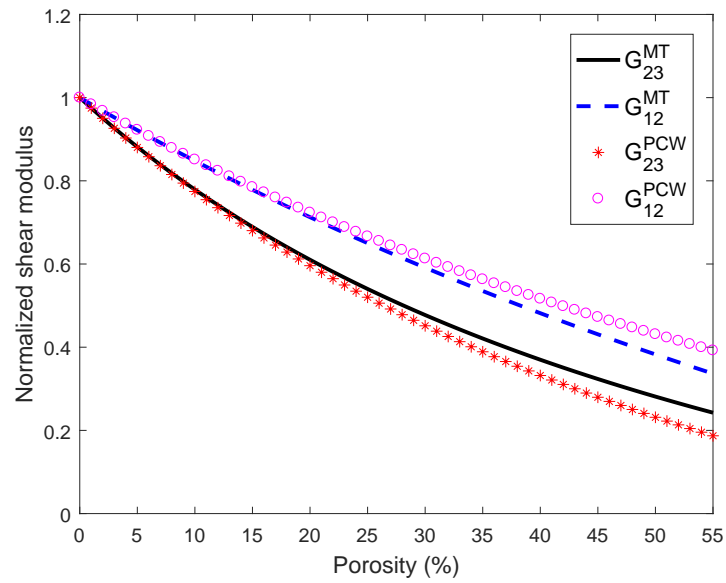


Figure 2.12: The prediction for shear modulus of molded bricks

objective optimization.

Due to lacking of enough material parameters of fired clay bricks, design factors are:  $E_s$ ,  $\nu_s$ ,  $X$ . In DOE Properties, *Sobol* algorithm [65] based on a pseudo random sequence is chosen to generate 4 discrete initial values and to fill the design space. For our non-linear problem, we use the more efficient SIMPLEX algorithm [66], which differs from a traditional simplex method for linear programming. A Matlab subscript constructing the

process from input variables to an output variable is imported into the workflow, in which the sum of squares of the difference between experimental data and predicted values is defined as the output variable  $Ferr$ . In the last of the workflow, the minimized demand of  $Ferr$  is set to achieve the least square. The workflow in *modeFRONTIER* is developed and shown in Figure 2.13:

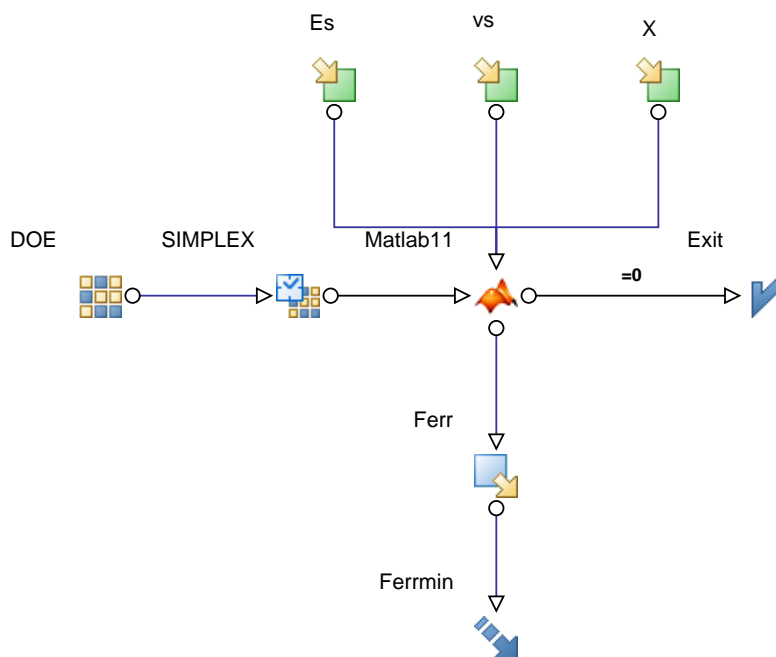


Figure 2.13: The workflow of calibration in *modeFRONTIER*

Figure 2.14 and Figure 2.15 show that the comparison for Young's modulus between our prediction and experimental data of extruded bricks [7]. Unknown parameters are calibrated by means of two points on two different axes under the condition of  $f_p = 27.9\%$ . Other experimental results in this figure are used to validate our prediction. For the 1st group of data containing 10% sands in Figure 2.14, we choose the common calibrated values of MT and PCW schemes and keep  $Ferr$  the least. The values of calibrated parameters are:  $X = 1.4$ ,  $E_s = 32000$  MPa,  $\nu_s = 0.09$ ,  $Ferr = 1.54 \times 10^4$ . Likewise, in Figure 2.15, we calibrate two points corresponding to  $f_p = 29.6\%$  and compare our prediction with other points. The values of calibrated parameters are:  $X = 1.4$ ,  $E_s = 30400$  MPa,  $\nu_s = 0.06$ ,  $Ferr = 6.17 \times 10^3$ . It should be noted that the additives (wheat straw residues and olive stone flour) are not only used to create micro-voids, but also used to mix with clay in order to reduce the thermal conductivity of solid matrix, which also leads to the reduction of mechanical properties. Consequently, it is reasonable that the prediction for Young's modulus is greater than most experimental results in the two figures. Moreover, the PCW estimate shows the anisotropic ratio more closer to experimental results.

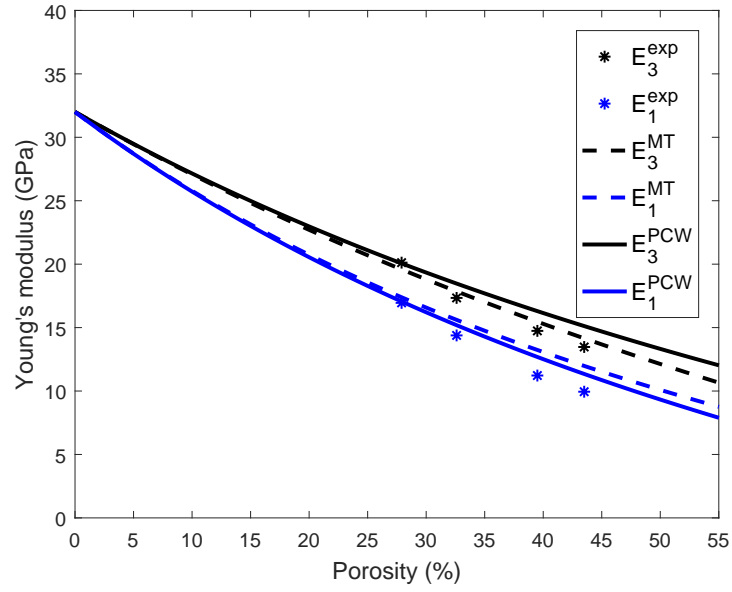


Figure 2.14: 10% sands

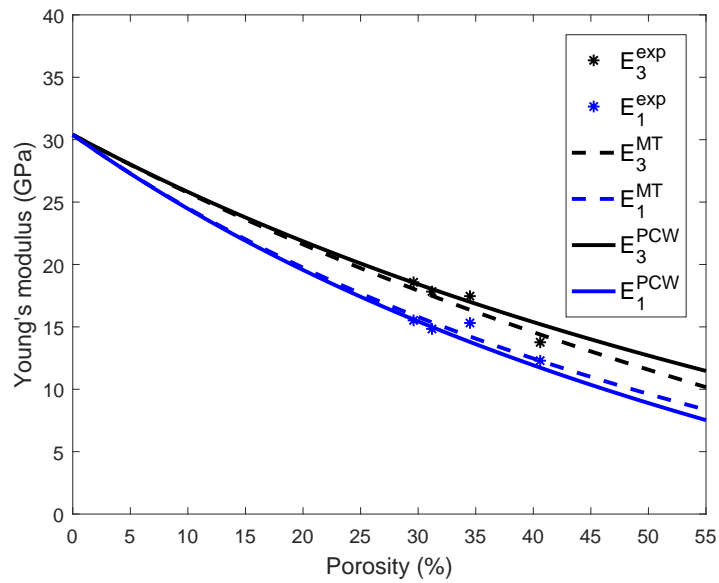


Figure 2.15: 5% sands

## 2.8 Conclusions

In this chapter, we not only build the relations between elastic properties and porosity, but also analyze the effect of shape and spatial distribution of micropores on elastic properties. From the validations, there is a good agreement between our prediction and experimental

results. We can give some conclusions, as follows:

Firstly, porosity is the most important influence factor weakening the elastic properties of fired clay bricks. With the rising of porosity, the variations of elastic moduli have been given in our results.

Secondly, besides porosity, the shape of micropore also has a notable impact on elastic properties according to our results. The aspect ratio of micropores is the fundamental reason causing the transverse isotropy of fired clay bricks. From the predictions, Young's modulus on the major axis is always larger than those on other orientations. Young's modulus on the minor axis is the smallest. The aspect ratio of micropores has a much stronger influence on Young's modulus parallel to the symmetric axis than that in other directions. For extruded bricks, the shear modulus in the plane perpendicular to the isotropic plane is greater than those in other planes. For molded bricks, the conclusion is on the contrary. The aspect ratio affects the shear modulus in the isotropic plane more clearly. With the increase of aspect ratio,  $E_3$  rises but  $G_{12}$  decreases.

Thirdly, by the comparison of results from MT and PCW schemes, PCW scheme considering the spatial distribution of micropores exhibits the more conspicuous anisotropy than the prediction by MT estimate. It means that the spatial distribution of micropores is an important factor for elastic properties.

In terms of numerical results, it is feasible to optimize the elastic properties of fired clay bricks by changing the volume fraction, the shape or the spatial distribution of micropores. To achieve a compromise between mechanical and thermal properties, the influence of micropores on thermal conductivity will be studied in Chapter 3.



# The effective thermal conductivity of fired clay bricks

---

## Contents

<b>3.1</b>	<b>Introduction . . . . .</b>	<b>59</b>
<b>3.2</b>	<b>Homogenization for stationary linear thermal conductivity . . .</b>	<b>60</b>
<b>3.3</b>	<b>Schemes of the effective thermal conductivity tensor . . . . .</b>	<b>63</b>
3.3.1	The Mori-Tanaka estimate of the thermal conductivity . . . . .	63
3.3.2	The Ponte Castañeda-Willis estimate of the thermal conductivity . .	64
<b>3.4</b>	<b>The prediction for effective thermal conductivity of fired clay bricks . . . . .</b>	<b>64</b>
3.4.1	The effective thermal conductivity tensor by Mori-Tanaka estimate .	65
3.4.2	The effective thermal conductivity tensor by Ponte Castañeda-Willis estimate . . . . .	67
<b>3.5</b>	<b>The prediction for thermal conductivity and calibrations . . . .</b>	<b>68</b>
3.5.1	The relationship between thermal conductivity and porosity . . . . .	68
3.5.2	Calibrations and validations for thermal conductivity . . . . .	70
<b>3.6</b>	<b>Conclusions . . . . .</b>	<b>73</b>

---

## 3.1 Introduction

In the preceding chapter, the effective elastic properties of fired clay bricks have been analyzed by homogenization method. In order to find the balance between heat preserving and mechanical capacity, the effective thermal conductivity will be studied in this chapter, which is a very important index to measure the ability of heat transfer. Similar to the elastic properties, the problem of linearly static heat conduction can be also solved by homogenization theory. Eshelby's problem is originally applied in linear microelasticity.

However, the thermal conduction phenomena is adapted to the higher order microelasticity problem [67, 68].

In the theoretical part, the problem of the linearly static heat conduction is introduced firstly. Secondly, the inhomogeneity problem and Eshelby's solution are explained to solve the linear thermal conduction problem. Then, two homogenization schemes (MT and PCW) for effective thermal conductivity are will be given in detail.

Based on the research objective, the same representative volume element with Chapter 2 is taken to analyzed the influence of micropores on the macroscopic thermal conductivity. Next, the numerical implementation for theoretical estimates is carried out to show the effect of micropores on effective thermal conductivity, including porosity, shape and spatial distribution of micropores. The predicted differences between different schemes are also compared. Then, parameter calibrations and experimental validations are achieved. Lastly, we conclude the effect of micropores on thermal conductivity of fired clay bricks.

## 3.2 Homogenization for stationary linear thermal conductivity

In this part, the micro-macro scale transformation of homogenization of thermal conductivity for porous fired clay bricks will be interpreted in detail.

We consider RVE of fired clay bricks as the domain  $\Omega$ . The boundary of RVE is  $\partial\Omega$  which undergoes the macroscopic homogeneous thermal gradient  $\underline{grad}T$ . We adopt  $\underline{q}(\underline{x})$  and  $\underline{grad}T(\underline{x})$  to represent the microscopic heat flux vector and the microscopic thermal gradient field vector, respectively.  $\underline{\lambda}(\underline{x})$  denotes the microscopic second-order thermal conductivity tensor. The problem for thermal conduction is analogous to that for elasticity. For the same RVE as shown in Chapter 2, the equations of localization can be expressed compared with (2.2):

$$\begin{cases} \underline{div}\underline{q}(\underline{x}) = 0 \\ \underline{q}(\underline{x}) = -\underline{\lambda}(\underline{x}) \cdot \underline{grad}T(\underline{x}) \\ T(\underline{x}) = \underline{grad}T \cdot \underline{x}, \quad \forall \underline{x} \in \partial\Omega \end{cases} \quad (3.1)$$

Using  $T(\underline{x}) = \underline{grad}T \cdot \underline{x}$  and integrating by parts, it is readily to yield:

$$\int_{\Omega} \frac{\partial T}{\partial x_j} d\Omega = \int_{\partial\Omega} T n_j dS = \underline{grad}T_i |\Omega| \quad (3.2)$$

in which  $T(\underline{x}) = \underline{grad}T \cdot \underline{x}$  has been used. It is sufficient to derive the relationship between

macroscopic and microscopic thermal gradient vectors by averaging and (3.2):

$$\langle \underline{gradT}(\underline{x}) \rangle = \frac{1}{|\Omega|} \int_{\Omega} \underline{gradT}(\underline{x}) d\Omega = \frac{1}{|\Omega|} \int_{\Omega} \frac{\partial T}{\partial x_j} d\Omega = \underline{gradT} \quad (3.3)$$

The macroscopic thermal flux as the microscopic volume averaging:

$$\underline{Q} = \langle \underline{q}(\underline{x}) \rangle \quad (3.4)$$

Homogenization aims to acquire the equivalent macroscopic thermal conductivity based on micro-structure information of heterogeneous material. The microscopic temperature gradient  $\underline{gradT}(\underline{x})$  and the macroscopic temperature gradient  $\underline{gradT}$  can be related together by a second-order tensor (also named, concentration tensor or localization tensor)  $\underline{A}(\underline{x})$ .

$$\underline{gradT}(\underline{x}) = \underline{A}(\underline{x}) \cdot \underline{gradT} \quad (3.5)$$

By the volume averaging operations for (3.5), it follows that:

$$\langle \underline{A}(\underline{x}) \rangle = \underline{\delta} \quad (3.6)$$

Here, the tensor  $\underline{A}$  is symmetric:

$$A_{ij} = A_{ji} \quad (3.7)$$

Combining (3.1) and (3.4), we obtain:

$$\underline{Q} = \langle \underline{q}(\underline{x}) \rangle = - \langle \underline{\lambda}(\underline{x}) \cdot \underline{gradT}(\underline{x}) \rangle \quad (3.8)$$

Substituting (3.5) into (3.8) yields:

$$\underline{Q} = - \langle \underline{\lambda}(\underline{x}) \cdot \underline{A}(\underline{x}) \cdot \underline{gradT} \rangle = - \langle \underline{\lambda}(\underline{x}) \cdot \underline{A}(\underline{x}) \rangle \cdot \underline{gradT} = - \underline{\lambda}^{hom} \cdot \underline{gradT} \quad (3.9)$$

where the second-order effective thermal conductivity tensor is:

$$\underline{\lambda}^{hom} = \langle \underline{\lambda}(\underline{x}) \cdot \underline{A}(\underline{x}) \rangle \quad (3.10)$$

In the same way, under the boundary condition of homogeneous heat flux on the  $\partial\Omega$ , we have:

$$\underline{gradT} = - \underline{S}^{hom} \cdot \underline{Q} \quad (3.11)$$

with

$$\underline{\underline{S}}^{hom} = \langle \underline{S}(\underline{x}) \cdot \underline{B}(\underline{x}) \rangle \quad (3.12)$$

$\underline{\underline{S}}^{hom}$  is the second-order effective thermal resistance tensor.  $\underline{S}(\underline{x})$  is the microscopic thermal resistance tensor. The relationship between the thermal conductivity tensor and the thermal resistance tensor is:

$$\underline{\lambda} \cdot \underline{S} = \underline{\delta} \quad (3.13)$$

$\underline{B}(\underline{x})$  is the second-order concentration tensor for heat flux. It also has:

$$\langle \underline{B}(\underline{x}) \rangle = \underline{\delta} \quad (3.14)$$

and

$$B_{ij} = B_{ji} \quad (3.15)$$

It should be pointed out that it is impossible to calculate exact solutions for concentration tensors  $\underline{A}(\underline{x})$  and  $\underline{B}(\underline{x})$  at all points of material. For a RVE composed of matrix and inclusions, it is assumed that all properties are same in the  $r$ -th phase. We define  $|\Omega_r|$  as the volume of the  $r$ -th phase in the material.  $\underline{\lambda}_r$  is the thermal conductivity tensor in the  $r$ -th phase. The concentration tensors  $\underline{A}(\underline{x})$  and  $\underline{B}(\underline{x})$  can be replaced by  $\underline{A}_r$  and  $\underline{B}_r$ . Based on these above, we can have the following set of expressions:

$$\left\{ \begin{array}{l} \text{div} \underline{q}_r = 0 \\ \underline{q}_r = -\underline{\lambda}_r \cdot \underline{\text{grad}} T_r \\ T_r = \underline{\text{grad}} T \cdot \underline{x}, \quad \forall \underline{x} \in \partial\Omega \end{array} \right. \quad (3.16)$$

The localization equation:

$$\underline{\text{grad}} T_r = \underline{A}_r \cdot \underline{\text{grad}} T \quad (3.17)$$

According to the volume averaging, it has:

$$\sum_{r=0}^N f_r \cdot \underline{A}_r = \underline{\delta} \quad (3.18)$$

where  $f_r$  is the volume fraction of the  $r$ -th phase.

The second-order effective thermal conductivity tensor is:

$$\underline{\underline{\lambda}}^{hom} = \sum_{r=0}^N f_r \cdot \underline{\lambda}_r \cdot \underline{A}_r \quad (3.19)$$

where the localization tensor in the problem of single inclusion can be written as (see Appendix D):

$$\underline{\underline{A}}_r = [\underline{\underline{\delta}} + \underline{\underline{P}}_r^\epsilon \cdot (\underline{\underline{\lambda}}_r - \underline{\underline{\lambda}}_s)]^{-1} \quad (3.20)$$

where the second-order tensor  $\underline{\underline{P}}_r^\epsilon$  can be expressed by the following relation:

$$\underline{\underline{P}}_r^\epsilon = \underline{\underline{S}}_r^\epsilon \cdot (\underline{\underline{\lambda}}_s)^{-1} \quad (3.21)$$

Like stiffness tensor, the second-order thermal conductivity tensor is dependent on the second-order concentration tensor  $\underline{\underline{A}}_r$ . Next, we will introduce three classical concentration tensors by homogenization approaches.

### 3.3 Schemes of the effective thermal conductivity tensor

Similarly, the problem of multi-inclusions in thermal conductivity can be also regarded as the problem of single inclusion when constructing the local relations. The solution of Eshelby inhomogeneity problem has been thoroughly derived in the previous part. In this part, two different homogenization schemes for thermal conductivity will be interpreted.

#### 3.3.1 The Mori-Tanaka estimate of the thermal conductivity

Unlike the dilute scheme, the Mori-Tanaka scheme considers the interactions between inclusions, and fits for the case of moderate concentration of inclusions [57]. It means that the thermal gradient boundary condition of the  $r$ th-phase inclusion is no longer  $\underline{\underline{grad}}T$ . We assume that the inclusion suffers a thermal gradient  $\underline{\underline{grad}}T^0$  at infinity.

The thermal gradient vector of the  $r$ th-phase inclusion is:

$$\underline{\underline{grad}}T_r = \underline{\underline{A}}_r^0 \cdot \underline{\underline{grad}}T^0 \quad (3.22)$$

where the second-order localization tensor of the polarization was given by (3.20).

According to the law of average, we have:

$$\underline{\underline{grad}}T = \langle \underline{\underline{grad}}T \rangle = \sum_{r=0}^N f_r \underline{\underline{grad}}T_r = \left( f_s \underline{\underline{\delta}} + \sum_{r=1}^N f_r \underline{\underline{A}}_r^0 \right) \cdot \underline{\underline{grad}}T^0 \quad (3.23)$$

The thermal gradient boundary condition of the  $r$ th-phase inclusion is:

$$\underline{grad}T^0 = \left[ f_s \underline{\delta} + \sum_{r=1}^N f_r \underline{A}_r^0 \right]^{-1} \cdot \underline{grad}T \quad (3.24)$$

Substituting (3.24) into (3.22) yields the following relationship between the thermal gradient of the  $r$ th-phase inclusion and the thermal gradient boundary of RVE:

$$\underline{grad}T_r = \underline{A}_r^{MT} \cdot \underline{grad}T \quad (3.25)$$

The second-order concentration tensor of thermal gradient in the equation (3.25) is:

$$\underline{A}_r^{MT} = \left[ \underline{\delta} + \underline{P}_r^\epsilon \cdot (\underline{\lambda}_r - \underline{\lambda}_s) \right]^{-1} \cdot \left[ f_s \underline{\delta} + \sum_{w=1}^N f_w \underline{A}_w^0 \right]^{-1} \quad (3.26)$$

### 3.3.2 The Ponte Castañeda-Willis estimate of the thermal conductivity

The model, which is based on the extension of the Hashin-Shtrikman bound, separates the shape of inclusion and the spatial distribution of inclusion by two independent tensor functions [58]. The second-order concentration tensor of thermal gradient of the  $r$ -th phase is:

$$\underline{A}_r^{PCW} = \left[ \underline{\delta} + \underline{P}_r^\epsilon \cdot (\underline{\lambda}_r - \underline{\lambda}_s) \right]^{-1} \cdot \left\{ f_s \underline{\delta} + \sum_{r=1}^N f_r \left[ \underline{\delta} + (\underline{P}_r^\epsilon - \underline{P}_r^d) \cdot (\underline{\lambda}_r - \underline{\lambda}_s) \right] \cdot \left[ \underline{\delta} + \underline{P}_r^\epsilon \cdot (\underline{\lambda}_r - \underline{\lambda}_s) \right]^{-1} \right\}^{-1} \quad (3.27)$$

where the subscript  $\epsilon$  indicates the shape and  $d$  denotes the spatial distribution.  $\underline{P}_r^\epsilon$  is the shape tensor of the  $r$ -th phase.  $\underline{P}_r^\epsilon = \underline{S}_r^\epsilon \cdot (\underline{\lambda}_s)^{-1}$ , and  $\underline{S}_r^\epsilon$  is second-order Eshelby's tensor of the  $r$ -th phase.  $\underline{P}_r^d$  represents the spatial distribution tensor of the  $r$ -th phase.

## 3.4 The prediction for effective thermal conductivity of fired clay bricks

In this part, the effective thermal conductivity tensors of porous fired bricks are derived by different estimates. The approach of homogenization allows us to determine the influence of geometry of micropores on thermal conductivity. As the micro-structure showed, the

micropores of extruded bricks and moulded bricks are represented by prolate spheroid and oblate spheroid, respectively. The spatial distribution of the micropores is regarded as spherical distribution. The orientation of micropores in the isotropic glassy matrix induces the transversely isotropic thermal conductivity. The solution of second-order tensor  $\underline{\underline{P}}_p^\epsilon$  for spheroidal micropores in the isotropic matrix can be found in [67] and [54].

$$\underline{\underline{P}}_p^\epsilon = \frac{V}{\lambda_s} (\underline{e}_1 \otimes \underline{e}_1 + \underline{e}_2 \otimes \underline{e}_2) + \frac{1-2V}{\lambda_s} \underline{e}_3 \otimes \underline{e}_3 \quad (3.28)$$

According to [46], we take  $\underline{e}_3 = \underline{n}$  as the unit vector normal to isotropic plane for transversely isotropic materials. The second-order tensor  $\underline{\underline{P}}_p^\epsilon$  can be also written as:

$$\underline{\underline{P}}_p^\epsilon = \frac{V}{\lambda_s} (\underline{\delta} - \underline{n} \otimes \underline{n}) + \frac{1-2V}{\lambda_s} \underline{n} \otimes \underline{n} \quad (3.29)$$

where  $V$  is dependent on the aspect ratio  $X = m_3/m_1$ .

$$V = \begin{cases} \frac{1}{2} \left[ 1 + \frac{1}{X^2-1} \left( 1 - \frac{1}{2\chi_1} \ln \left( \frac{1+\chi_1}{1-\chi_1} \right) \right) \right], & \text{if } X \geq 1 \\ \frac{1}{3}, & \text{if } X = 1 \\ \frac{1}{2} \left[ 1 + \frac{1}{X^2-1} \left( 1 - \frac{1}{\chi_2} \arctan(\chi_2) \right) \right], & \text{if } X \leq 1 \end{cases} \quad (3.30)$$

with

$$\chi_2^2 = -\chi_1^2 = \frac{1}{X^2} - 1 \quad (3.31)$$

### 3.4.1 The effective thermal conductivity tensor by Mori-Tanaka estimate

Based on the equation (3.22) mentioned in 3.3.1, the tensors  $A_r^0$  for our case are calculated at first:

$$\begin{aligned} \underline{\underline{A}}_s^0 &= \underline{\underline{\delta}} \\ \underline{\underline{A}}_p^0 &= \left( \underline{\underline{\delta}} + \underline{\underline{P}}_p^\epsilon \cdot (\underline{\underline{\lambda}}_p - \underline{\underline{\lambda}}_s) \right)^{-1} \end{aligned} \quad (3.32)$$

Combining (3.29) and (??), we can obtain the same expression for  $\underline{\underline{A}}_p^0$  as (??):

$$\underline{\underline{A}}_p^0 = \frac{\lambda_s}{\lambda_s + V(\lambda_p - \lambda_s)} (\underline{\underline{\delta}} - \underline{n} \otimes \underline{n}) + \frac{\lambda_s}{\lambda_s + (1-2V)(\lambda_p - \lambda_s)} \underline{n} \otimes \underline{n} \quad (3.33)$$

The expression of the volume averaging, it is written as:

$$\sum_{i=0}^1 f_i \underline{\underline{A}}_i^0 = f_s \underline{\underline{\delta}} + f_p \underline{\underline{A}}_p^0 \quad (3.34)$$

Substituting (3.33) into (3.34), it derives:

$$\begin{aligned} \sum_{i=0}^1 f_i \underline{\underline{A}}_i^0 &= \left[ f_s + \frac{\lambda_s f_p}{\lambda_s + V(\lambda_p - \lambda_s)} \right] (\underline{\underline{\delta}} - \underline{\underline{n}} \otimes \underline{\underline{n}}) \\ &+ \left[ f_s + \frac{\lambda_s f_p}{\lambda_s + (1 - 2V)(\lambda_p - \lambda_s)} \right] \underline{\underline{n}} \otimes \underline{\underline{n}} \end{aligned} \quad (3.35)$$

Calculating the inverse for equation (3.35) in terms of equation (??), it is:

$$\begin{aligned} \left( \sum_{i=0}^1 f_i \underline{\underline{A}}_i^0 \right)^{-1} &= \left[ f_s + \frac{\lambda_s f_p}{\lambda_s + V(\lambda_p - \lambda_s)} \right]^{-1} (\underline{\underline{\delta}} - \underline{\underline{n}} \otimes \underline{\underline{n}}) \\ &+ \left[ f_s + \frac{\lambda_s f_p}{\lambda_s + (1 - 2V)(\lambda_p - \lambda_s)} \right]^{-1} \underline{\underline{n}} \otimes \underline{\underline{n}} \end{aligned} \quad (3.36)$$

Inserting equations (3.33) and (3.36) into (3.26), the concentration tensor for micropores is obtained:

$$\begin{aligned} \underline{\underline{A}}_p^{MT} &= \frac{\lambda_s}{\lambda_s + V(\lambda_p - \lambda_s)} \left[ f_s + \frac{\lambda_s f_p}{\lambda_s + V(\lambda_p - \lambda_s)} \right]^{-1} (\underline{\underline{\delta}} - \underline{\underline{n}} \otimes \underline{\underline{n}}) \\ &+ \frac{\lambda_s}{\lambda_s + (1 - 2V)(\lambda_p - \lambda_s)} \left[ f_s + \frac{\lambda_s f_p}{\lambda_s + (1 - 2V)(\lambda_p - \lambda_s)} \right]^{-1} \underline{\underline{n}} \otimes \underline{\underline{n}} \end{aligned} \quad (3.37)$$

The effective thermal conductivity tensor for two phases can be expressed as:

$$\underline{\underline{\lambda}}^{MT} = \sum_{r=0}^1 f_r \underline{\underline{\lambda}}_r \cdot \underline{\underline{A}}_r^{MT} = \underline{\underline{\lambda}}_s + f_p (\underline{\underline{\lambda}}_p - \underline{\underline{\lambda}}_s) \cdot \underline{\underline{A}}_p^{MT} \quad (3.38)$$

Replacing (3.37) into (3.38), the second-order effective thermal conductivity tensor can be derived, as follows:

$$\begin{aligned} \underline{\underline{\lambda}}^{MT} &= \left[ \lambda_s + \frac{f_p \lambda_s (\lambda_p - \lambda_s)}{\lambda_s + (1 - f_p) V(\lambda_p - \lambda_s)} \right] (\underline{\underline{\delta}} - \underline{\underline{n}} \otimes \underline{\underline{n}}) \\ &+ \left[ \lambda_s + \frac{f_p \lambda_s (\lambda_p - \lambda_s)}{\lambda_s + (1 - f_p)(1 - 2V)(\lambda_p - \lambda_s)} \right] \underline{\underline{n}} \otimes \underline{\underline{n}} \end{aligned} \quad (3.39)$$

The effective thermal conductivities on the two axial directions are, respectively:

$$\lambda_{11}^{MT} = \lambda_{22}^{MT} = \lambda_s + \frac{f_p \lambda_s (\lambda_p - \lambda_s)}{[[1 - (1 - f_p)V]\lambda_s + (1 - f_p)V\lambda_p} \quad (3.40)$$

and

$$\lambda_{33}^{MT} = \lambda_s + \frac{f_p \lambda_s (\lambda_p - \lambda_s)}{[1 - (1 - f_p)(1 - 2V)]\lambda_s + (1 - f_p)(1 - 2V)\lambda_p} \quad (3.41)$$

where  $V$  has been given (3.30).

### 3.4.2 The effective thermal conductivity tensor by Ponte Castañeda-Willis estimate

The spatial distribution of micropores have to be considered in the PCW scheme. It is assumed that the spatial distribution of micropores is spherical, so the tensorial function representing the spatial distribution is identical with the shaping function of spheroidal voids. That is:

$$\underline{\underline{P}}_p^d = \frac{1}{3}(\underline{\underline{\lambda}}_s)^{-1} \quad (3.42)$$

Substituting (3.29) and (3.42) into (3.27), it yields the second-order concentration tensor of micropores:

$$\begin{aligned} \underline{\underline{A}}_p^{PCW} &= \frac{3\lambda_s}{(3V - f_p)\lambda_p + (3 - 3V + f_p)\lambda_s} (\underline{\underline{\delta}} - \underline{\underline{n}} \otimes \underline{\underline{n}}) \\ &+ \frac{3\lambda_s}{(3 - 6V - f_p)\lambda_p + (6V + f_p)\lambda_s} \underline{\underline{n}} \otimes \underline{\underline{n}} \end{aligned} \quad (3.43)$$

The effective thermal conductivity tensor derived from PCW model is:

$$\begin{aligned} \underline{\underline{\lambda}}^{PCW} &= \left[ \lambda_s + \frac{3f_p(\lambda_p - \lambda_s)\lambda_s}{(3V - f_p)\lambda_p + (3 - 3V + f_p)\lambda_s} \right] (\underline{\underline{\delta}} - \underline{\underline{n}} \otimes \underline{\underline{n}}) \\ &+ \left[ \lambda_s + \frac{3f_p(\lambda_p - \lambda_s)\lambda_s}{(3 - 6V - f_p)\lambda_p + (6V + f_p)\lambda_s} \right] \underline{\underline{n}} \otimes \underline{\underline{n}} \end{aligned} \quad (3.44)$$

The effective thermal conductivities by PCW estimate on the two axial directions are, respectively:

$$\lambda_{11}^{PCW} = \lambda_{22}^{PCW} = \lambda_s + \frac{3f_p(\lambda_p - \lambda_s)\lambda_s}{(3V - f_p)\lambda_p + (3 - 3V + f_p)\lambda_s} \quad (3.45)$$

and

$$\lambda_{33}^{PCW} = \lambda_s + \frac{3f_p(\lambda_p - \lambda_s)\lambda_s}{(3 - 6V - f_p)\lambda_p + (6V + f_p)\lambda_s} \quad (3.46)$$

where  $V$  was given by (3.30).

## 3.5 The prediction for thermal conductivity and calibrations

### 3.5.1 The relationship between thermal conductivity and porosity

In this part, we will study the relationship between thermal conductivity and porosity for fired clay bricks.

For extruded bricks, the direction 3 represents the extrusion direction, and the direction 1 is on the transversely isotropic plane. We know the thermal conductivity of air  $\lambda_p = 0.026$  W/m·K. Under fixed parameters:  $X = m_3/m_1 = 2$ , the tendency of thermal conductivity is analyzed. Figure 3.1 shows the relationship between thermal conductivity and porosity for extruded fired clay bricks from the three above homogenization schemes. From the figure, we can see that  $\lambda_{33} > \lambda_{11}$ . It means that the thermal conductivity on the major axis is the largest, that on minor axis is the smallest. Comparing the curves, it can be found that the prediction by PCW scheme considering the spatial distribution of micropores shows a much stronger anisotropy than the prediction by MT scheme. It means that the spatial distribution of micropores has an important effect on the thermal conductivity of fired clay bricks.

For moulded bricks, the minor axis of the oblate micropore is on the axis 3. For an aspect ratio  $X = m_3/m_1 = 0.5$ , the prediction of thermal conductivity is shown in Figure 3.2. Similar to extruded bricks, some similar results about molded bricks can be also obtained. The thermal conductivity on the major axis is the largest than those on other orientations, that is  $\lambda_{11}^{PCW} > \lambda_{33}^{PCW}$ . The prediction by PCW estimate gives a greater ratio  $\lambda_{11}/\lambda_{33}$ .

Figure 3.3 and Figure 3.4 show that the comparison for thermal conductivity for extruded and molded bricks by PCW estimate for different aspect ratios. Figure 3.3 predicts the effective thermal conductivity on direction 3. As the decreasing of aspect ratio,  $\lambda_{33}$  decreases more clearly. Figure 3.4 predicts that on direction 1. Comparing the two figures, it can be seen that the aspect ratio has a greater impact on the thermal conductivity on

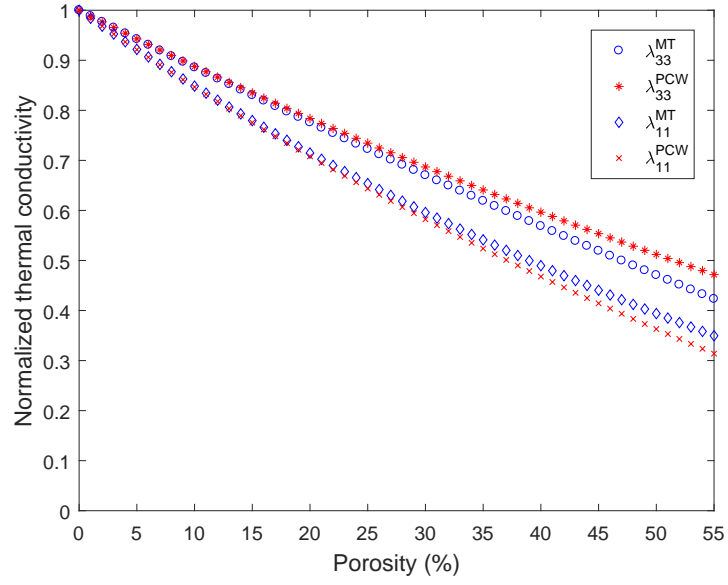


Figure 3.1: The normalized thermal conductivity of extruded bricks

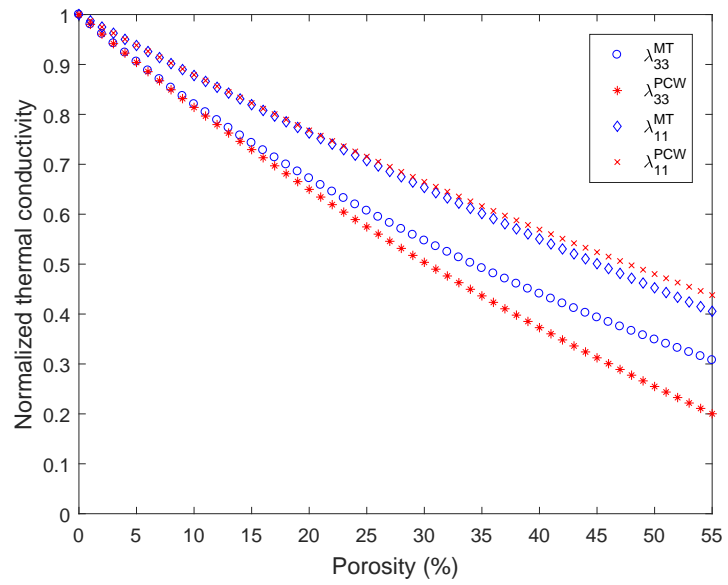


Figure 3.2: The normalized thermal conductivity of molded bricks

the symmetric axis than that on direction 1.

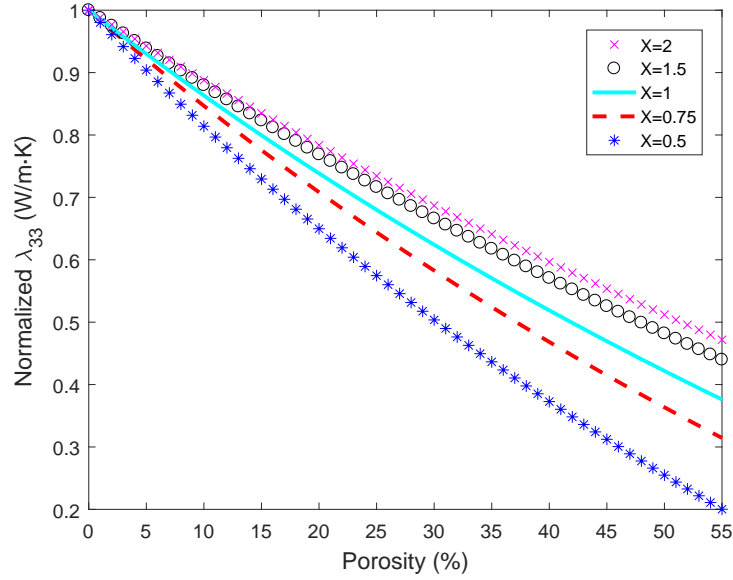


Figure 3.3: The prediction for  $\lambda_{33}$  by Ponte Castañeda-Willis scheme

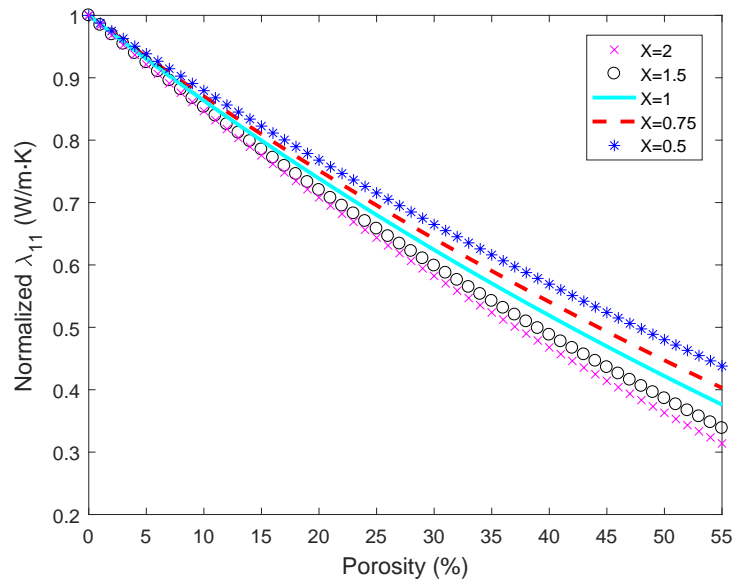


Figure 3.4: The prediction for  $\lambda_{11}$  by Ponte Castañeda-Willis scheme

### 3.5.2 Calibrations and validations for thermal conductivity

For two groups of data from [7], one group corresponds to the content of sands 5% and another corresponds to the content of sands 10%. Here, a two-step homogenization procedure for the evaluation of the effective thermal conductivity of fired clay bricks is performed.

In step 1, we only consider solid phase as the homogeneous and isotropic material. The solid phase is composed of fired clay and sands.

$$\lambda_s = \lambda_{cl} + \frac{3f^{sa}\lambda_{cl}(\lambda_{sa} - \lambda_{cl})}{3f^{sa}\lambda_{cl} + f^{cl}(\lambda_{sa} + 2\lambda_{cl})} \quad (3.47)$$

In step 2, the fired clay brick is made up of two phases, which are solid phases and micropores.

$$\lambda_{11}^{PCW} = \lambda_{22}^{PCW} = \lambda_s + \frac{3f_p(\lambda_p - \lambda_s)\lambda_s}{(3V - f_p)\lambda_p + (3 - 3V + f_p)\lambda_s} \quad (3.48)$$

and

$$\lambda_{33}^{PCW} = \lambda_s + \frac{3f_p(\lambda_p - \lambda_s)\lambda_s}{(3 - 6V - f_p)\lambda_p + (6V + f_p)\lambda_s} \quad (3.49)$$

The following Figure 3.5 and Figure 3.6 illustrate the relationship between thermal conductivity and porosity under different content of sands [7]. The two group of data is measured by hot plate apparatus. We know that the thermal conductivity of voids  $\lambda_p = 0.026$  W/m·K. Because these tested samples for thermal conductivity are same as those for Young's modulus, we take the same aspect ratio of micropores  $X = 1.4$ , which was calibrated in Chapter 2. Figure 3.5 corresponds to the experimental results of 10% sands. We use this group of data to calibrate parameters and obtain:  $\lambda_{cl} = 0.559$  W/m·K and  $\lambda_{sa} = 2.2$  W/m·K. The least square is  $Ferr = 5.95 \times 10^{-3}$ . Making use of calibrated parameters, we predict the thermal conductivity on the 1-axis. We use these obtained parameters to predict the thermal conductivity with 5% sands and compare with another group of data, which is shown in Figure 3.6.

Figure 3.7 and Figure 3.8 show the calibrated and predicted curves by using two groups of data containing 10% and 5% sands [7], respectively. The two groups of data are measured according to NF EN 1745 [7, 12]. We calibrate the parameters according to the data of samples with 10% sands along the 3-axis direction. Similarly, the calibrated parameters are:  $\lambda_{cl} = 0.568$  W/m·K,  $\lambda_{sa} = 1.4$  W/m·K. The error  $Ferr = 5.88 \times 10^{-5}$ . Based on the calibrated parameters, we make the prediction for thermal conductivity of samples with 5% sands and compare with experimental data in Figure 3.8. It can be seen that our estimation can give a reasonable prediction.

Figure 3.9 and Figure 3.10 calibrate the model by PCW estimation according to experimental data on the direction 3 [3]. By using calibrated parameters, the predictions by MT estimation were given to compare with the results from PCW estimation. In Figure 3.9, the fired temperature of experimental samples is at 1000°C. The calibrated parameters are:  $X = 0.63$ ,  $\lambda_s = 1.279$  W/m·K,  $Ferr = 0.00128$ . In Figure 3.10, the experimental samples

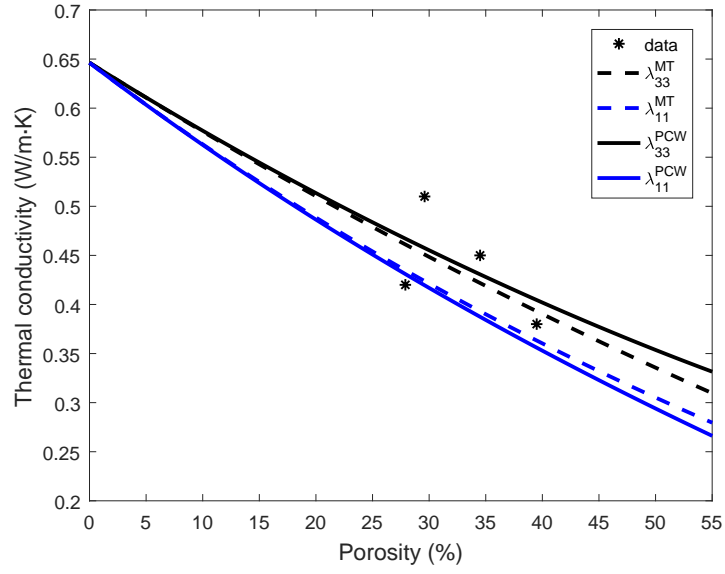


Figure 3.5: The data containing 10% sands (by hot plate apparatus) [7]

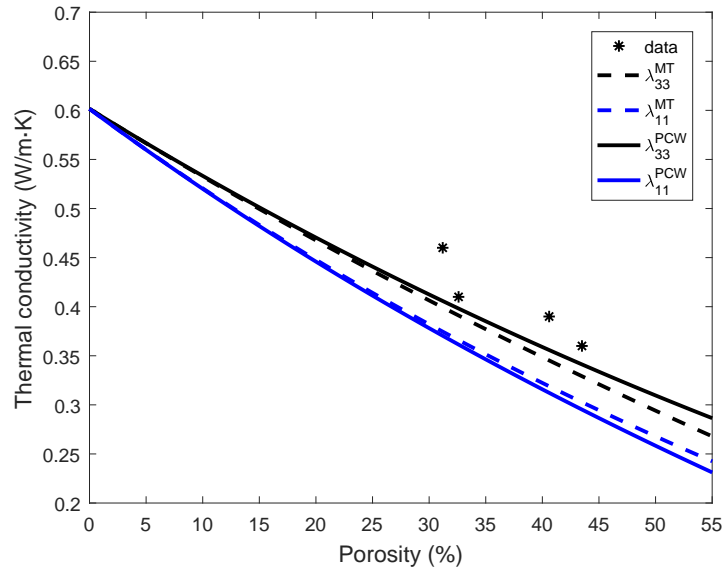


Figure 3.6: The data containing 5% sands (by hot plate apparatus) [7]

were fired at  $1300^{\circ}\text{C}$ , and the group of data corresponds to high porosity. The calibrated parameters are:  $X = 0.69$ ,  $\lambda_s = 0.964 \text{ W/m}\cdot\text{K}$ ,  $Ferr = 0.000822$ . We give the prediction on direction 1, and need the experimental data on the direction 1 to validate.

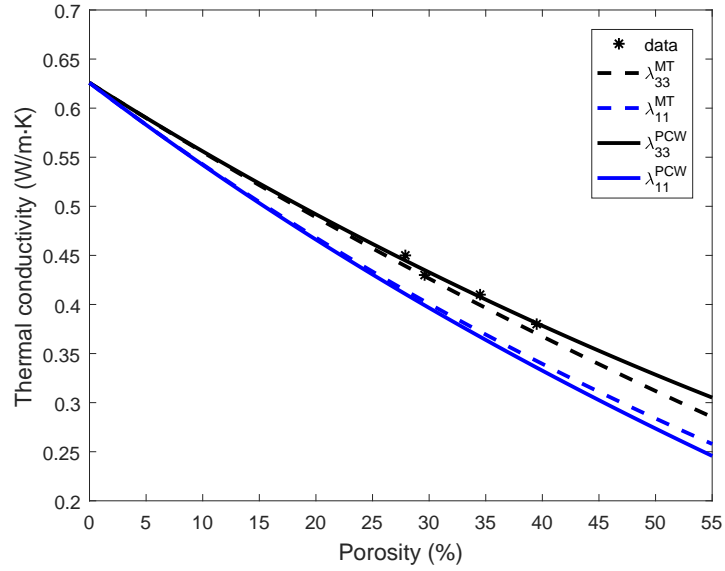


Figure 3.7: The data containing 10% sands (by NF EN 1745) [7]

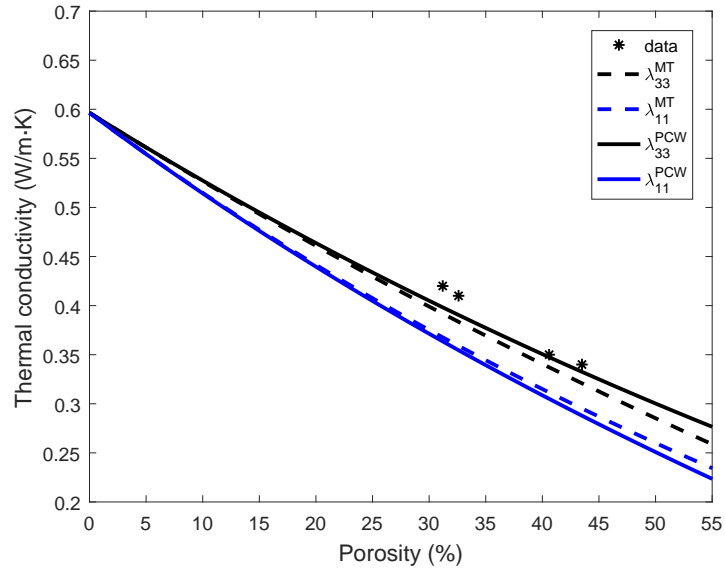


Figure 3.8: The data containing 5% sands (by NF EN 1745) [7]

### 3.6 Conclusions

In this chapter, we analyze the effect of micropores on thermal conductivity of fired clay bricks by three homogenization approaches and obtain the following conclusions:

At first, the effect of porosity on thermal conductivity of fired clay bricks is studied by different homogenization estimates. The results by dilute estimation ignoring the interac-

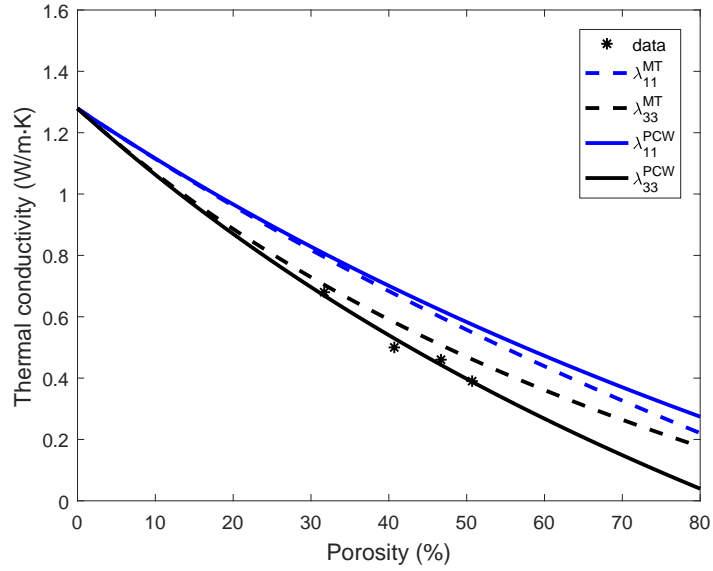


Figure 3.9: The samples fired at 1000°C [3]

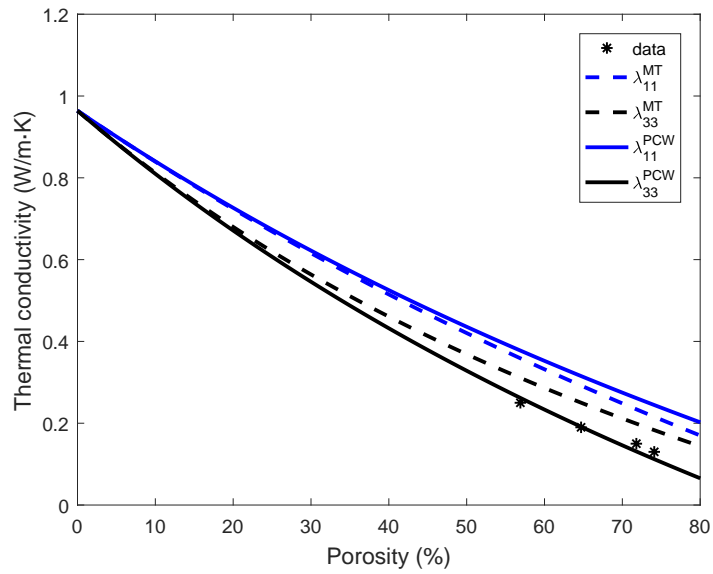


Figure 3.10: The samples fired at 1300°C [3]

tion among micropores exhibit the linear and lower prediction. Compared with the results by MT scheme, the results from PCW scheme show the greater ratio of modulus. It means that the spatial distribution of micropores also plays an important role in anisotropic ratio and cannot be ignored.

Next, the influence of the aspect ratio of micropores on thermal conductivity has been studied. For extruded and molded bricks, the thermal conductivity along the major axis

of micropore is larger than those along other directions. The thermal conductivity on the minor axis of micropores is the smallest. In the two axial directions, the aspect ratio of micropores affects the thermal conductivity along the symmetric axis more obviously.

Combining the analysis in Chapter 2, it is obvious that reducing the thermal conductivity can also cause the decreasing of elastic properties. The optimal determination between mechanical properties and thermal conduction is dependent on the geometry of fired clay bricks and the situation in constructions. Following the analysis of elastic properties and thermal conductivity, the effect of micropores on mechanical strength of fired clay bricks will be studied in Chapter 4.



# The micromechanical damage modeling for fired clay bricks

---

## Contents

<b>4.1</b>	<b>Introduction</b>	<b>77</b>
<b>4.2</b>	<b>The representative volume element (RVE) considering microcracks</b>	<b>78</b>
<b>4.3</b>	<b>The effective stiffness of cracked fired clay bricks</b>	<b>78</b>
4.3.1	The MT estimate for open microcracks	80
4.3.2	The MT estimate for closed microcracks	81
4.3.3	The PCW estimate for open microcracks of isotropic distribution	83
4.3.4	The PCW estimate for closed microcracks of isotropic distribution	85
<b>4.4</b>	<b>Thermodynamic potential and state laws</b>	<b>87</b>
<b>4.5</b>	<b>The study on parameters of the damage model</b>	<b>89</b>
4.5.1	The study on parameter $\eta$	90
4.5.2	The study on parameter $R_0$	91
4.5.3	The study on parameter $f_p$	91
4.5.4	The study on parameter $X$	93
4.5.5	The comparison between PCW scheme and MT scheme	94
<b>4.6</b>	<b>Calibrations and experimental validations of the micromechanical model</b>	<b>96</b>
<b>4.7</b>	<b>Conclusions</b>	<b>98</b>

---

## 4.1 Introduction

A micro-mechanical damage modeling is proposed for fired clay bricks produced by extruding or molding under the uniaxial compressive load. Taking advantage of homogenization schemes implemented in chapter 2, we first extended our previous results to porous

materials with distributed microcracks. We then deduce damage models based on MT and PCW schemes combined with classical thermodynamics approach. The microcracks-induced damage is represented by a microcracks density parameter. Unilateral effects (closure or opening) will be also considered. It is assumed that the orientations of all microcracks are aligned and the spatial distribution of microcracks is spherical. The obtained models are finally calibrated and then validated by comparison with experimental data.

## 4.2 The representative volume element (RVE) considering microcracks

Besides micropores existing in fired clay bricks, microcracks can be generated during the manufacturing process or the service stage and play a crucial role in the mechanical behavior. As the analysis of micro-structure of fired clay bricks [4], this material mainly contains then glassy matrix, silts, micropores and microcracks. For simplicity, all solid phases in fired clay bricks are summarized into the a unique solid matrix. In order to illustrate the heterogeneity and the multi-scale characteristics of fired clay bricks, a representative volume element for microcracked porous fired clay bricks is established and shown in the following Figure 4.1. The RVE of fired clay bricks is constituted of solid matrix, micropores and microcracks at this microscopic scale. The RVE is suitable for both extruded bricks and molded bricks. As mentioned in Chapter 2, for extruded bricks, their shapes are prolate and the long axes of micropores are identical with the extruded direction. The shapes of micropores of molded bricks are oblate and the short axes of micropores are parallel to pressed direction. The shapes of all microcracks are considered penny-shaped, however, their orientations are assumed to be parallel.

## 4.3 The effective stiffness of cracked fired clay bricks

As mentioned before, microcracks have an important influence on the mechanical behavior of cracked porous bricks. Now, we introduce a parameter microcrack density, which is a very important state variable to make predictions in continuum damage mechanics. The  $j$ -th family of microcracks is  $F_j$  relying on the orientation. The aspect ratios of microcracks of all families are assumed to be  $X_c = c/a \ll 1$  (see Figure 4.2). The aspect ratio  $X_c$  will be eliminated in the derivation of homogenized stiffness [69], so that the effective stiffness is not affected by the aspect ratio of microcracks when the later tends to 0. Then, we introduce the microcracks density parameter  $d = Na^3$ , with  $N$  is the number of microcracks by unit volume. The volume fraction of microcracks is denoted  $f_c$  while that of micropores is  $f_p$ . Moreover, the volume fraction of microcracks is written as:

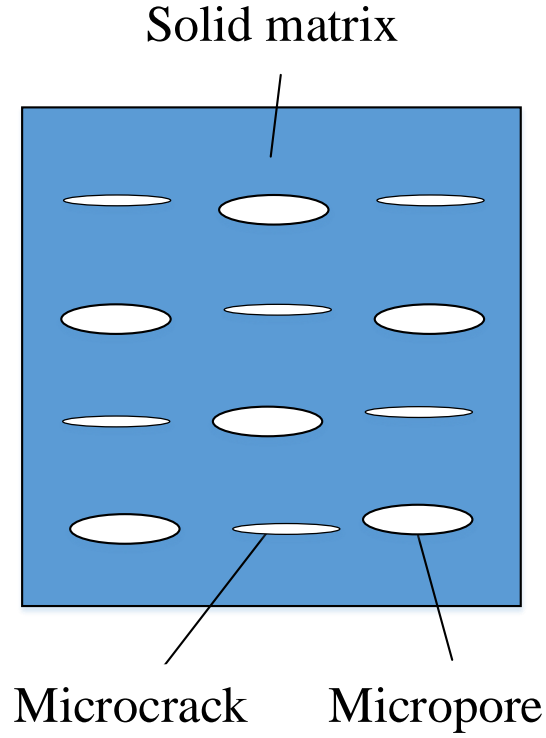


Figure 4.1: The RVE for extruded bricks at one microscale

$$f_c = \frac{4}{3}\pi a^2 c N = \frac{4}{3}\pi d X_c \quad (4.1)$$

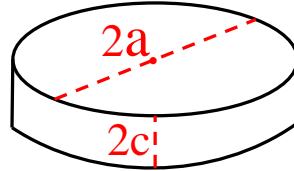


Figure 4.2: The penny-shaped microcrack

Like other brittle materials (see [70, 71]), the mechanical behavior of transversely isotropic fired clay bricks is dependent on the open or closed state of microcracks. Aa microcracks families are composed of open microcracks and closed microcracks, the volume fractions of open and closed microcracks are indicated by  $f_c^{op}$  and  $f_c^{cl}$ , respectively.

We have the following expression for the volume fraction of microcracks:

$$\sum_{j,op} f_{c_j}^{op} + \sum_{j,cl} f_{c_j}^{cl} = f_c \quad (4.2)$$

Based on the definition of homogenization theory, the effective stiffness tensor for the material composed of 3 phases (solid matrix, micropores and microcracks) can be written as:

$$\mathbb{C}^{hom} = \sum_{r=0}^2 f_r \mathbb{C}_r : \mathbb{A}_r \quad (4.3)$$

$f_r$  is the volume fraction of  $r$ -th phase.  $\mathbb{C}_r$  holds for the stiffness tensor of the  $r$ -th phase.  $\mathbb{A}_r$  represents the the strain concentration tensor of  $r$ -th phase. We use subscripts  $s$ ,  $p$  and  $c$  to indicate solid matrix, micropores, and microcracks, respectively. The expansion of equation (4.3) is recast as:

$$\mathbb{C}^{hom} = f_s \mathbb{C}_s : \mathbb{A}_s + f_p \mathbb{C}_p : \mathbb{A}_p + \sum_{j,op} f_{c_j}^{op} \mathbb{C}_{c_j}^{op} : \mathbb{A}_{c_j}^{op} + \sum_{j,cl} f_{c_j}^{cl} \mathbb{C}_{c_j}^{cl} : \mathbb{A}_{c_j}^{cl} \quad (4.4)$$

with:

$$\sum_{r=0}^2 f_r \mathbb{A}_r = \mathbb{I} \quad (4.5)$$

and

$$\sum_{r=0}^2 f_r = 1 \quad (4.6)$$

Note that we only consider unilateral effects of microcracks that all microcracks are open or closed in this chapter. The following parts focus on the estimates of two homogenization schemes considering unilateral effect of microcracks of fired clay bricks.

### 4.3.1 The MT estimate for open microcracks

As showed in Figure 4.1, the simplified RVE contains one family of micropores and one family of microcracks. It is known that  $\mathbb{C}_p = 0$  and  $\mathbb{C}_{op} = 0$ . All microcracks of fired clay bricks are assumed to be open, the localization tensors of micropores and microcracks can be calculated by MT estimation, respectively:

$$\mathbb{A}_p^{MT} = (\mathbb{I} - \mathbb{S}_p^\epsilon)^{-1} : \left[ f_s \mathbb{I} + f_p (\mathbb{I} - \mathbb{S}_p^\epsilon)^{-1} + \frac{4}{3} \pi d \mathbb{T} \right]^{-1} \quad (4.7)$$

and

$$\mathbb{A}_{op}^{MT} = (\mathbb{I} - \mathbb{S}_{op}^\epsilon)^{-1} : \left[ f_s \mathbb{I} + f_p (\mathbb{I} - \mathbb{S}_p^\epsilon)^{-1} + \frac{4}{3} \pi d \mathbb{T} \right]^{-1} \quad (4.8)$$

where the subscript 'p' represents pores and 'op' represents open cracks. Tensor  $\mathbb{T}$  was given in (B.10). Subsequently, it is not difficult to calculate the effective stiffness tensor with open microcracks.

$$\begin{aligned} \mathbb{C}_{op}^{MT}(d) = & \mathbb{C}_s - f_p \mathbb{C}_s : (\mathbb{I} - \mathbb{S}_p^\epsilon)^{-1} : \left[ f_s \mathbb{I} + f_p (\mathbb{I} - \mathbb{S}_p^\epsilon)^{-1} + \frac{4}{3} \pi d \mathbb{T} \right]^{-1} \\ & - \frac{4\pi d}{3} \mathbb{C}_s : \mathbb{T} : \left[ f_s \mathbb{I} + f_p (\mathbb{I} - \mathbb{S}_p^\epsilon)^{-1} + \frac{4}{3} \pi d \mathbb{T} \right]^{-1} \end{aligned} \quad (4.9)$$

The fourth-order effective stiffness tensor considering open microcracks can be indicated by Walpole's notation [63]. The relationships between mechanical constants and open microcrack density  $d$  (damage parameter) can be obtained. Because the orientations of microcracks are aligned with the symmetric 3-axis (extruded or pressed direction), Young's modulus  $E_1(d)$  and shear modulus  $G_{12}(d)$  are always invariants. Poisson's ratios  $\nu_{13}(d)$  and  $\nu_{12}(d)$  are not affected by parameter  $d$ .

Figure 4.3 depicts the relationship between normalized Young's modulus  $E_3(d)$  and microcrack density  $d$ . The relations are drawn under the given parameters:  $f_p = 20\%$  and  $\nu_s = 0.1$ . It is seen that  $E_3(d)$  decreases with the rising of microcrack density  $d$ . During the damage process, the aspect ratio  $X$  affects  $E_3(d)$  of molded bricks more clearly, not that of extruded bricks.

Figure 4.4 exhibits the effect of damage parameter  $d$  on the normalized  $G_{23}(d)$ . When  $X > 1$ , the aspect ratio  $X$  doesn't have an obvious effect on  $G_{23}(d)$ . When  $X < 1$ , the smaller the aspect ratio  $X$  is, the value  $G_{23}(d)$  is lower.

### 4.3.2 The MT estimate for closed microcracks

In this case, it is assumed that all microcracks are closed and the microcracks faces are frictionless. That is to say, these faces only transmit the normal stress and the shear stress between lips is equal to zero. The bulk modulus of microcracks is  $k_{cl} = k_s$  and the shear modulus of microcracks is  $\mu_{cl} = 0$ . It has been known that the stiffness tensor of closed microcracks [72]:

$$\mathbb{C}_{cl} = 3k_s \mathbb{J} \quad (4.10)$$

The concentration tensor for micropores is recast by the following expression:

$$\mathbb{A}_p^{MT} = (\mathbb{I} - \mathbb{S}_p^\epsilon)^{-1} : \left[ f_s \mathbb{I} + f_p (\mathbb{I} - \mathbb{S}_p^\epsilon)^{-1} + \frac{4}{3} \pi d \mathbb{T}' \right]^{-1} \quad (4.11)$$

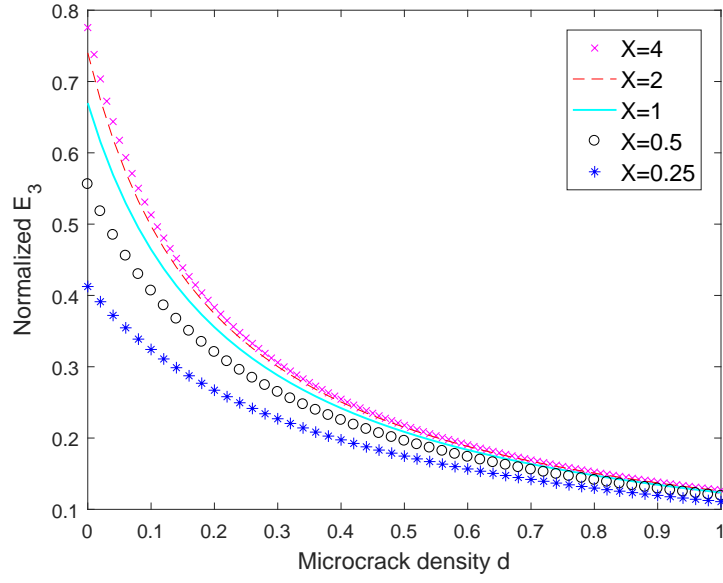


Figure 4.3: The relation between normalized  $E_3$  and  $d$  for open microcracks by MT

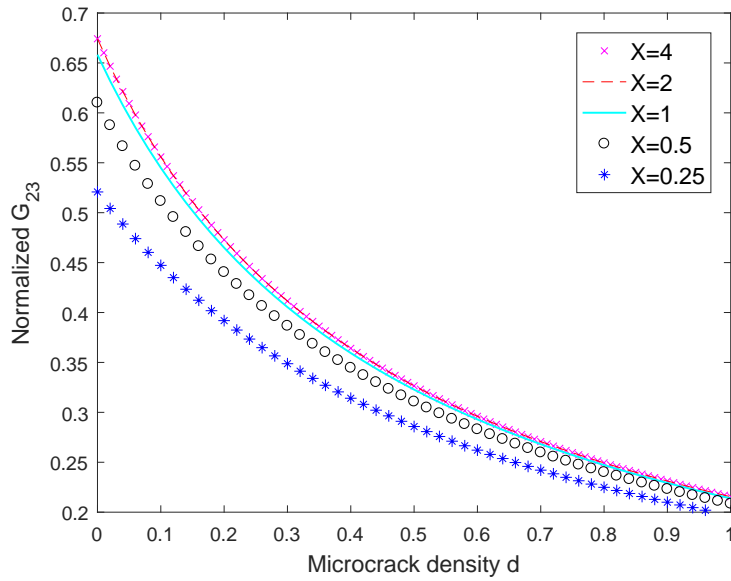


Figure 4.4: The relation between normalized  $G_{23}$  and  $d$  for open microcracks by MT

The concentration tensor for microcracks is simplified by the expression:

$$\mathbb{A}_{cl}^{MT} = (\mathbb{I} - \mathbb{S}_{cl}^e)^{-1} : \left[ f_s \mathbb{I} + f_p (\mathbb{I} - \mathbb{S}_p^e)^{-1} + \frac{4}{3} \pi d \mathbb{T}' \right]^{-1} \quad (4.12)$$

The effective stiffness tensor considering closed microcracks can be written as:

$$\begin{aligned} \mathbb{C}_{cl}^{MT}(d) = & \mathbb{C}_s - f_p \mathbb{C}_s : (\mathbb{I} - \mathbb{S}_p^\epsilon)^{-1} : \left[ f_s \mathbb{I} + f_p (\mathbb{I} - \mathbb{S}_p^\epsilon)^{-1} + \frac{4}{3} \pi d \mathbb{T}' \right]^{-1} \\ & - \frac{8\pi d}{3} \mu_s \mathbb{K} : \mathbb{T}' : \left[ f_s \mathbb{I} + f_p (\mathbb{I} - \mathbb{S}_p^\epsilon)^{-1} + \frac{4}{3} \pi d \mathbb{T}' \right]^{-1} \end{aligned} \quad (4.13)$$

We still take Walpole's notation to describe the fourth-order effective stiffness tensor with closed microcracks. For the case of aligned closed microcracks, the microcrack density  $d$  doesn't affect  $E_3(d)$ ,  $E_1(d)$  and  $G_{12}(d)$ . Moreover, Poisson's ratios  $\nu_{13}(d)$  and  $\nu_{12}(d)$  are not affected by parameter  $d$ . There is only one stiffness tensor component  $C_4(d)$ , where  $C_4(d)/2$  represents the longitudinal shear modulus, decreases about with the increasing of  $d$ . Figure 4.5 exhibits the effect of damage parameter  $d$  on the normalized  $G_{23}(d)$ . When  $X < 1$ , the aspect ratio  $X$  has a more clear effect on the shear modulus  $G_{23}(d)$ .

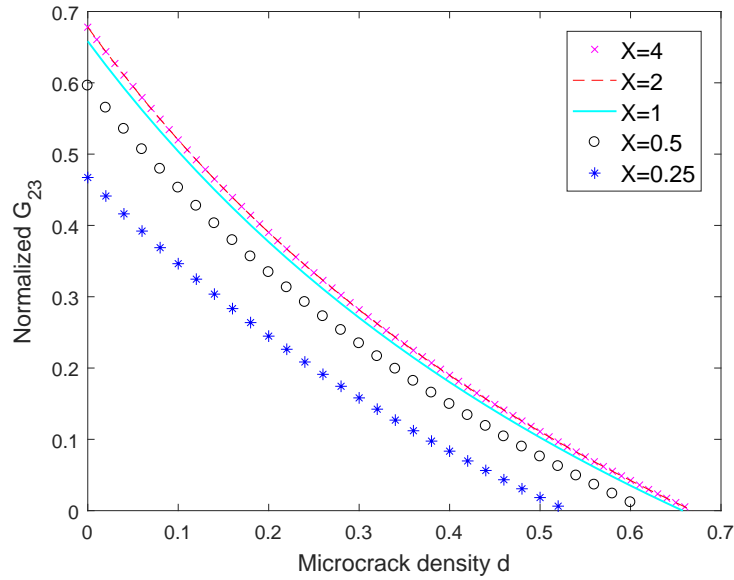


Figure 4.5: The relation between normalized  $G_{23}$  and  $d$  for closed microcracks by MT

### 4.3.3 The PCW estimate for open microcracks of isotropic distribution

In this part, we assume that all the microcracks are open. Our damage model is based on the scheme proposed by Ponte Castañeda-Willis [58]. Let us recall that this scheme is the extension of the Hashin-Shtrikman bound, and separates the shape of inclusion and the spatial distribution of inclusion by two independent functions. It is assumed that the spatial distributions of micropores and open microcracks are spherical. The damage is

characterized by a scalar microcrack density parameter  $d$ . We know  $\mathbb{C}_p = 0$  and  $\mathbb{C}_{op} = 0$ .

The fourth-order strain concentration tensors of micropores and microcracks by the PCW estimate are, respectively:

$$\begin{aligned} \mathbb{A}_p &= \left[ \mathbb{I} + \mathbb{P}_p^\epsilon : (\mathbb{C}_p - \mathbb{C}_s) \right]^{-1} \\ &: \left\{ f_s \mathbb{I} + \sum_{j=1}^2 f_j [\mathbb{I} + (\mathbb{P}_j^\epsilon - \mathbb{P}_j^d) : (\mathbb{C}_j - \mathbb{C}_s)] : [\mathbb{I} + \mathbb{P}_j^\epsilon : (\mathbb{C}_j - \mathbb{C}_s)]^{-1} \right\}^{-1} \end{aligned} \quad (4.14)$$

and

$$\begin{aligned} \mathbb{A}_{op} &= \left[ \mathbb{I} + \mathbb{P}_{op}^\epsilon : (\mathbb{C}_{op} - \mathbb{C}_s) \right]^{-1} \\ &: \left\{ f_s \mathbb{I} + \sum_{j=1}^2 f_j [\mathbb{I} + (\mathbb{P}_j^\epsilon - \mathbb{P}_j^d) : (\mathbb{C}_j - \mathbb{C}_s)] : [\mathbb{I} + \mathbb{P}_j^\epsilon : (\mathbb{C}_j - \mathbb{C}_s)]^{-1} \right\}^{-1} \end{aligned} \quad (4.15)$$

where the subscript  $\epsilon$  indicates the shape and  $d$  denotes the spatial distribution as explained in Chapter 2.  $\mathbb{P}_r^\epsilon$  is the shape tensor of the  $r$ -th phase.  $\mathbb{P}_r^\epsilon = \mathbb{S}_r^\epsilon : \mathbb{C}_s^{-1}$ , and  $\mathbb{S}_r^\epsilon$  is fourth-order Eshelby's tensor of the  $r$ -th phase, which has been given in B.  $\mathbb{P}_r^d$  represents the spatial distribution tensor of the  $r$ -th phase. For the tensorial functions of spatial distribution of micropores and microcracks, we consider that both of them are the spherical distribution. The tensorial function of the spatial distribution is [64]:

$$\mathbb{P}_p^d = \mathbb{P}_{op}^d = \frac{\alpha}{3k_s} \mathbb{J} + \frac{\beta}{2\mu_s} \mathbb{K} \quad (4.16)$$

where  $\alpha$  and  $\beta$  were shown in equation (2.33).

For simplification, (4.14) and (4.15) can be written as follows:

$$\mathbb{A}_p = \left[ \mathbb{I} + \mathbb{P}_p^\epsilon : (\mathbb{C}_p - \mathbb{C}_s) \right]^{-1} : \mathbb{M} \quad (4.17)$$

and

$$\mathbb{A}_{op} = \left[ \mathbb{I} + \mathbb{P}_{op}^\epsilon : (\mathbb{C}_{op} - \mathbb{C}_s) \right]^{-1} : \mathbb{M} \quad (4.18)$$

with

$$\begin{aligned} \mathbb{M} &= \left\{ f_s \mathbb{I} + f_p [\mathbb{I} + (\mathbb{P}_p^\epsilon - \mathbb{P}_p^d) : (\mathbb{C}_p - \mathbb{C}_s)] : [\mathbb{I} + \mathbb{P}_p^\epsilon : (\mathbb{C}_p - \mathbb{C}_s)]^{-1} \right. \\ &\quad \left. + f_{op} [\mathbb{I} + (\mathbb{P}_{op}^\epsilon - \mathbb{P}_{op}^d) : (\mathbb{C}_{op} - \mathbb{C}_s)] : [\mathbb{I} + \mathbb{P}_{op}^\epsilon : (\mathbb{C}_{op} - \mathbb{C}_s)]^{-1} \right\}^{-1} \end{aligned} \quad (4.19)$$

The strain concentration tensors for micropores and open microcracks can be represented as the following expressions, respectively:

$$\mathbb{A}_p = (\mathbb{I} - \mathbb{S}_p^\epsilon)^{-1} : \mathbb{M} \quad (4.20)$$

$$\mathbb{A}_{op} = (\mathbb{I} - \mathbb{S}_{op}^\epsilon)^{-1} : \mathbb{M} \quad (4.21)$$

where tensor  $\mathbb{M}$  can be simplified as:

$$\mathbb{M} = \left\{ \mathbb{I} + f_p(\alpha\mathbb{J} + \beta\mathbb{K}) : (\mathbb{I} - \mathbb{S}_p^\epsilon)^{-1} + \frac{4\pi}{3}d(\alpha\mathbb{J} + \beta\mathbb{K}) : \mathbb{T} \right\}^{-1} \quad (4.22)$$

with tensor  $\mathbb{T}$  was given in B.10.

The effective stiffness tensor of fired clay bricks with open microcracks can be recast as:

$$\mathbb{C}_{op}^{PCW}(d) = \mathbb{C}_s - f_p\mathbb{C}_s : (\mathbb{I} - \mathbb{S}_p^\epsilon)^{-1} : \mathbb{M} - \frac{4\pi d}{3}\mathbb{C}_s : \mathbb{T} : \mathbb{M} \quad (4.23)$$

The fourth-order effective stiffness tensor with open microcracks can be expressed by Walpole's notation [63]. Due to the parallel orientations of microcracks, only two material damage functions  $E_3(d)$  and  $G_{23}(d)$  are analyzed. Under given parameters  $\nu_s = 0.1$  and  $f_p = 20\%$ , the relationships between material constants and microcrack density  $d$  can be analyzed below for different aspect ratios of micropores  $X$ .

Figure 4.6 shows the relationship between normalized Young's modulus  $E_3(d)/E_s$  and damage parameter  $d$  for different aspect ratios. The microcrack density  $d$  can strongly weaken Young's modulus. Besides parameter  $d$ , the aspect ratio  $X$  of micropores also affects  $E_3(d)$ . the aspect ratio  $X$  is smaller,  $E_3(d)$  is lower, especially in the case of  $X < 1$ . When  $X > 1$ , the aspect ratio doesn't have a clear influence on  $E_3(d)$ .

Figure 4.7 shows the relationship between normalized shear modulus  $G_{23}(d)/\mu_s$  and damage parameter  $d$  for different aspect ratios. There is no obvious difference between  $X = 4$  and  $X = 2$ . It means that rising the aspect ratio of micropore barely affects  $G_{23}(d)$  of extruded bricks. But for  $G_{23}(d)$  of molded bricks, with the decreasing of aspect ratio,  $G_{23}(d)$  will decline.

#### 4.3.4 The PCW estimate for closed microcracks of isotropic distribution

In this case, it is assumed that the spatial distributions of closed micropores and microcracks are spherical. The lips between closed microcracks are assumed to be frictionless.

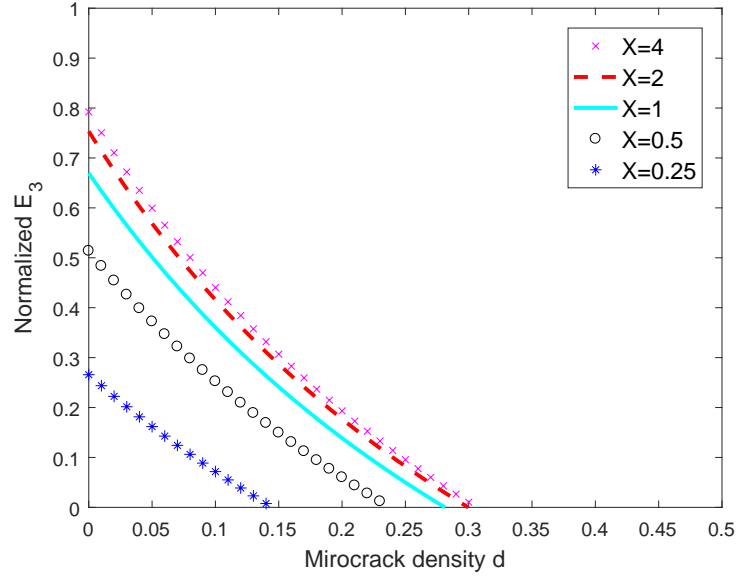


Figure 4.6: The relation between normalized  $E_3$  and  $d$  for closed microcracks by PCW

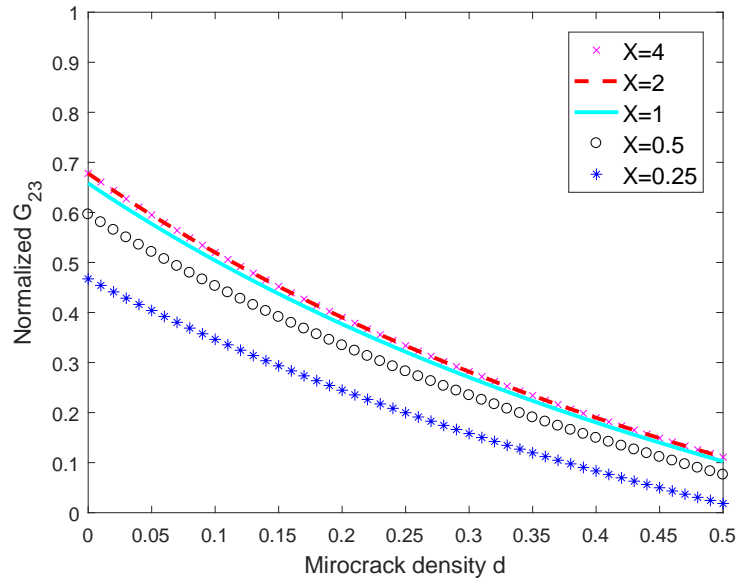


Figure 4.7: The relation between normalized  $G_{23}$  and  $d$  for closed microcracks by PCW

The strain concentration tensors for micropores and closed microcracks can be represented as the following expressions, respectively:

$$\mathbb{A}_p = (\mathbb{I} - \mathbb{S}_p^\epsilon)^{-1} : \mathbb{M} \quad (4.24)$$

and

$$\mathbb{A}_{cl} = (\mathbb{I} - \mathbb{S}_{cl}^\epsilon : \mathbb{K})^{-1} : \mathbb{M} \quad (4.25)$$

The fourth-order tensor  $\mathbb{M}$  is simplified as:

$$\mathbb{M} = \{\mathbb{I} + f_p(\alpha\mathbb{J} + \beta\mathbb{K}) : (\mathbb{I} - \mathbb{S}_p^\epsilon)^{-1} + \frac{4\pi}{3}d\beta\mathbb{K} : \mathbb{T}'\}^{-1} \quad (4.26)$$

where the Walpole notations of tensors  $\mathbb{J}$  and  $\mathbb{K}$  can be found in A. The tensor  $\mathbb{T}'$  has been given in B.11.

The fourth-order effective stiffness tensor for frictionless closed microcracks can be deduced as:

$$\mathbb{C}_{cl}^{PCW} = \mathbb{C}_s - f_p\mathbb{C}_s : (\mathbb{I} - \mathbb{S}_p^\epsilon)^{-1} : \mathbb{M} - \frac{8\pi d}{3}\mu_s\mathbb{K} : \mathbb{T}' : \mathbb{M} \quad (4.27)$$

According to [63], the fourth-order effective stiffness tensor for closed microcracks can be expressed by Walpole's notation. The detailed expressions of stiffness tensor components can be found in C.3.

Under the fixed parameters  $\nu_s = 0.1$  and  $f_p = 20\%$ , For aligned closed microcracks,  $C_4^{cl}(d)/2$  representing shear modulus  $G_{23}(d)$  decreases as the rising of microcrack density  $d$ , whereas other stiffness components keep invariant. In other words, longitudinal and transverse Young's moduli and Poisson's ratio are constants. Figure 4.8 is the tendency of shear modulus  $G_{23}(d)$  under different aspect ratios.

## 4.4 Thermodynamic potential and state laws

Damage of materials is the irreversible generation and propagation of micro-defects (microcracks and micropores) in material subjected to loading. The framework of continuum damage mechanics was firstly established by [73]. For an elastic-brittle material, we can introduce a damage internal parameter  $d$  to present the degradation of stiffness. The independent state variables are the strain tensor  $\underline{\underline{E}}$  and the damage parameter  $d$ .

The thermodynamic potential considering state variables is:

$$W(\underline{\underline{E}}, d) = \frac{1}{2}\underline{\underline{E}} : \mathbb{C}^{hom}(d) : \underline{\underline{E}} \quad (4.28)$$

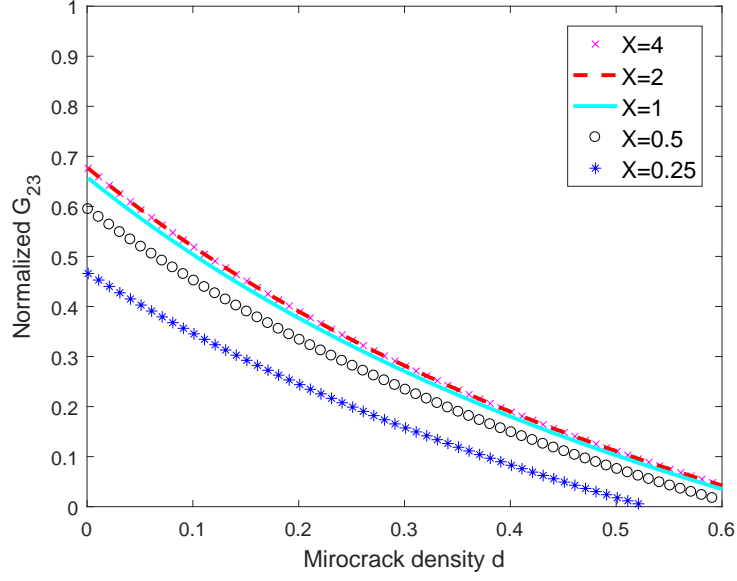


Figure 4.8: The relation between normalized  $G_{23}$  and  $d$  for closed microcracks by PCW

$d$  is a positive damage internal variable related with crack density.  $d = 0$  corresponds to the intact material.  $\mathbb{C}^{hom}(d)$  is the fourth-order effective stiffness tensor related with  $d$ .

The first state laws is:

$$\underline{\underline{\Sigma}}(\underline{\underline{E}}, d) = \frac{\partial W(\underline{\underline{E}}, d)}{\partial \underline{\underline{E}}} = \mathbb{C}^{hom}(d) : \underline{\underline{E}} \quad (4.29)$$

The second state law is:

$$F^d(\underline{\underline{E}}, d) = -\frac{\partial W(\underline{\underline{E}}, d)}{\partial d} = -\frac{1}{2} \underline{\underline{E}} : (\mathbb{C}^{hom}(d))' : \underline{\underline{E}} \quad (4.30)$$

$F^d$  is the damage driving force (also called energy release rate), and  $F^d > 0$ .  $(\mathbb{C}^{hom}(d))'$  is the derivative of the effective stiffness tensor considering crack density.

The evolution of damage doesn't take place for closed microcracks, but the damage evolution of open microcracks can be represented by the damage driving force  $F^d$ .

The classical damage criterion is expressed as:

$$f(F^d, d) = F^d - R(d) \leq 0 \quad (4.31)$$

$R(d)$  is a positive scalar as a function of  $d$ , which represents the ability to resist the damage propagation. Generally, the following linear resistance function introduced by [74] is

considered:

$$R(d) = R_0(1 + \eta d) \quad (4.32)$$

where  $R_0 > 0$  and  $\eta > 0$ .  $R_0$  is the initial threshold surface, and  $\eta$  is the material parameter.

The rate form of the constitutive law is:

$$\underline{\underline{\dot{\Sigma}}} = \mathbb{L}^{hom}(d) : \underline{\underline{\dot{E}}} \quad (4.33)$$

where the tangent tensor operator is:

$$\mathbb{L}^{hom}(d) = \left[ \mathbb{C}(d) - \frac{[\mathbb{C}'(d) : \underline{\underline{\varepsilon}}] \otimes [\mathbb{C}'(d) : \underline{\underline{\varepsilon}}]}{\frac{\partial F^d}{\partial d} + R_0 \cdot \eta} \right] \quad (4.34)$$

### The numerical implementation of the micromechanical damage modeling

The proposed damage model is implemented in the standard ABAQUS by means of UMAT subroutine. For the local integration of micromechanical modeling at each integration point (or Gauss point), a numerical algorithm is presented as follows:

- (1) It is assumed that the strain  $\underline{\underline{E}}_n$  at the step ( $n$ ) is given and the strain increment  $\Delta \underline{\underline{E}}_{n+1}$  is known. At the ( $n + 1$ ) step, the macroscopic strain  $\underline{\underline{E}}_{n+1} = \underline{\underline{E}}_n + \Delta \underline{\underline{E}}_{n+1}$ .
- (2) At the linearly elastic stage,  $d_{n+1} = d_n$  and  $f(F_{n+1}^d, d_n) \leq 0$ .
- (3) At the non-linear stage, if  $f(F_{n+1}^d, d_n) > 0$ ,  $\Delta d_{n+1}$  will be determined. Then it has  $d_{n+1} = d_n + \Delta d_{n+1}$ .
- (4) The macroscopic stress can be obtained:  $\underline{\underline{\Sigma}}(d_{n+1}) = \mathbb{C}^{hom}(d_{n+1}) : \underline{\underline{E}}_{n+1}$ .

## 4.5 The study on parameters of the damage model

Based on our damage modeling, the following parameters need to be determined: Young's modulus of solid matrix  $E_s$ , Poisson's ratio of solid matrix  $\nu_s$ , the volume fraction of micropores  $f_p$ , the aspect ratio of micropores  $X$ , the initial threshold surface  $R_0$  and the hardening parameter  $\eta$ .

	Solid matrix	Micropore
Material parameters	$E_s$ $\nu_s$	$f_p$ $X$
Damaged parameters	$R_0$ $\eta$	

Table 4.1: Parameters of the damage modeling

#### 4.5.1 The study on parameter $\eta$

The effect of  $\eta$  on mechanical behavior is studied under the fixed parameters in this part:  $E_s = 20000MPa$ ,  $\nu_s = 0.1$ ,  $f_p = 20\%$ ,  $X = 2$ ,  $R_0 = 0.2MPa$ .

Figure 4.9 exhibits the macroscopic full stress-strain curves under different values of  $\eta$ . The blue line is the linearly elastic stage. Other color curves represent the damage stages of fired clay bricks. From this figure, we can see that the greater the value  $\eta$  is, the stronger the strain hardening is. In other words, parameter  $\eta$  determines the peak strength of material. Figure 4.10 shows the variation tendency of the microcracks density with the increase of macroscopic strain on the 3-axis. Under given the strain of the damage stage, the greater the value of  $\eta$  is, the microcracks density is smaller. Though the values of  $\eta$  are different, the linear elastic stages are the same under the identical  $R_0$ . The value of  $\eta$  determines whether there is the strain-hardening stage in the damage process.

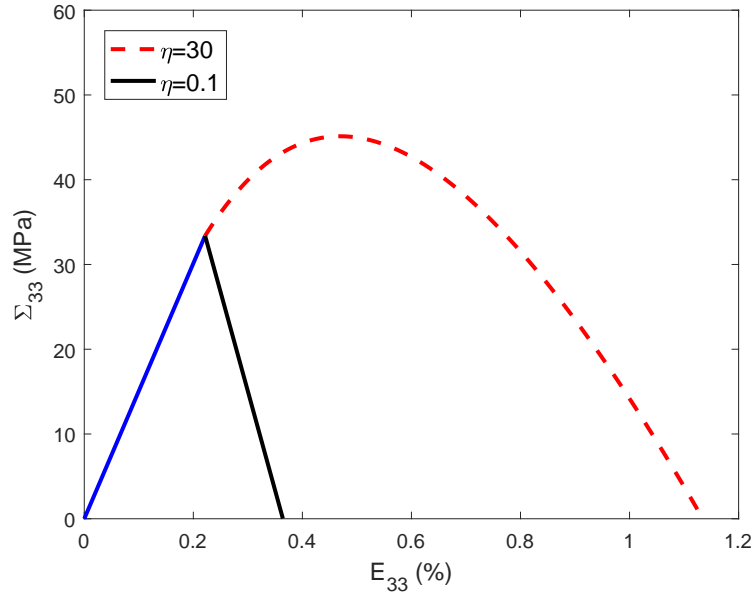


Figure 4.9: The stress-strain curves by PCW estimation under different values of  $\eta$

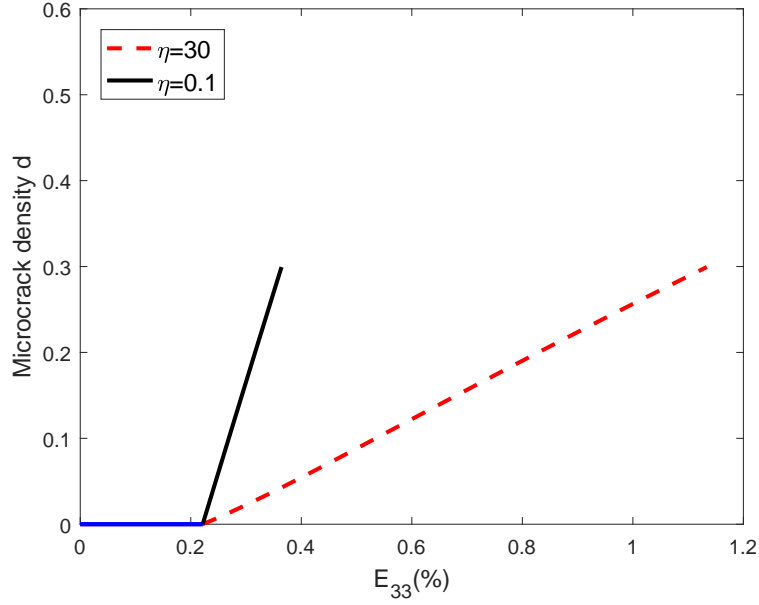


Figure 4.10: The relationships between damage parameter  $d$  and the axial strain  $E_{33}$

#### 4.5.2 The study on parameter $R_0$

As above mentioned, the parameter  $R_0$  determines the initial damage threshold. The influence of  $R_0$  on mechanical behavior is studied under the hypothetical parameters:  $E_s = 20000MPa$ ,  $\nu_s = 0.1$ ,  $f_p = 20\%$ ,  $X = 2$ ,  $\eta = 30$ .

Figure 4.11 shows the macroscopic stress-strain curves under the values of  $R_0 = 0.1MPa$  and  $R_0 = 0.2MPa$ . The greater the value of  $R_0$  is, the higher the elastic critical point is. In other words, the parameter  $R_0$  determines the elastic limitation of fired clay bricks. So the greater  $R_0$  also gives the higher strength.

Figure 4.12 shows the variation tendency of the microcracks density with the increase of macroscopic strain on the 3-axis. From the two figures, we can find that the smaller the value of  $R_0$  is, the damage initial strain is smaller.

#### 4.5.3 The study on parameter $f_p$

The influence of damage parameters  $\eta$  and  $R_0$  on mechanical behavior has been analyzed in the above two parts. The effect of porosity on mechanical behavior of fired clay bricks will be studied here. Given parameters  $E_s = 20000MPa$ ,  $\nu_s = 0.1$ ,  $R_0 = 0.1MPa$ ,  $\eta = 30$ ,

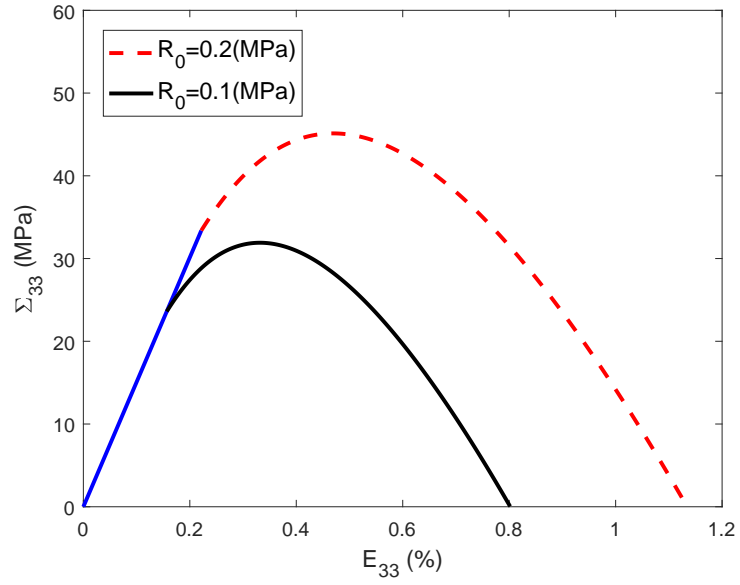


Figure 4.11: The stress-strain curves by PCW estimation under different values of  $R_0$

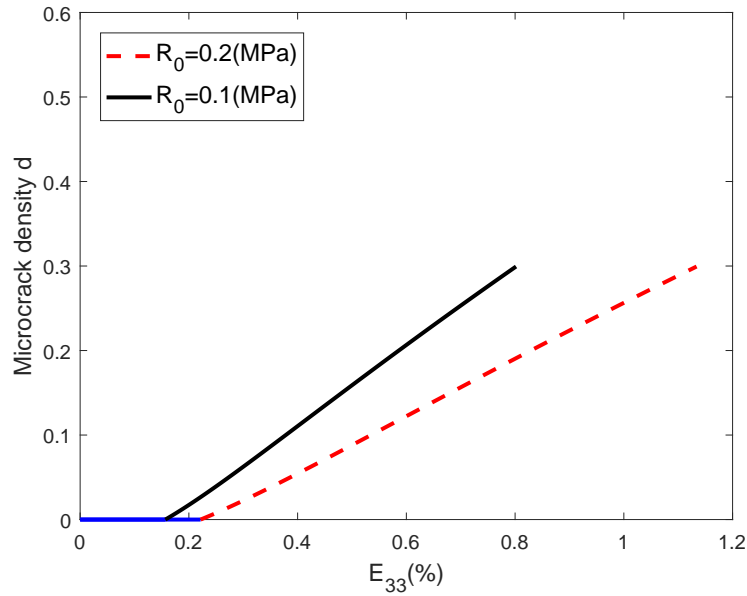


Figure 4.12: The relationships between  $d$  and the axial strain  $E_{33}$  under different  $R_0$

$X = 2$ , the stress-strain curves corresponding to 20% and 40% are obtained. It is obvious that porosity affects the elastic modulus and peak stress. When  $\eta$  is the same, the damage stages for different porosities are parallel.

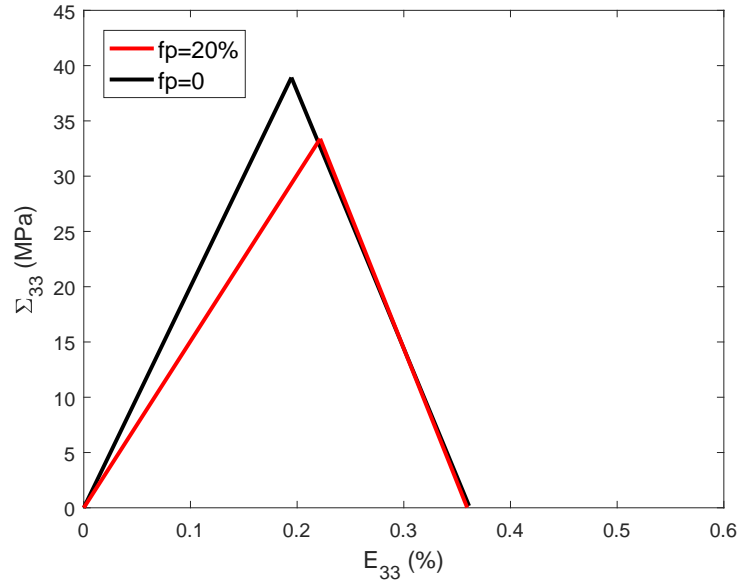


Figure 4.13: The stress-strain curve for different porosity when  $\eta = 0.1$

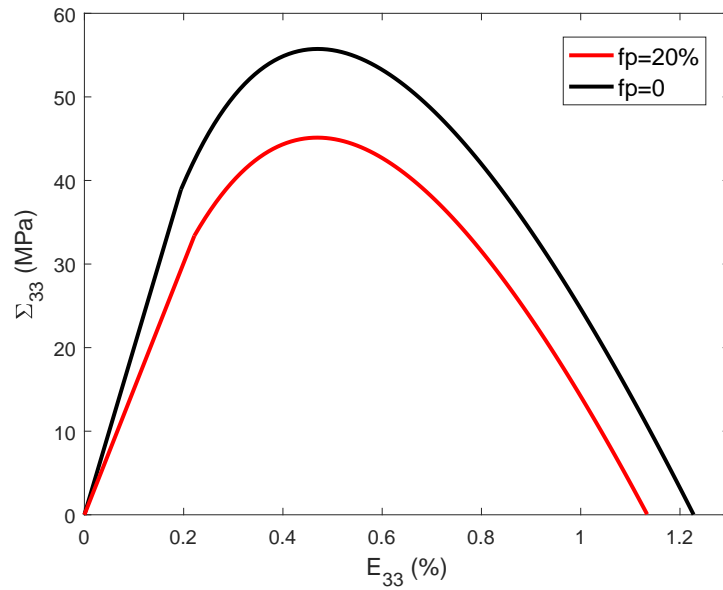


Figure 4.14: The stress-strain curve for different porosity when  $\eta = 30$

#### 4.5.4 The study on parameter $X$

In Chapter 2, the empirical models referring to peak strength was given. Figure 4.15 shows the relationship between normalized peak strength  $\Sigma_{33}/\sigma_s$  and porosity for different aspect ratios. For given parameters  $E_s = 20000MPa$ ,  $\nu_s = 0.1$ ,  $f_p = 20\%$ ,  $\eta = 30$ , it can be seen that both the porosity and the aspect ratio of micropores affect the peak strength of fired

clay bricks. Combining the predictions for the condition of  $X > 1$  and  $X < 1$ , the aspect ratios of micropores of molded bricks have a more impact on the peak strength.

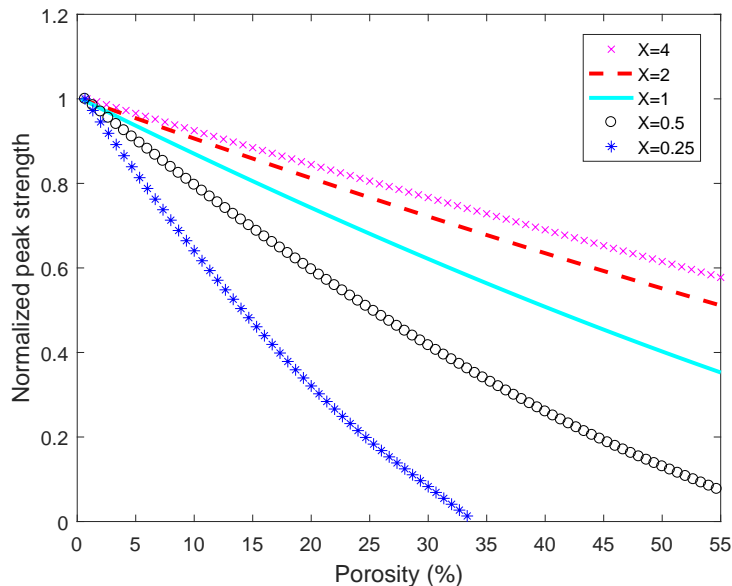


Figure 4.15: The relationship between peak strength and porosity by PCW

#### 4.5.5 The comparison between PCW scheme and MT scheme

The difference between PCW and MT schemes is that the former considers the spatial distribution of micropores. So the mechanical behavior of fired clay bricks by the two estimates are shown in the following figures.

Figure 4.16 exhibits the comparison of full stress-strain curves between Mori-Tanaka and PCW estimate under the hypothetical parameters of  $\eta = 30$  and  $f_p = 20\%$ . Other hypothetical material constants are:  $E_s = 20000MPa$ ,  $\nu_s = 0.1$ ,  $X = 2$ ,  $R_0 = 0.2MPa$ . Figure 4.17 shows the comparison of results by MT and PCW estimations under  $\eta = 0.1$  and  $f_p = 20\%$ . Compared with the two figures, the elastic moduli and strength by MT and PCW estimations are different, and there is no declined tendency for the results by MT estimation in the damage process even if  $\eta$  is very small. The difference between two estimations is that the MT approach ignores the spatial distribution of micropores and microcracks.

Compared with the results in Figure 4.17, the curves in Figure 4.18 are attained under  $\eta = 0.1$  and  $f_p = 0$ . In this case, the material is only composed of solid matrix when

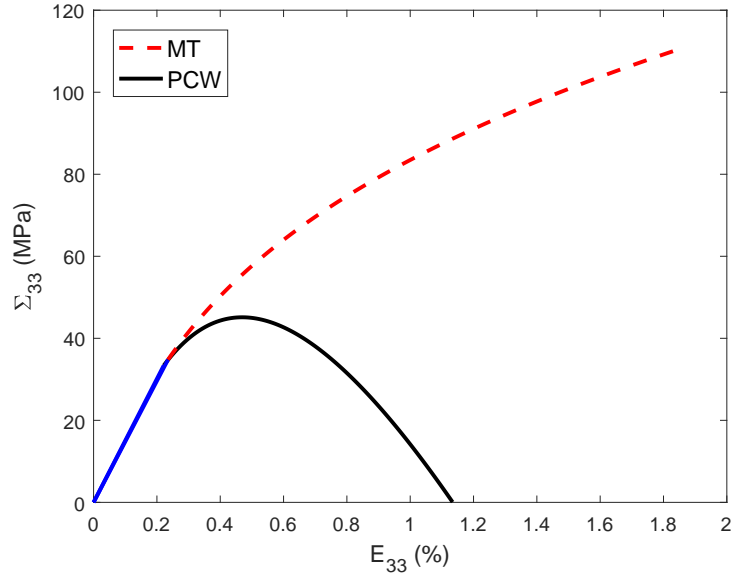


Figure 4.16: The stress-strain curves under  $\eta = 30$  and  $f_p = 20\%$

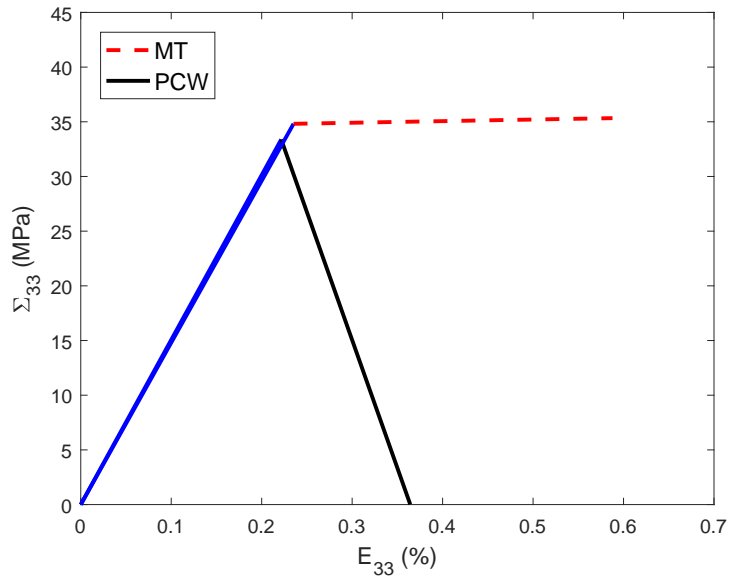


Figure 4.17: The stress-strain curves under  $\eta = 0.1$  and  $f_p = 20\%$

damage parameter  $d$  is equal to 0. The elastic parts from the two estimations are absolutely coincident. When the damage appears, the evolution of stress-strain is different due to the Mori-Tanaka approach ignores the spatial distribution of microcracks.

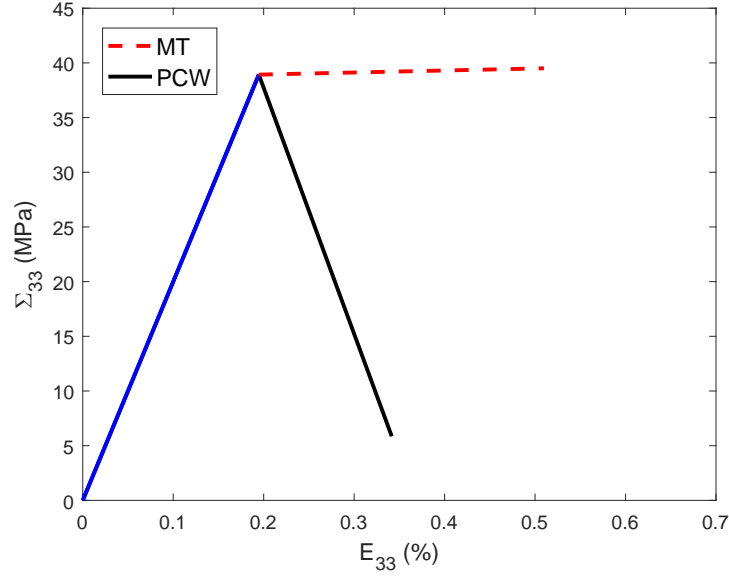


Figure 4.18: The stress-strain curves under  $\eta = 0.1$  and  $f_p = 0$

## 4.6 Calibrations and experimental validations of the micromechanical model

Calibrations and validations are performed in order to evaluate the predictive ability of our proposed modeling. Concerning our case, multi-variable calibration ( $\eta$  and  $R_0$ ) are realized by a software, named *modeFRONTIER*. A 'simplex' operation is selected for the minimization of a function of variables [75].

Table 4.2 gives the peak strength and Young's moduli in different directions. We calibrate the modeling parameters according to average values from experiments [6] on the 3-axis, and give our predicted results on the 1-axis. The calibrated parameters are:  $f_p = 24.0\%$ ,  $X = 1.6$ ,  $E_s = 15200MPa$ ,  $\nu_s = 0.1$ ,  $R_0 = 0.12MPa$ ,  $\eta = 0.1$ . Figure 4.19 displays the full stress-strain curves from our modeling and experimental data. In this figure, the experimental curve is only from one test, so the peak result is different from the data showed in Table 4.2.

Table 4.3 exhibits the peak strength and Young's moduli on different orientations. The experimental results were obtained from molded bricks [2], which caused oblate micropores. We calibrate the modeling parameters according to data on the 3-axis, and give our predicted results on the 1-axis. The relative error is also calculated in the Table 4.3. The calibrated parameters are:  $f_p = 27.0\%$ ,  $X = 0.35$ ,  $E_s = 21000MPa$ ,  $\nu_s = 0.07$ ,  $R_0 = 0.039MPa$ ,  $\eta = 150$ . Figure 4.20 exhibits the comparison between the experimental curve

	$\Sigma_{p3}$ (MPa)	$\Sigma_{p1}$ (MPa)	$\Sigma_{p3}/\Sigma_{p1}$	$E_3$ (MPa)	$E_1$ (MPa)	$E_3/E_1$
Experiment	56.8	51.0	1.11	12750	10450	1.22
Modeling	57.0	50.9	1.12	10457	8702	1.20

$\Sigma_{p3}$ : Peak stress on the 3-axis,  $\Sigma_{p1}$ : Peak stress on the 1-axis  
 $E_3$ : Young's modulus on the 3-axis,  $E_1$ : Young's modulus on the 1-axis

Table 4.2: Predictions for peak stress and Young's modulus on different directions

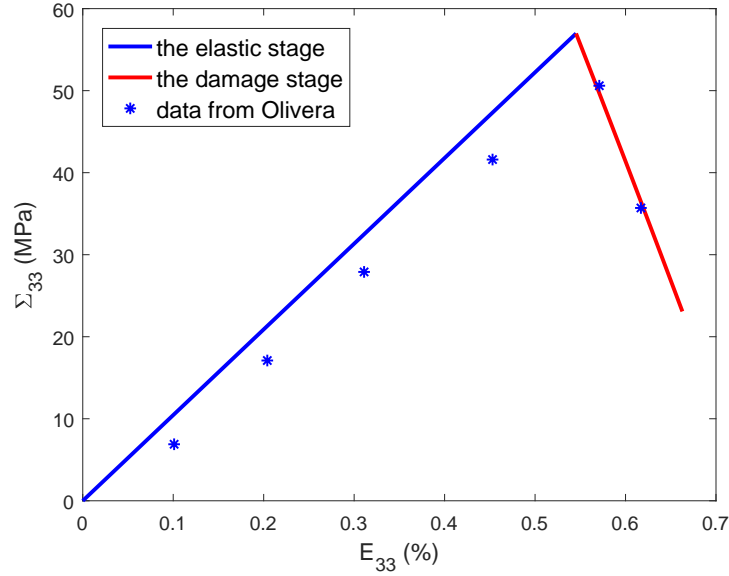


Figure 4.19: The comparison between our modeling and experimental results of extruded bricks [6]

and the prediction of modeling. It is clear that our modeling is in agreement with experimental results.

	$\Sigma_{p3}$ (MPa)	$\Sigma_{p1}$ (MPa)	$\Sigma_{p3}/\Sigma_{p1}$	$E_3$ (MPa)	$E_1$ (MPa)	$E_3/E_1$
Experiment	13.76	22.58	0.61	5524	16673	0.33
Modeling	13.74	400.27	0.034	5537	14065	0.39

Table 4.3: Predictions for peak stress and Young's modulus on different directions

Table 4.4 gives the comparison between experimental data [3] and modeling results under different porosities. Because paper residues are used to create micropores and to be part solid matrix in order to improve the thermal conductivity in this experiment, the physical properties of solid matrix are not same under different porosities. In our prediction, the effect of fired paper residues on the solid matrix is ignored. That is to

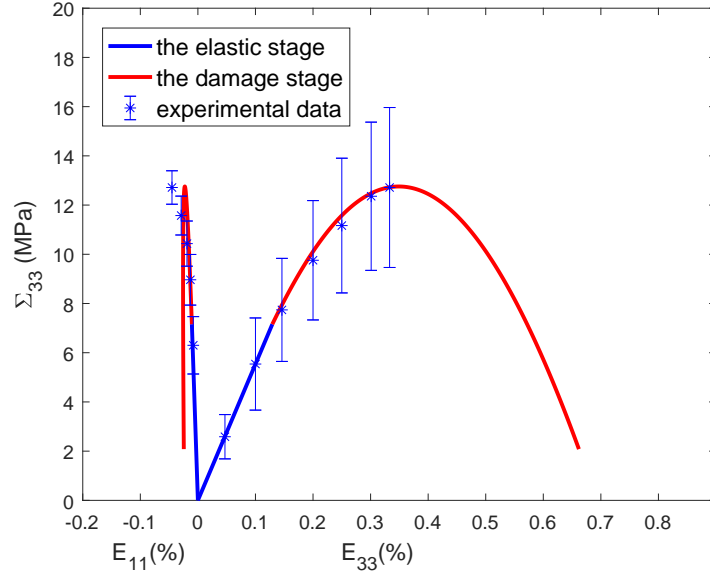


Figure 4.20: The comparison between our modeling and experimental results of molded bricks [2]

say, all solid matrix under contents of residues are regarded as the same. Under given values  $\nu_s = 0.1$ ,  $f_p = 30.8\%$ ,  $X = 0.51$  and the experimental result  $\Sigma_{p3} = 40MPa$ , we calibrate the following parameters:  $E_s = 25200MPa$ ,  $R_0 = 0.18MPa$ ,  $\eta = 98$ . Other peak stresses are predicted and listed in the table. From the results of modeling, our prediction is always greater than experimental results. Recalling that the solid matrix isn't same under different porosities, so our prediction for strength is reasonable.

Porosity		30.8%	38.9%	46.2%	52.0 %
Experiment	$\Sigma_{p3}(MPa)$	40.0	16.0	7.6	5.1
Modeling	$\Sigma_{p3}(MPa)$	<b>40.0</b>	24.11	14.45	8.05

Table 4.4: The comparison between experimental data and modeling results

## 4.7 Conclusions

In view of the context of application of fired clay bricks, we have built a micromechanical damage modeling by homogenization. It is assumed that the shape of microcracks is penny-shaped and the orientations of all microcracks are parallel. The unilateral effect of microcracks is taken to analyze the influence of damage parameter  $d$  on mechanical properties. Then we build a micro-mechanical damage modeling considering open microcracks.

After the analysis of mechanical behavior of our modeling, we can come to the following conclusions:

Firstly, the microcracks have strong influence on the degradation of fired clay bricks. With the increase of microcracks density (also the damage parameter  $d$ ), the elastic moduli of fired clay bricks decrease obviously. Similar to elastic moduli, porosity and the aspect ratio of micropores weaken the peak strength. The lower the aspect ratio, the smaller the peak strength.

Secondly, compared with Mori-Tanaka estimation, Ponte Castañeda-Willis estimation can predict the strain softening stage during the damage process by virtue of considering the spatial distribution of inclusions. The material parameter  $\eta$  determines the soften variation.

The numerical results of our proposed micromechanical damage modeling are approximately in agreement with the experimental data, which can predict accurately the mechanical behavior of fired clay bricks under the uniaxial compressive loading, including the damage stage.



# Conclusions and perspectives

## Conclusions

On the premise of satisfying mechanical capacity, fired clay bricks possessing the function of energy-saving have been the developing target with the demand of sustainable development. It is obvious that the macroscopic properties of fired clay bricks are dependent on their microscopic information. In order to provide a reference to change the information of micropores by using pore-forming agents, the effects of micropores and microcracks on macroscopic mechanical properties and thermal conductivity are studied by homogenization theory, which helps to understand the relationship between composition, micro-structure, material processing and mechanical or thermal properties. The study relies on the description of fired clay bricks at the micro-scale. It appears that the relation between micro-structure and macroscopic properties is important to predict engineering properties. The conclusions of this thesis are summarized as follows.

The Chapter 2 begins with the description of representative volume element as a micro-structural morphology composed of continuous solid matrix with micropores. It has been seen that the micro-structure is linked with the manufacturing technology of fired clay bricks. We proposed two different representative volume elements depending on extruding and molding technology, which generate the prolate or oblate micropores. Based on the analysis micro-structure, the effective elastic properties of fired clay bricks are studied by homogenization. We can obviously find that the volume fraction of pores is the most important factor which can weaken the elastic moduli. Besides porosity, we evaluate the effect of aspect ratio of micropores on elastic moduli. It can be found that the aspect ratio has a much stronger influence on Young's modulus parallel to the symmetric axis than that in other directions. It affects the shear modulus in the isotropic plane more clearly. With the increase of aspect ratios,  $E_3$  rises but  $G_{12}$  decreases. By using different approaches, the spatial distribution of micropores also affects the elastic moduli. The results considering the spherical distribution of pores exhibit more conspicuous anisotropic ratio than those of parallel distribution.

Based on the same microstructure, Chapter 3 is devoted to the study on effective thermal conductivity of fired clay bricks. Like the effective elastic properties, we study the influence of micropores on thermal conductivity. The effect of porosity on thermal conductivity is also the most apparent. In this chapter, we also predict the tendency of

thermal conductivity under the condition of high porosity. The prediction in this case still needs experimental data to validate. The aspect ratio of micropores affects the thermal conductivity  $\lambda_{33}$  on the symmetric axis more obviously. With the increasing of aspect ratio,  $\lambda_{33}$  significantly rises but  $\lambda_{11}$  decreases. The spherical spatial distribution of micropores shows much stronger anisotropy than those of aligned distribution. We can conclude that a method to improve the optimization between mechanical and thermal properties is not only changing the volume fraction of pores, but also adding different kind of pore-forming agents in the production process. An opening research direction is to study the effect of vegetable fibers on mechanical strength and thermal conduction.

As a kind of structural materials, fired clay bricks are mainly used to support the load. But it appears to be empirical to evaluate the mechanical strength. In Chapter 4, we build a micro-mechanical damage modeling to link peak strength and micropores, including the volume fraction and aspect ratio of pores. The impact of porosity on peak strength is studied under different aspect ratios. It can be seen that the effect of porosity on peak strength is very strong. Moreover, the aspect ratio of micropores also obviously affects the peak strength. The aspect ratio is greater, the strength on the major axis is higher. By comparison of results by MT and PCW approaches, the PCW estimation considering the spatial distribution of micropores and microcracks can predict the strain-softening behavior of fired clay bricks, but MT estimate can't achieve. The material parameter  $\eta$  determines the tendency of strain-softening. The parameter  $R_0$  is the initial elastic threshold of material. The validations between our proposed damage modeling and experimental data approximately exhibit an agreement.

## Perspectives

Some work of this thesis can be improved and a lot of research perspectives can be found in the future work.

The optimization between mechanical properties and thermal conductivity can be achieved by combining engineering situations. For example, due to the transverse isotropy of fired clay bricks, the orientation of bricks laying in the wall can cause different mechanical strength and thermal conductivity of walls. Due to hollow fired clay bricks are also used in masonry structures, the influence of different geometries of hollow bricks on mechanical properties of masonries can be the following research work.

We take the same microscopic scales for micropores and microcracks in the RVE. To study the micro-mechanical modeling more precisely, it is necessary to analyze the distribution of size of micropores and microcracks, which is helpful to build a multi-scale RVE.

In the Chapter 4, our proposed damage modeling is based on the assumption of aligned opening microcracks of spherical distribution. The following work can focus on the condition of random orientation of microcracks, including opening or closed ones. In this thesis, we only consider the porous and cracked solid matrix without liquid as the research objective in the thesis. The influence of transfer of substances in opening microcracks on the properties of fired clay bricks will be a new direction in the following work. The multi-scale micromechanical modeling considering multi-phenomena couplings can help us understand mechanical behavior under complex environmental conditions.

The study on fired clay tiles with additives is an interesting research subject. The difference with bricks is that the orientations and the spatial distributions of micropores in tiles due to the molding technology. Considering that tiles are always suffered the changing of the seasons, the impact of numbers and temperatures of freeze-thaw cycles on durability of fired clay bricks is also attractive.



# Walpole's notation

---

The transverse isotropy is that the elastic properties of arbitrary directions which are normal to a symmetric axis are the same. The fourth-order stiffness tensor only has 5 independent constants. In order to study the transversely isotropic problems, it is necessary to introduce the notation from [63] which is helpful to obtain the elements of transversely isotropic tensors. Given a unit normal vector  $\underline{n}$ , other directions perpendicular to  $\underline{n}$  are equivalent because of transversely isotropic symmetry. Also given the second-order unit tensor  $\mathbf{1}$  (Kronecker tensor  $\delta_{ij}$ ), the unit tensor is decomposed of two elementary tensors  $\mathbf{a}$  and  $\mathbf{b}$ :

$$\mathbf{1} = \mathbf{a} + \mathbf{b} \quad (\text{A.1})$$

with

$$\mathbf{a} = \mathbf{1} - \underline{n} \otimes \underline{n}, \quad \mathbf{b} = \underline{n} \otimes \underline{n} \quad (\text{A.2})$$

The set of fourth order elementary tensors contain 4 unit tensors with diagonal symmetry and 2 tensors without diagonal symmetry. The diagonally symmetric tensors are:

$$\mathbb{E}_1 = \frac{1}{2} \mathbf{a} \otimes \mathbf{a}, \quad \mathbb{E}_2 = \mathbf{b} \otimes \mathbf{b}, \quad \mathbb{E}_3 = \mathbf{a} \overline{\otimes} \mathbf{a} - \frac{1}{2} \mathbf{a} \otimes \mathbf{a}, \quad \mathbb{E}_4 = \mathbf{a} \overline{\otimes} \mathbf{b} + \mathbf{b} \overline{\otimes} \mathbf{a} \quad (\text{A.3})$$

It is easily seen that:

$$\mathbb{E}_1 + \mathbb{E}_2 + \mathbb{E}_3 + \mathbb{E}_4 = \mathbb{I} \quad (\text{A.4})$$

Especially, when  $p$  and  $q$  are integers from 1 to 4, we can also obtain the following expressions:

$$\mathbb{E}_4 : \mathbb{J} = \mathbb{J} : \mathbb{E}_4 = 0, \quad \mathbb{E}_4 : \mathbb{K} = \mathbb{K} : \mathbb{E}_4 = \mathbb{E}_4 \quad (\text{A.5})$$

and

$$\mathbb{E}_p : \mathbb{E}_q = \mathbb{E}_q, \quad \text{if } p = q; \quad \mathbb{E}_p : \mathbb{E}_q = 0, \quad \text{if } p \neq q \quad (\text{A.6})$$

The non-diagonally symmetric tensors are:

$$\mathbb{E}_5 = \mathbf{b} \otimes \mathbf{a}, \quad \mathbb{E}_6 = \mathbf{a} \otimes \mathbf{b} \quad (\text{A.7})$$

The tensor products of elements can be presented as the table:

	$\mathbb{E}_1$	$\mathbb{E}_2$	$\mathbb{E}_3$	$\mathbb{E}_4$	$\mathbb{E}_5$	$\mathbb{E}_6$
$\mathbb{E}_1$	$\mathbb{E}_1$	0	0	0	0	$\mathbb{E}_6$
$\mathbb{E}_2$	0	$\mathbb{E}_2$	0	0	$\mathbb{E}_5$	0
$\mathbb{E}_3$	0	0	$\mathbb{E}_3$	0	0	0
$\mathbb{E}_4$	0	0	0	$\mathbb{E}_4$	0	0
$\mathbb{E}_5$	$\mathbb{E}_5$	0	0	0	0	$2\mathbb{E}_2$
$\mathbb{E}_6$	0	$\mathbb{E}_6$	0	0	$2\mathbb{E}_1$	0

Table A.1: The products of Walpole tensor elements

Based on Walpole notation, any transversely isotropic fourth-order tensor, which is not necessarily symmetric, can be expressed by six elementary tensors.

$$\mathbb{U} = c\mathbb{E}_1 + d\mathbb{E}_2 + e\mathbb{E}_3 + f\mathbb{E}_4 + g\mathbb{E}_5 + h\mathbb{E}_6 \quad (\text{A.8})$$

which can be recast as another form:

$$\mathbb{U} = [c, d, e, f, g, h] \quad (\text{A.9})$$

If the tensor  $\mathbb{U}$  is symmetric, it has  $g = h$ .

The inverse of  $\mathbb{U}$  is:

$$\mathbb{U}^{-1} = \left[ \frac{d}{l}, \frac{c}{l}, \frac{1}{e}, \frac{1}{f}, -\frac{g}{l}, -\frac{h}{l} \right] \quad (\text{A.10})$$

with  $l = cd - 2gh$ .

The fourth-order unit tensor  $\mathbb{I}$  of equation (A.4) can be represented as:

$$\mathbb{I} = [1, 1, 1, 1, 0, 0] \quad (\text{A.11})$$

The spherical tensor  $\mathbb{J}$  and deviatoric tensor  $\mathbb{K}$  of equation (A.5) can be represented as:

$$\mathbb{J} = \left[\frac{2}{3}, \frac{1}{3}, 0, 0, \frac{1}{3}, \frac{1}{3}\right], \quad \mathbb{K} = \left[\frac{1}{3}, \frac{2}{3}, 1, 1, -\frac{1}{3}, -\frac{1}{3}\right] \quad (\text{A.12})$$

Walpole defined the unit tensor as  $\mathbb{I} = \mathbb{J} + \mathbb{K}$ . These fourth-order tensors can be written as:

$$\begin{aligned} \mathbb{I}_{ijkl} &= \frac{1}{2}(\delta_{ik}\delta_{jl} + \delta_{il}\delta_{jk}), & \mathbb{J}_{ijkl} &= \frac{1}{3}\delta_{ij}\delta_{kl} \\ \mathbb{K}_{ijkl} &= \frac{1}{2}(\delta_{ik}\delta_{jl} + \delta_{il}\delta_{jk} - \frac{2}{3}\delta_{ij}\delta_{kl}) \end{aligned} \quad (\text{A.13})$$

The decomposed tensors are idempotent and orthogonal:

$$\mathbb{J} : \mathbb{J} = \mathbb{J}, \quad \mathbb{K} : \mathbb{K} = \mathbb{K}, \quad \mathbb{J} : \mathbb{K} = 0 \quad (\text{A.14})$$

For isotropic solid matrix, the stiffness tensor can be expressed by decomposed tensors  $\mathbb{J}$  and  $\mathbb{K}$ .

$$\mathbb{C}_s = 3k_s\mathbb{J} + 2\mu_s\mathbb{K} \quad (\text{A.15})$$

where  $k_s$  is the bulk modulus of solid matrix and  $\mu_s$  is the shear modulus of solid matrix.

In Voigt notation, these fourth-order tensors can be recast as:

$$\mathbb{I} = \begin{pmatrix} 1 & 0 & 0 & 0 & 0 & 0 \\ 0 & 1 & 0 & 0 & 0 & 0 \\ 0 & 0 & 1 & 0 & 0 & 0 \\ 0 & 0 & 0 & 1 & 0 & 0 \\ 0 & 0 & 0 & 0 & 1 & 0 \\ 0 & 0 & 0 & 0 & 0 & 1 \end{pmatrix} \quad \mathbb{J} = \begin{pmatrix} \frac{1}{3} & \frac{1}{3} & \frac{1}{3} & 0 & 0 & 0 \\ \frac{1}{3} & \frac{1}{3} & \frac{1}{3} & 0 & 0 & 0 \\ \frac{1}{3} & \frac{1}{3} & \frac{1}{3} & 0 & 0 & 0 \\ 0 & 0 & 0 & 0 & 0 & 0 \\ 0 & 0 & 0 & 0 & 0 & 0 \\ 0 & 0 & 0 & 0 & 0 & 0 \end{pmatrix} \quad \mathbb{K} = \begin{pmatrix} \frac{2}{3} & -\frac{1}{3} & -\frac{1}{3} & 0 & 0 & 0 \\ -\frac{1}{3} & \frac{2}{3} & -\frac{1}{3} & 0 & 0 & 0 \\ -\frac{1}{3} & -\frac{1}{3} & \frac{2}{3} & 0 & 0 & 0 \\ 0 & 0 & 0 & 1 & 0 & 0 \\ 0 & 0 & 0 & 0 & 1 & 0 \\ 0 & 0 & 0 & 0 & 0 & 1 \end{pmatrix}$$

The base tensor of Walpole can be expressed by Voigt notation when  $\underline{\mathbf{n}}=(0,0,1)$ , as follows:

$$\mathbb{E}_1 = \begin{pmatrix} \frac{1}{2} & \frac{1}{2} & 0 & 0 & 0 & 0 \\ \frac{1}{2} & \frac{1}{2} & 0 & 0 & 0 & 0 \\ 0 & 0 & 0 & 0 & 0 & 0 \\ 0 & 0 & 0 & 0 & 0 & 0 \\ 0 & 0 & 0 & 0 & 0 & 0 \\ 0 & 0 & 0 & 0 & 0 & 0 \end{pmatrix}$$

$$\mathbb{E}_2 = \begin{pmatrix} 0 & 0 & 0 & 0 & 0 & 0 \\ 0 & 0 & 0 & 0 & 0 & 0 \\ 0 & 0 & 1 & 0 & 0 & 0 \\ 0 & 0 & 0 & 0 & 0 & 0 \\ 0 & 0 & 0 & 0 & 0 & 0 \\ 0 & 0 & 0 & 0 & 0 & 0 \end{pmatrix}$$

$$\mathbb{E}_3 = \begin{pmatrix} \frac{1}{2} & -\frac{1}{2} & 0 & 0 & 0 & 0 \\ -\frac{1}{2} & \frac{1}{2} & 0 & 0 & 0 & 0 \\ 0 & 0 & 0 & 0 & 0 & 0 \\ 0 & 0 & 0 & 0 & 0 & 0 \\ 0 & 0 & 0 & 0 & 0 & 0 \\ 0 & 0 & 0 & 0 & 0 & 1 \end{pmatrix}$$

$$\mathbb{E}_4 = \begin{pmatrix} 0 & 0 & 0 & 0 & 0 & 0 \\ 0 & 0 & 0 & 0 & 0 & 0 \\ 0 & 0 & 0 & 0 & 0 & 0 \\ 0 & 0 & 0 & 1 & 0 & 0 \\ 0 & 0 & 0 & 0 & 1 & 0 \\ 0 & 0 & 0 & 0 & 0 & 0 \end{pmatrix}$$

$$\mathbb{E}_5 = \begin{pmatrix} 0 & 0 & 0 & 0 & 0 & 0 \\ 0 & 0 & 0 & 0 & 0 & 0 \\ 1 & 1 & 0 & 0 & 0 & 0 \\ 0 & 0 & 0 & 0 & 0 & 0 \\ 0 & 0 & 0 & 0 & 0 & 0 \\ 0 & 0 & 0 & 0 & 0 & 0 \end{pmatrix}$$

$$\mathbb{E}_6 = \begin{pmatrix} 0 & 0 & 1 & 0 & 0 & 0 \\ 0 & 0 & 1 & 0 & 0 & 0 \\ 0 & 0 & 0 & 0 & 0 & 0 \\ 0 & 0 & 0 & 0 & 0 & 0 \\ 0 & 0 & 0 & 0 & 0 & 0 \\ 0 & 0 & 0 & 0 & 0 & 0 \end{pmatrix}$$

# Eshelby tensor in linear elasticity

---

$\mathbb{S}_r^\epsilon$  is called as Eshelby tensor of the  $r$ -th phase. The fourth-order Eshelby tensor of can be represented by six elemental tensors as the following form [63, 46]:

$$\mathbb{S}_r^\epsilon = a_1\mathbb{E}_1 + a_2\mathbb{E}_2 + a_3\mathbb{E}_3 + a_4\mathbb{E}_4 + a_5\mathbb{E}_5 + a_6\mathbb{E}_6 \quad (\text{B.1})$$

or

$$\mathbb{S}_r^\epsilon = [a_1, a_2, a_3, a_4, a_5, a_6] \quad (\text{B.2})$$

where,  $a_i (i = 1 \text{ } 6)$  are the following six scalars:

$$\begin{aligned} a_1 &= S_{1111} + S_{1122}, & a_2 &= S_{3333}, & a_3 &= S_{1111} - S_{1122}, \\ a_4 &= 2S_{3131}, & a_5 &= S_{3311}, & a_6 &= S_{1133} \end{aligned} \quad (\text{B.3})$$

For the inclusion in isotropic matrix, the Eshelby tensor depends on the shape of inclusion and the stiffness of matrix. When the symmetric axis of inclusion is  $\underline{n} = (0, 0, 1)$ , the shape of ellipsoidal inclusion can be expressed by three-dimensional Cartesian coordinate system.

$$\frac{z_1^2}{m_1^2} + \frac{z_2^2}{m_2^2} + \frac{z_3^2}{m_3^2} = 1, \quad \text{with } m_1 = m_2 \quad (\text{B.4})$$

[55] has given the components of Eshelby tensor of ellipsoidal inclusion.

$$\begin{aligned} S_{iiii} &= \frac{3}{8\pi(1-\nu)} m_i^2 I_{ii} + \frac{1-2\nu}{8\pi(1-\nu)} I_i \\ S_{ijij} &= \frac{1}{8\pi(1-\nu)} m_j^2 I_{ij} - \frac{1-2\nu}{8\pi(1-\nu)} I_i \\ S_{ijij} &= \frac{1}{16\pi(1-\nu)} (m_i^2 + m_j^2) I_{ij} + \frac{1-2\nu}{16\pi(1-\nu)} (I_i + I_j) \end{aligned} \quad (\text{B.5})$$

where  $\nu$  is Poisson's ratio of matrix.  $I_{ij}$  and  $I_i$  can be expressed as the following integrals by [76] and [55].

$$\begin{aligned}
I_i &= 2\pi m_1 m_2 m_3 \int_0^\infty \frac{du}{(m_i^2 + u)\Delta} \\
I_{ii} &= 2\pi m_1 m_2 m_3 \int_0^\infty \frac{du}{(m_i^2 + u)^2 \Delta} \\
I_{ij} &= 2\pi m_1 m_2 m_3 \int_0^\infty \frac{du}{(m_i^2 + u)(m_j^2 + u)\Delta}
\end{aligned} \tag{B.6}$$

with

$$\Delta = (m_1^2 + u)^{\frac{1}{2}}(m_2^2 + u)^{\frac{1}{2}}(m_3^2 + u)^{\frac{1}{2}} \tag{B.7}$$

For the prolate spheroidal inclusion ( $m_1 = m_2 < m_3$ ), the integral result is:

$$\begin{aligned}
I_1 = I_2 &= \frac{2\pi m_1^2 m_3}{(m_3^2 - m_1^2)^{\frac{3}{2}}} \left[ \frac{m_3}{m_1} \left( \frac{m_3^2}{m_1^2} - 1 \right)^{\frac{1}{2}} - \cosh^{-1} \frac{m_3}{m_1} \right] \\
I_3 &= 4\pi - 2I_1, \quad I_{11} = I_{22} = I_{12} \\
I_{12} &= \frac{\pi}{m_1^2} - \frac{1}{4} I_{13} = \frac{\pi}{m_1^2} - \frac{(I_1 - I_3)}{4(m_3^2 - m_1^2)} \\
I_{31} &= \frac{I_1 - I_3}{m_3^2 - m_1^2} \\
3I_{33} &= \frac{4\pi}{m_3^2} - 2I_{31} \\
3I_{11} &= \frac{4\pi}{m_1^2} - I_{12} - \frac{I_1 - I_3}{m_3^2 - m_1^2}
\end{aligned} \tag{B.8}$$

For the oblate spheroidal inclusion ( $m_1 = m_2 > m_3$ ), the integral result is:

$$\begin{aligned}
I_1 = I_2 &= \frac{2\pi m_1^2 m_3}{(m_1^2 - m_3^2)^{\frac{3}{2}}} \left[ \cos^{-1} \frac{m_3}{m_1} - \frac{m_3}{m_1} \left( 1 - \frac{m_3^2}{m_1^2} \right)^{\frac{1}{2}} \right] \\
I_3 &= 4\pi - 2I_1, \quad I_{11} = I_{22} = I_{12} \\
I_{12} &= \frac{\pi}{m_1^2} - \frac{1}{4} I_{13} = \frac{\pi}{m_1^2} - \frac{(I_1 - I_3)}{4(m_3^2 - m_1^2)} \\
I_{31} &= \frac{I_1 - I_3}{m_3^2 - m_1^2} \\
3I_{33} &= \frac{4\pi}{m_3^2} - 2I_{31} \\
3I_{11} &= \frac{4\pi}{m_1^2} - I_{12} - \frac{I_1 - I_3}{m_3^2 - m_1^2}
\end{aligned} \tag{B.9}$$

The tensor  $\mathbb{T}$  of penny-shaped ( $X_c \ll 1$ ) open microcracks is [77]:

$$\mathbb{T} = \lim_{X_c \rightarrow 0} X_c (\mathbb{I} - \mathbb{S}_c^\epsilon)^{-1} = \frac{4}{\pi} \left[ 0, \frac{(1 - \nu_s)^2}{1 - 2\nu_s}, 0, \frac{1 - \nu_s}{2 - \nu_s}, \frac{\nu_s(1 - \nu_s)}{1 - 2\nu_s}, 0 \right] \tag{B.10}$$

The tensor  $\mathbb{T}'$  of penny-shaped closed microcracks is [77]:

$$\mathbb{T}' = \lim_{X_c \rightarrow 0} X_c (\mathbb{I} - \mathbb{S}_c^\epsilon : \mathbb{K})^{-1} = \frac{4}{\pi} \left[ 0, 0, 0, \frac{1 - \nu_s}{2 - \nu_s}, 0, 0 \right] \tag{B.11}$$



# The calculations of transversely isotropic stiffness tensor

---

## Contents

C.1	The calculation of elastic stiffness tensor of Mori-Tanaka estimate	113
C.2	The calculation of elastic stiffness tensor of Ponte Castañeda-Willis estimate . . . . .	116
C.3	The calculation of stiffness tensor of Ponte Castañeda-Willis estimate considering damage . . . . .	118

---

## C.1 The calculation of elastic stiffness tensor of Mori-Tanaka estimate

In this section, the elastic stiffness tensor by Mori-Tanaka estimate is derived and the calculated result is expressed by Walpole notation.

According to equations (A.11), (B.2) and (A.10), it is readily to have:

$$(\mathbb{I} - \mathbb{S}_r^\epsilon)^{-1} = [b_1, b_2, b_3, b_4, b_5, b_6] \quad (\text{C.1})$$

with

$$\begin{aligned}
b_1 &= \frac{1 - a_2}{(1 - a_1)(1 - a_2) - 2a_5a_6} \\
b_2 &= \frac{1 - a_1}{(1 - a_1)(1 - a_2) - 2a_5a_6} \\
b_3 &= \frac{1}{1 - a_3} \\
b_4 &= \frac{1}{1 - a_4} \\
b_5 &= \frac{a_5}{(1 - a_1)(1 - a_2) - 2a_5a_6} \\
b_6 &= \frac{a_6}{(1 - a_1)(1 - a_2) - 2a_5a_6}
\end{aligned} \tag{C.2}$$

where  $a_1, a_2, \dots, a_6$  were given in (B.3).

Replacing  $\mathbb{P}_p^\epsilon$  by  $\mathbb{S}_p^\epsilon : \mathbb{C}_s^{-1}$ , it is easy to calculate the following equation:

$$f_s \mathbb{I} + f_p [\mathbb{I} + \mathbb{P}_p^\epsilon : (\mathbb{C}_p - \mathbb{C}_s)]^{-1} = [n_1, n_2, n_3, n_4, n_5, n_6] \tag{C.3}$$

with

$$\begin{aligned}
n_1 &= I_1 + f_p(b_1 - I_1) \\
n_2 &= I_2 + f_p(b_2 - I_2) \\
n_3 &= I_3 + f_p(b_3 - I_3) \\
n_4 &= I_4 + f_p(b_4 - I_4) \\
n_5 &= I_5 + f_p(b_5 - I_5) \\
n_6 &= I_6 + f_p(b_6 - I_6)
\end{aligned} \tag{C.4}$$

The inverse of equation (C.3) is:

$$\{f_s \mathbb{I} + f_p [\mathbb{I} + \mathbb{P}_p^\epsilon : (\mathbb{C}_p - \mathbb{C}_s)]^{-1}\}^{-1} = [g_1, g_2, g_3, g_4, g_5, g_6] \tag{C.5}$$

with

$$\begin{aligned}
g_1 &= n_2 / (n_1 \cdot n_2 - 2n_5 \cdot n_6) \\
g_2 &= n_1 / (n_1 \cdot n_2 - 2n_5 \cdot n_6) \\
g_3 &= 1/n_3 \\
g_4 &= 1/n_4 \\
g_5 &= -n_5 / (n_1 \cdot n_2 - 2n_5 \cdot n_6) \\
g_6 &= -n_6 / (n_1 \cdot n_2 - 2n_5 \cdot n_6)
\end{aligned} \tag{C.6}$$

From the expression (2.17), the strain localization tensor of micropores could be written as:

$$\mathbb{A}_p^{MT} = \left( \mathbb{I} - \mathbb{S}_p^c \right)^{-1} : \left\{ f_s \mathbb{I} + f_p [\mathbb{I} + \mathbb{P}_p^c : (\mathbb{C}_p - \mathbb{C}_s)]^{-1} \right\}^{-1} \quad (\text{C.7})$$

By calculation,  $\mathbb{A}_p^{MT}$  is described by Walpole's notation:

$$\mathbb{A}_p^{MT} = [A_{p1}, A_{p2}, A_{p3}, A_{p4}, A_{p5}, A_{p6}] \quad (\text{C.8})$$

with

$$\begin{aligned} A_{p1} &= b_1 g_1 + 2b_6 g_5 \\ A_{p2} &= b_2 g_2 + 2b_5 g_6 \\ A_{p3} &= b_3 g_3 \\ A_{p4} &= b_4 g_4 \\ A_{p5} &= b_5 g_1 + b_2 g_5 \\ A_{p6} &= b_6 g_2 + b_1 g_6 \end{aligned} \quad (\text{C.9})$$

The fourth-order stiffness tensor of isotropic solid matrix can be written as:

$$\mathbb{C}_s = [C_{s1}, C_{s2}, C_{s3}, C_{s4}, C_{s5}, C_{s6}] \quad (\text{C.10})$$

with

$$\begin{aligned} C_{s1} &= 2k_s + \frac{2}{3}\mu_s, & C_{s2} &= k_s + \frac{4}{3}\mu_s, & C_{s3} &= 2\mu_s \\ C_{s4} &= 2\mu_s, & C_{s5} &= k_s - \frac{2}{3}\mu_s, & C_{s6} &= k_s - \frac{2}{3}\mu_s \end{aligned} \quad (\text{C.11})$$

where  $k_s$  is the bulk modulus of solid matrix and  $\mu_s$  is the shear modulus of solid matrix.

Having known that (C.10) and (C.8), the following expression can be calculated:

$$f_p(\mathbb{C}_p - \mathbb{C}_s) : \mathbb{A}_p^{MT} = [s_1, s_2, s_3, s_4, s_5, s_6] \quad (\text{C.12})$$

with

$$\begin{aligned} s_1 &= -[C_{s1} \cdot (b_1 g_1 + 2b_6 g_5) + 2C_{s6} \cdot (b_5 g_1 + b_2 g_5)] \cdot f_p \\ s_2 &= -[C_{s2} \cdot (b_2 g_2 + 2b_5 g_6) + 2C_{s5} \cdot (b_6 g_2 + b_1 g_6)] \cdot f_p \\ s_3 &= -(C_{s3} \cdot b_3 g_3) \cdot f_p \\ s_4 &= -(C_{s4} \cdot b_4 g_4) \cdot f_p \\ s_5 &= -[C_{s5} \cdot (b_1 g_1 + 2b_6 g_5) + C_{s2} \cdot (b_5 g_1 + b_2 g_5)] \cdot f_p \\ s_6 &= -[C_{s6} \cdot (b_2 g_2 + 2b_5 g_6) + C_{s1} \cdot (b_6 g_2 + b_1 g_6)] \cdot f_p \end{aligned} \quad (\text{C.13})$$

According to the homogenization expression (2.11), the effective stiffness tensor by MT scheme can be obtained and expressed by:

$$\mathbb{C}^{MT} = [C_1, C_2, C_3, C_4, C_5, C_6] \quad (\text{C.14})$$

with

$$\begin{aligned} C_1 &= C_{s1} + s_1 \\ C_2 &= C_{s2} + s_2 \\ C_3 &= C_{s3} + s_3 \\ C_4 &= C_{s4} + s_4 \\ C_5 &= C_{s5} + s_5 \\ C_6 &= C_{s6} + s_6 \end{aligned} \quad (\text{C.15})$$

## C.2 The calculation of elastic stiffness tensor of Ponte Castañeda-Willis estimate

Like the part C.1, the concentration tensor need to be calculated at first in this section. We calculate the expression (C.1) :

$$\left(\mathbb{I} - \mathbb{S}^{Esh}\right)^{-1} = [b_1, b_2, b_3, b_4, b_5, b_6] \quad (\text{C.16})$$

where  $b_1, \dots, b_6$  were given in (C.2).

Then it is also easy to calculate the following equation:

$$\mathbb{I} + f_p(\alpha\mathbb{J} + \beta\mathbb{K}) : \left(\mathbb{I} - \mathbb{S}^{Esh}\right)^{-1} = [c_1, c_2, c_3, c_4, c_5, c_6] \quad (\text{C.17})$$

with

$$\begin{aligned} c_1 &= 1 + f_p \left[ \left(\frac{2}{3}\alpha + \frac{1}{3}\beta\right) \cdot b_1 + 2\left(\frac{1}{3}\alpha - \frac{1}{3}\beta\right) \cdot b_5 \right] \\ c_2 &= 1 + f_p \left[ \left(\frac{1}{3}\alpha + \frac{2}{3}\beta\right) \cdot b_2 + 2\left(\frac{1}{3}\alpha - \frac{1}{3}\beta\right) \cdot b_6 \right] \\ c_3 &= 1 + f_p \cdot \beta \cdot b_3 \\ c_4 &= 1 + f_p \cdot \beta \cdot b_4 \\ c_5 &= f_p \left[ \left(\frac{1}{3}\alpha - \frac{1}{3}\beta\right) \cdot b_1 + \left(\frac{1}{3}\alpha + \frac{2}{3}\beta\right) \cdot b_5 \right] \\ c_6 &= f_p \left[ \left(\frac{1}{3}\alpha - \frac{1}{3}\beta\right) \cdot b_2 + \left(\frac{2}{3}\alpha + \frac{1}{3}\beta\right) \cdot b_6 \right] \end{aligned} \quad (\text{C.18})$$

where  $\alpha$  and  $\beta$  have been given in equation (2.33).

The inverse of equation (C.17) is:

$$\left[ \mathbb{I} + f_p(\alpha \mathbb{J} + \beta \mathbb{K}) : \left( \mathbb{I} - \mathbb{S}^{Esh} \right)^{-1} \right]^{-1} = [g_1, g_2, g_3, g_4, g_5, g_6] \quad (\text{C.19})$$

with

$$\begin{aligned} g_1 &= c_2 / (c_1 \cdot c_2 - 2c_5 \cdot c_6) \\ g_2 &= c_1 / (c_1 \cdot c_2 - 2c_5 \cdot c_6) \\ g_3 &= 1/c_3 \\ g_4 &= 1/c_4 \\ g_5 &= -c_5 / (c_1 \cdot c_2 - 2c_5 \cdot c_6) \\ g_6 &= -c_6 / (c_1 \cdot c_2 - 2c_5 \cdot c_6) \end{aligned} \quad (\text{C.20})$$

The strain localization tensor for micropores could be obtained:

$$\mathbb{A}_p^{PCW} = [A_{p1}, A_{p2}, A_{p3}, A_{p4}, A_{p5}, A_{p6}] \quad (\text{C.21})$$

with

$$\begin{aligned} A_{p1} &= b_1 g_1 + 2b_6 g_5 \\ A_{p2} &= b_2 g_2 + 2b_5 g_6 \\ A_{p3} &= b_3 g_3 \\ A_{p4} &= b_4 g_4 \\ A_{p5} &= b_5 g_1 + b_2 g_5 \\ A_{p6} &= b_6 g_2 + b_1 g_6 \end{aligned} \quad (\text{C.22})$$

Then the following expression can be calculated:

$$f_p(\mathbb{C}_p - \mathbb{C}_s) : \mathbb{A}_p^{PCW} = [s_1, s_2, s_3, s_4, s_5, s_6] \quad (\text{C.23})$$

with

$$\begin{aligned} s_1 &= -[C_{s1} \cdot (b_1 g_1 + 2b_6 g_5) + 2C_{s6} \cdot (b_5 g_1 + b_2 g_5)] \cdot f_p \\ s_2 &= -[C_{s2} \cdot (b_2 g_2 + 2b_5 g_6) + 2C_{s5} \cdot (b_6 g_2 + b_1 g_6)] \cdot f_p \\ s_3 &= -(C_{s3} \cdot b_3 g_3) \cdot f_p \\ s_4 &= -(C_{s4} \cdot b_4 g_4) \cdot f_p \\ s_5 &= -[C_{s5} \cdot (b_1 g_1 + 2b_6 g_5) + C_{s2} \cdot (b_5 g_1 + b_2 g_5)] \cdot f_p \\ s_6 &= -[C_{s6} \cdot (b_2 g_2 + 2b_5 g_6) + C_{s1} \cdot (b_6 g_2 + b_1 g_6)] \cdot f_p \end{aligned} \quad (\text{C.24})$$

And the fourth-order stiffness tensor of solid matrix can be written as the following form:

$$\mathbb{C}_s = [C_{s1}, C_{s2}, C_{s3}, C_{s4}, C_{s5}, C_{s6}] \quad (\text{C.25})$$

The effective stiffness tensor can be recast as:

$$\mathbb{C}^{PCW} = [C_1, C_2, C_3, C_4, C_5, C_6] \quad (\text{C.26})$$

with

$$\begin{aligned} C_1^{PCW} &= C_{s1} + s_1 \\ C_2^{PCW} &= C_{s2} + s_2 \\ C_3^{PCW} &= C_{s3} + s_3 \\ C_4^{PCW} &= C_{s4} + s_4 \\ C_5^{PCW} &= C_{s5} + s_5 \\ C_6^{PCW} &= C_{s6} + s_6 \end{aligned} \quad (\text{C.27})$$

### C.3 The calculation of stiffness tensor of Ponte Castañeda-Willis estimate considering damage

The calculated process of stiffness tensor components is shown as follows.

According to the expression of Eshelby tensor (B.2) and Walpole notation, we still need to obtain:

$$\left(\mathbb{I} - \mathbb{S}_p^{Esh}\right)^{-1} = [b_1, b_2, b_3, b_4, b_5, b_6] \quad (\text{C.28})$$

where  $b_1, \dots, b_6$  were given in (C.2).

Then it is also easy to calculate the following equation:

$$\mathbb{I} + f_p(\alpha\mathbb{J} + \beta\mathbb{K}) : \left(\mathbb{I} - \mathbb{S}_p^{Esh}\right)^{-1} = [c_1, c_2, c_3, c_4, c_5, c_6] \quad (\text{C.29})$$

with

$$\begin{aligned}
c_1 &= 1 + f_p \left[ \left( \frac{2}{3}\alpha + \frac{1}{3}\beta \right) \cdot b_1 + 2 \left( \frac{1}{3}\alpha - \frac{1}{3}\beta \right) \cdot b_5 \right] \\
c_2 &= 1 + f_p \left[ \left( \frac{1}{3}\alpha + \frac{2}{3}\beta \right) \cdot b_2 + 2 \left( \frac{1}{3}\alpha - \frac{1}{3}\beta \right) \cdot b_6 \right] \\
c_3 &= 1 + f_p \cdot \beta \cdot b_3 \\
c_4 &= 1 + f_p \cdot \beta \cdot b_4 \\
c_5 &= f_p \left[ \left( \frac{1}{3}\alpha - \frac{1}{3}\beta \right) \cdot b_1 + \left( \frac{1}{3}\alpha + \frac{2}{3}\beta \right) \cdot b_5 \right] \\
c_6 &= f_p \left[ \left( \frac{1}{3}\alpha - \frac{1}{3}\beta \right) \cdot b_2 + \left( \frac{2}{3}\alpha + \frac{1}{3}\beta \right) \cdot b_6 \right]
\end{aligned} \tag{C.30}$$

where  $\alpha$  and  $\beta$  have been given in equation (2.33).

The tensor  $\langle \mathbb{T}' \rangle$  can be expressed by Walpole's notation, as follows:

$$\langle \mathbb{T}' \rangle = [Tp_1, Tp_2, Tp_3, Tp_4, Tp_5, Tp_6] \tag{C.31}$$

with

$$\begin{aligned}
Tp_1 &= \frac{8(1 - \nu_s)}{15\pi(2 - \nu_s)}, & Tp_2 &= \frac{16(1 - \nu_s)}{5\pi(2 - \nu_s)}, & Tp_3 &= \frac{8(1 - \nu_s)}{5\pi(2 - \nu_s)} \\
Tp_4 &= \frac{8(1 - \nu_s)}{5\pi(2 - \nu_s)}, & Tp_5 &= -\frac{8(1 - \nu_s)}{15\pi(2 - \nu_s)}, & Tp_6 &= -\frac{8(1 - \nu_s)}{15\pi(2 - \nu_s)}
\end{aligned} \tag{C.32}$$

The tensor  $\mathbb{M}$  in equation (4.19) can be calculated and expressed by the following expressions:

$$\mathbb{M} = [g_1, g_2, g_3, g_4, g_5, g_6] \tag{C.33}$$

with

$$\begin{aligned}
g_1 &= (c_2 + e_2) / ((c_1 + e_1) \cdot (c_2 + e_2) - 2 \cdot (c_5 + e_5) \cdot (c_6 + e_6)) \\
g_2 &= (c_1 + e_1) / ((c_1 + e_1) \cdot (c_2 + e_2) - 2 \cdot (c_5 + e_5) \cdot (c_6 + e_6)) \\
g_3 &= 1 / (c_3 + e_3) \\
g_4 &= 1 / (c_4 + e_4) \\
g_5 &= -(c_5 + e_5) / ((c_1 + e_1) \cdot (c_2 + e_2) - 2 \cdot (c_5 + e_5) \cdot (c_6 + e_6)) \\
g_6 &= -(c_6 + e_6) / ((c_1 + e_1) \cdot (c_2 + e_2) - 2 \cdot (c_5 + e_5) \cdot (c_6 + e_6))
\end{aligned} \tag{C.34}$$

and

$$\begin{aligned}
e_1 &= \frac{4\pi}{3} \cdot d \cdot \beta \cdot Tp_1, & e_2 &= \frac{4\pi}{3} \cdot d \cdot \beta \cdot Tp_2, & e_3 &= \frac{4\pi}{3} \cdot d \cdot \beta \cdot Tp_3 \\
e_4 &= \frac{4\pi}{3} \cdot d \cdot \beta \cdot Tp_4, & e_5 &= \frac{4\pi}{3} \cdot d \cdot \beta \cdot Tp_5, & e_6 &= \frac{4\pi}{3} \cdot d \cdot \beta \cdot Tp_6
\end{aligned} \tag{C.35}$$

and  $\beta$  has been given in equation (2.33).  
Then we can obtain the following results:

$$f_p(\mathbb{C}_p - \mathbb{C}_s) : \mathbb{A}_p = [s_1, s_2, s_3, s_4, s_5, s_6] \quad (\text{C.36})$$

with

$$\begin{aligned} s_1 &= -[C_{s1} \cdot (b_1g_1 + 2b_6g_5) + 2C_{s6} \cdot (b_5g_1 + b_2g_5)] \cdot f_p \\ s_2 &= -[(C_{s2} \cdot (b_2g_2 + 2b_5g_6) + 2C_{s5} \cdot (b_6g_2 + b_1g_6)] \cdot f_p \\ s_3 &= -(C_{s3} \cdot b_3g_3) \cdot f_p \\ s_4 &= -(C_{s4} \cdot b_4g_4) \cdot f_p \\ s_5 &= -[C_{s5} \cdot (b_1g_1 + 2b_6g_5) + C_{s2} \cdot (b_5g_1 + b_2g_5)] \cdot f_p \\ s_6 &= -[C_{s6} \cdot (b_2g_2 + 2b_5g_6) + C_{s1} \cdot (b_6g_2 + b_1g_6)] \cdot f_p \end{aligned} \quad (\text{C.37})$$

And Walpole's notation of the fourth-order stiffness tensor of solid matrix was given in (C.10). We can have the expression for microcracks:

$$f^c(\mathbb{C}_c - \mathbb{C}_s) : \mathbb{A}_c = [r_1, r_2, r_3, r_4, r_5, r_6] \quad (\text{C.38})$$

with

$$\begin{aligned} r_1 &= -\frac{8}{3}\pi\mu_s \cdot d \cdot (Tp_1 \cdot g_1 + 2 \cdot Tp_6 \cdot g_5) \\ r_2 &= -\frac{8}{3}\pi\mu_s \cdot d \cdot (Tp_2 \cdot g_2 + 2 \cdot Tp_5 \cdot g_6) \\ r_3 &= -\frac{8}{3}\pi\mu_s \cdot d \cdot Tp_3 \cdot g_3 \\ r_4 &= -\frac{8}{3}\pi\mu_s \cdot d \cdot Tp_4 \cdot g_4 \\ r_5 &= -\frac{8}{3}\pi\mu_s \cdot d \cdot (Tp_5 \cdot g_5 + Tp_2 \cdot g_6) \\ r_6 &= -\frac{8}{3}\pi\mu_s \cdot d \cdot (Tp_6 \cdot g_6 + Tp_1 \cdot g_5) \end{aligned}$$

From equation (4.3), the effective stiffness tensor can be written as:

$$\mathbb{C}^{hom} = \mathbb{C}_s + f_p(\mathbb{C}_p - \mathbb{C}_s) : \mathbb{A}_p + f^c(\mathbb{C}_c - \mathbb{C}_s) : \mathbb{A}_c \quad (\text{C.39})$$

Replacing equation (C.36) and (C.38) into (C.39), the fourth-order effective stiffness tensor of fired clay bricks can be represented as:

$$\mathbb{C}^{hom} = [C_1^{pcw}, C_2^{pcw}, C_3^{pcw}, C_4^{pcw}, C_5^{pcw}, C_6^{pcw}] \quad (\text{C.40})$$

with

$$\begin{aligned}C_1^{pcw} &= C_{s1} + s_1 + r_1 \\C_2^{pcw} &= C_{s2} + s_2 + r_2 \\C_3^{pcw} &= C_{s3} + s_3 + r_3 \\C_4^{pcw} &= C_{s4} + s_4 + r_4 \\C_5^{pcw} &= C_{s5} + s_5 + r_5 \\C_6^{pcw} &= C_{s6} + s_6 + r_6\end{aligned}\tag{C.41}$$



# Eshelby's problem in linear thermal conduction

---

## Contents

<b>D.1</b>	<b>The thermal conductivity inclusion problem . . . . .</b>	<b>124</b>
<b>D.2</b>	<b>The second-order hill tensor . . . . .</b>	<b>126</b>
<b>D.3</b>	<b>The inhomogeneity problem . . . . .</b>	<b>127</b>

---

In the above part, the effective thermal conductivity, which is dependent on the thermal conductivities of inclusions and matching localization tensors, has been derived. Now we study Eshelby's problem that contributes to the solutions of the localization problem. We consider a RVE  $\Omega$  composed of a solid phase  $\Omega_s$  and another phase  $\Omega_I$ . The thermal conductivity tensor are denoted by  $\underline{\underline{\lambda}}_s$  and  $\underline{\underline{\lambda}}_I$ , respectively. The boundary of RVE  $\partial\Omega$  is submitted to the macroscopic homogeneous thermal gradient  $\underline{grad}T$ .

$$\left\{ \begin{array}{l} \underline{div}\underline{q}(\underline{x}) = 0 \\ \underline{q}(\underline{x}) = -\underline{\underline{\lambda}}(\underline{x}) \cdot \underline{grad}T(\underline{x}) \quad \text{with} \quad \underline{\underline{\lambda}}(\underline{x}) = \begin{cases} \underline{\underline{\lambda}}_I & \text{for } \underline{x} \in \Omega_I \\ \underline{\underline{\lambda}}_s & \text{for } \underline{x} \in \Omega_s \end{cases} \\ T(\underline{x}) = \underline{grad}T \cdot \underline{x} \quad \forall \underline{x} \in \partial\Omega \end{array} \right. \quad (\text{D.1})$$

The set of equations (D.1) are proposed for a problem in a bounded domain. We can consider an auxiliary problem (so-called Eshelby's Problem) in which a bounded inclusion  $I$  is embedded in an infinite homogeneous medium  $\Omega$ , respectively, corresponding to thermal conductivity tensors  $\underline{\underline{\lambda}}_I$  and  $\underline{\underline{\lambda}}_s$ . The boundary condition of this problem for the infinite medium will be changed. The controlling equations for the inhomogeneity problem are:

$$\left\{ \begin{array}{l} \text{div}\underline{q}(\underline{x}) = 0 \\ \underline{q}(\underline{x}) = -\underline{\lambda}(\underline{x}) \cdot \underline{grad}T(\underline{x}) \quad \text{with} \quad \underline{\lambda}(\underline{x}) = \begin{cases} \underline{\lambda}_I & \text{for } \underline{x} \in I \\ \underline{\lambda}_s & \text{for } \underline{x} \in (\Omega - I) \end{cases} \\ T(\underline{x}) = \underline{grad}T \cdot \underline{x} \quad \text{when} \quad |\underline{x}| \rightarrow \infty \end{array} \right. \quad (\text{D.2})$$

Introducing  $\delta\underline{\lambda} = \underline{\lambda}_I - \underline{\lambda}_s$ , we can have:

$$\underline{q}(\underline{x}) = -\underline{\lambda}_s \cdot \underline{grad}T(\underline{x}) + \underline{q}_f(\underline{x}) \quad (\text{D.3})$$

with

$$\underline{q}_f(\underline{x}) = -\delta\underline{\lambda} \cdot \chi_I(\underline{x})\underline{grad}T(\underline{x}) \quad (\text{D.4})$$

where  $\chi_I(\underline{x})$  is denoted as the characteristic function of the domain  $I$ .

Supposing that  $\underline{q}_f(\underline{x}) = \underline{q}^c \chi_I(\underline{x})$ , where  $\underline{q}^c$  is a constant vector. The problem of inhomogeneity could be written as:

$$\left\{ \begin{array}{l} \text{div}\underline{q}(\underline{x}) = 0 \\ \underline{q}(\underline{x}) = -\underline{\lambda}_s \cdot \underline{grad}T(\underline{x}) + \underline{q}^c \chi_I(\underline{x}) \\ T(\underline{x}) = \underline{grad}T \cdot \underline{x} \quad \text{when} \quad |\underline{x}| \rightarrow \infty \end{array} \right. \quad (\text{D.5})$$

The set of equations (D.5) is named as Eshelby's inclusion problem [55].

## D.1 The thermal conductivity inclusion problem

In this problem, we consider the case of  $\underline{grad}T = 0$ . From (D.5), the following equation is obtained:

$$-\underline{\lambda}_s \cdot \Delta T + \underline{q}^c \cdot \underline{grad}\chi_I = 0 \quad (\text{D.6})$$

$\underline{grad}\chi_I$  involves derivations of a discontinuous function (see [46]). In terms of the definition of the derivative of a distribution, we can have:

$$\langle \underline{grad}\chi_I, \psi \rangle = - \langle \chi_I, \underline{grad}\psi \rangle = - \int_I \underline{grad}\psi dV = - \int_{\partial I} \psi \underline{n} dS \quad (\text{D.7})$$

where  $\psi$  is a function of  $D(\mathbb{R}^3)$  and  $\underline{n}$  is the outward normal unit vector of  $I$ . The Dirac distribution  $\delta_{\partial I}$  connected with the boundary of  $I$  is introduced by:

$$\langle \delta_{\partial I}, \psi \rangle = \int_{\partial I} \psi dS \quad (\text{D.8})$$

From (D.7) and (D.8), we can obtain:

$$\underline{grad}\chi_I = -\underline{n}\delta_{\partial I} \quad (\text{D.9})$$

Then equation (D.6) can be written as:

$$\underline{\lambda}_s \cdot \Delta T + \underline{q}^c \cdot \underline{n}\delta_{\partial I} = 0 \quad (\text{D.10})$$

The solution of (D.10) can be acquired by the Green function  $G(\underline{x})$ , which is defined as the solution of the following equation:

$$\underline{\lambda}_s \cdot \Delta_{\underline{x}} G + \delta_{\underline{x}'} = 0 \quad (\text{D.11})$$

where  $\delta_{\underline{x}'}$  is the Dirac function at  $\underline{x}'$  that is defined by any function  $\psi \in D(\mathbb{R}^3)$ . The solution of (D.11) is [78, 79]:

$$G(\underline{x}, \underline{x}') = \frac{1}{4\pi R\kappa} \quad (\text{D.12})$$

with

$$R = [(\underline{x} - \underline{x}')^T \cdot \underline{\lambda}_s^{-1} \cdot (\underline{x} - \underline{x}')]^{1/2} \quad (\text{D.13})$$

and

$$\kappa = \det \underline{\lambda}_s^{1/2} \quad (\text{D.14})$$

By superposition, we can obtain the solution of (D.10):

$$T = \int_{\partial I} G(\underline{x} - \underline{x}') \underline{q}^c \cdot \underline{n} dS_{\underline{x}'} \quad (\text{D.15})$$

Using the Gauss's theorem:

$$T = -\frac{\partial}{\partial \underline{x}_j} \int_I G(\underline{x} - \underline{x}') \underline{q}_j^c dV_{\underline{x}'} \quad (\text{D.16})$$

It is readily to have another derivation:

$$\frac{\partial T}{\partial x_i}(\underline{x}) = \frac{\partial^2}{\partial x_i \partial x_j} \left( \int_I G(\underline{x} - \underline{x}') dV_{\underline{x}'} \right) \underline{q}_j^c \quad (\text{D.17})$$

The thermal gradient vector can be expressed as:

$$\underline{grad}T = \underline{P}^\epsilon \cdot \underline{q}^c \quad (\text{D.18})$$

with

$$P_{ij}(\underline{x}) = -\frac{\partial^2}{\partial x_i \partial x_j} \int_I G(\underline{x} - \underline{x}') dV_{\underline{x}'} \quad (\text{D.19})$$

The above mentioned derivations are performed under  $\underline{grad}T = 0$ . For the case of  $\underline{grad}T \neq 0$ , we have:

$$\underline{grad}T = \underline{P}^\epsilon \cdot \underline{q}^c + \underline{grad}T \quad (\text{D.20})$$

Supposing that  $\underline{q}^c$  was constant, the solution of Eshelby's problem could be reduced to the calculation of the second-order Hill tensor  $P$ .

## D.2 The second-order hill tensor

In view of the Green function, it is necessary to introduce the potential function  $\Phi(\underline{x})$  relying on the geometry of  $I$ :

$$\Phi(\underline{x}) = \int_I \frac{1}{|\underline{x} - \underline{x}'|} dV_{\underline{x}'} \quad (\text{D.21})$$

Combining (D.12) and (D.19), it yields:

$$P_{ij}(\underline{x}) = -\frac{1}{4\pi\kappa} \frac{\partial^2 \Phi}{\partial x_i \partial x_j}(\underline{x}) \quad (\text{D.22})$$

### D.3 The inhomogeneity problem

Now we turn to the inhomogeneity problem. Recalling equation (D.3) and (D.4):

$$\underline{q}(\underline{x}) = -\underline{\lambda}_s \cdot \underline{grad}T(\underline{x}) + \underline{q}_f(\underline{x}) \quad (\text{D.23})$$

with

$$\underline{q}_f(\underline{x}) = -\delta\underline{\lambda} \cdot \chi_I(\underline{x})\underline{grad}T(\underline{x}) \quad (\text{D.24})$$

The necessary and sufficient condition is that the thermal gradient is uniform in the domain  $I$  so that the inhomogeneity problem is consistent with the inclusion problem. In this instance, The solution of the inhomogeneity problem can be obtained by that of the inclusion problem:

$$\underline{grad}T(\underline{x}) = \underline{P}^\epsilon \cdot \underline{q}_f(\underline{x}) + \underline{grad}T \quad (\text{D.25})$$

with

$$\underline{q}_f(\underline{x}) = -\delta\underline{\lambda} \cdot \underline{grad}T(\underline{x}) \quad (\text{D.26})$$

From above two equations, we can obtain:

$$\underline{q}_f(\underline{x}) = -\delta\underline{\lambda} \cdot (\underline{\delta} + \delta\underline{\lambda} \cdot \underline{P}^\epsilon)^{-1} \cdot \underline{grad}T \quad (\text{D.27})$$

The local thermal gradient vector in the ellipsoidal domain  $I$  is:

$$\underline{grad}T = \underline{A}_I \cdot \underline{grad}T \quad (\text{D.28})$$

where the localization tensor is:

$$\underline{A}_I = [\underline{\delta} + (\underline{\lambda}_I - \underline{\lambda}_s) \cdot \underline{P}^\epsilon]^{-1} \quad (\text{D.29})$$



# Bibliography

- [1] Michel KORNMANN. Matériaux de terre cuite propriétés et produits. *Techniques de l'ingénieur Les matériaux de construction*, 2009.
- [2] Nathalie Domede. Méthode de requalification des ponts en maçonnerie. *Institut National des Sciences Appliquées de Toulouse, LMDC*, 2006.
- [3] Mücahit Sütçü. The use of paper processing residues in the development of ceramics with improved thermal insulation properties. 2010.
- [4] Konrad J Krakowiak, Paulo B Lourenço, and Franz Josef Ulm. Multitechnique investigation of extruded clay brick microstructure. *Journal of the American Ceramic Society*, 94(9):3012–3022, 2011.
- [5] Mucahit Sutcu and Sedat Akkurt. The use of recycled paper processing residues in making porous brick with reduced thermal conductivity. *Ceramics International*, 35(7):2625–2631, 2009.
- [6] Daniel Vitorino de Castro Oliveira. *Experimental and numerical analysis of blocky masonry structures under cyclic loading*. PhD thesis, Universidade do Minho, 2003.
- [7] Laila Aouba, Cécile Bories, Marie Coutand, Bernard Perrin, and Hervé Lemercier. Properties of fired clay bricks with incorporated biomasses: cases of olive stone flour and wheat straw residues. *Construction and Building Materials*, 102:7–13, 2016.
- [8] Michel Kornmann. *Clay bricks and rooftiles, manufacturing and properties*. lasim, 2007.
- [9] P Maillard and JE Aubert. Effects of the anisotropy of extruded earth bricks on their hygrothermal properties. *Construction and Building Materials*, 63:56–61, 2014.
- [10] Daniel Vitorino de Castro Oliveira. *experimental and numerical analysis of blocky masonry structures under cyclic loading*. PhD thesis, Universidade do Minho, 2002.
- [11] Laila Aouba. *Caractérisation et conception de nouveaux matériaux et produits à base de terre cuite et d'agro-ressources*. PhD thesis, Université de Toulouse, Université Toulouse III-Paul Sabatier, 2015.
- [12] Norme Européenne-AFNOR. Maçonnerie et éléments de maçonnerie détermination des valeurs thermiques de calcul nf en 1745. *NF EN 1745*, 2002.

- [13] Mucahit Sutcu. Influence of expanded vermiculite on physical properties and thermal conductivity of clay bricks. *Ceramics International*, 41(2):2819–2827, 2015.
- [14] Pierre-Marie Nigay. *Study of microstructural transformations of clay/biomass mixtures on the firing and relations with the mechanical and thermal properties*. PhD thesis, Ecole des Mines d’Albi-Carmaux, 2015.
- [15] Mucahit Sutcu, Hande Alptekin, Ertugrul Erdogmus, Yusuf Er, and Osman Gencil. Characteristics of fired clay bricks with waste marble powder addition as building materials. *Construction and Building Materials*, 82:1–8, 2015.
- [16] W. D. Nesse. Introduction to mineralogy. *Geological Magazine*, 139(4):491, 2000.
- [17] Giuseppe Cultrone, Eduardo Sebastián, Kerstin Elert, Maria José de la Torre, Olga Cazalla, and Carlos Rodriguez-Navarro. Influence of mineralogy and firing temperature on the porosity of bricks. *Journal of the European Ceramic Society*, 24(3):547 – 564, 2004.
- [18] M.J. Orts, A. Escardino, J.L. Amorós, and F. Negre. Microstructural changes during the firing of stoneware floor tiles. *Applied Clay Science*, 8(2):193 – 205, 1993.
- [19] Magdalena Lassinantti Gualtieri, Alessandro F. Gualtieri, Silvio Gagliardi, Petra Ruffini, Roberto Ferrari, and Miriam Hanuskova. Thermal conductivity of fired clays: Effects of mineralogical and physical properties of the raw materials. *Applied Clay Science*, 49(3):269 – 275, 2010.
- [20] Pedro M Velasco, María Pilar M Ortiz, Manuel Antonio M Giró, Daniel M Melia, and Jorge H Rehbein. Development of sustainable fired clay bricks by adding kindling from vine shoot: Study of thermal and mechanical properties. *Applied Clay Science*, 107:156–164, 2015.
- [21] Cecile Bories, Marie-Elisabeth Borredon, Emeline Vedrenne, and Gerard Vilarem. Development of eco-friendly porous fired clay bricks using pore-forming agents: A review. *Journal of environmental management*, 143:186–196, 2014.
- [22] SP Raut, RV Ralegaonkar, and SA Mandavgane. Development of sustainable construction material using industrial and agricultural solid waste: A review of waste-create bricks. *Construction and building materials*, 25(10):4037–4042, 2011.
- [23] G.W. Carter, A.M. Cannor, and D.S. Mansell. Properties of bricks incorporating unground rice husks. *Building and Environment*, 17(4):285 – 291, 1982.
- [24] J. Sutas, A. Mana, and L. Pitak. Effect of rice husk and rice husk ash to properties of bricks. *Procedia Engineering*, 32:1061 – 1067, 2012.

- [25] Viktor Bánhidi and László A Gömze. Improvement of insulation properties of conventional brick products. In *Materials science forum*, volume 589, pages 1–6. Trans Tech Publ, 2008.
- [26] D. Eliche-Quesada, C. Martínez-García, M.L. Martínez-Cartas, M.T. Cotes-Palomino, L. Pérez-Villarejo, N. Cruz-Pérez, and F.A. Corpas-Iglesias. The use of different forms of waste in the manufacture of ceramic bricks. *Applied Clay Science*, 52(3):270 – 276, 2011.
- [27] R Saiah, B Perrin, and L Rigal. Improvement of thermal properties of fired clays by introduction of vegetable matter, 2010.
- [28] Chih-Huang Weng, Deng-Fong Lin, and Pen-Chi Chiang. Utilization of sludge as brick materials. *Advances in Environmental Research*, 7(3):679 – 685, 2003.
- [29] Winfried Russ, Heinrich MÄürtel, and Roland Meyer-Pittroff. Application of spent grains to increase porosity in bricks. *Construction and Building Materials*, 19(2):117 – 126, 2005.
- [30] Ismail Demir. Effect of organic residues addition on the technological properties of clay bricks. *Waste Management*, 28(3):622 – 627, 2008.
- [31] Giuseppe Cultrone and Eduardo Sebastián. Fly ash addition in clayey materials to improve the quality of solid bricks. *Construction and Building Materials*, 23(2):1178–1184, 2009.
- [32] K Koseoglu, Mehmet Polat, and Hürriyet Polat. Encapsulating fly ash and acidic process waste water in brick structure. *Journal of hazardous materials*, 176(1):957–964, 2010.
- [33] F Saboya, GC Xavier, and J Alexandre. The use of the powder marble by-product to enhance the properties of brick ceramic. *Construction and Building Materials*, 21(10):1950–1960, 2007.
- [34] María Adriana Montero, MM Jordán, MS Hernández-Crespo, and T Sanfeliu. The use of sewage sludge and marble residues in the manufacture of ceramic tile bodies. *Applied Clay Science*, 46(4):404–408, 2009.
- [35] Yüksel Abalı, Mehmet Ali Yurdusev, M Sadrettin Zeybek, and Ahmet Ali Kumanlıođlu. Using phosphogypsume and boron concentrator wastes in light brick production. *Construction and Building Materials*, 21(1):52–56, 2007.
- [36] Kae-Long Lin. The effect of heating temperature of thin film transistor-liquid crystal display (tft-lcd) optical waste glass as a partial substitute partial for clay in eco-brick. *Journal of Cleaner Production*, 15(18):1755–1759, 2007.

- [37] M Dondi, G Guarini, M Raimondo, and C Zanelli. Recycling pc and tv waste glass in clay bricks and roof tiles. *Waste Management*, 29(6):1945–1951, 2009.
- [38] T Uslu and AI Arol. Use of boron waste as an additive in red bricks. *Waste Management*, 24(2):217–220, 2004.
- [39] Romualdo R Menezes, Heber S Ferreira, Gelmires A Neves, Helio de L Lira, and Heber C Ferreira. Use of granite sawing wastes in the production of ceramic bricks and tiles. *Journal of the European Ceramic Society*, 25(7):1149–1158, 2005.
- [40] Yongliang Chen, Yimin Zhang, Tiejun Chen, Yunliang Zhao, and Shenxu Bao. Preparation of eco-friendly construction bricks from hematite tailings. *Construction and Building Materials*, 25(4):2107–2111, 2011.
- [41] G Lu, GQ Max Lu, and ZM Xiao. Mechanical properties of porous materials. *Journal of Porous Materials*, 6(4):359–368, 1999.
- [42] W Hansen and JH Kung. Pore structure and frost durability of clay bricks. *Materials and Structures*, 21(6):443–447, 1988.
- [43] P Muñoz, MP Morales, MA Mendivil, MC Juárez, and L Muñoz. Using of waste pomace from winery industry to improve thermal insulation of fired clay bricks. eco-friendly way of building construction. *Construction and Building Materials*, 71:181–187, 2014.
- [44] ASTM D4404-84. Standard test method for determination of pore volume and pore volume distribution of soil and rock by mercury intrusion porosimetry. *American society for Testing and Materials*, 2004.
- [45] A. Zaoui. *Matériaux hétérogènes et composites: Majeure de Mécanique, option matériaux et structures*. École polytechnique, département de mécanique, 1999.
- [46] L. Dormieux, D. Kondo, and F.J. Ulm. *Microporomechanics*. Wiley, 2006.
- [47] Arthur L Gurson. Continuum theory of ductile rupture by void nucleation and growth: Part i-yield criteria and flow rules for porous ductile media. *Journal of engineering materials and technology*, 99(1):2–15, 1977.
- [48] V. Rzhevsky and G. Novik. The physics of rocks. *Journal of engineering materials and technology*, 1971.
- [49] Eugene Ryshkewitch. Compression strength of porous sintered alumina and zirconia. *Journal of the American Ceramic Society*, 36(2):65–68, 1953.
- [50] S Shima and M Oyane. Plasticity theory for porous metals. *International Journal of Mechanical Sciences*, 18(6):285–291, 1976.

- [51] M.Y. Bal'shin. Relation of mechanical properties of powder metals and their porosity and the ultimate properties of porous metal-ceramic materials. *Doklady Akademii Nauk SSSR*, 67(5):831–834, 1949.
- [52] KK Schiller. Strength of porous materials. *Cement and Concrete Research*, 1(4):419–422, 1971.
- [53] Didericus Hasselman. Griffith flaws and the effect of porosity on tensile strength of brittle ceramics. 52:457–457, 08 1969.
- [54] Salvatore Torquato. *Random heterogeneous materials: microstructure and macroscopic properties*. Springer-Verlag, 2002.
- [55] J.D. Eshelby. The determination of the elastic field of an ellipsoidal inclusion, and related problems. *Proceedings of the Royal Society of London. Series A, Mathematical and Physical Sciences*, 241(1226):376–396, 1957.
- [56] R. Hill. A self-consistent mechanics of composite materials. *Journal of the Mechanics and Physics of Solids*, 13(4):213 – 222, 1965.
- [57] Tanaka Mori and K Tanaka. Average stress in matrix and average elastic energy of materials with misfitting inclusions. *Acta metallurgica*, 21(5):571–574, 1973.
- [58] P Ponte Castañeda and JOHN R Willis. The effect of spatial distribution on the effective behavior of composite materials and cracked media. *Journal of the Mechanics and Physics of Solids*, 43(12):1919–1951, 1995.
- [59] Qi-zhi Zhu, Jian-fu Shao, and Djimedo Kondo. A micromechanics-based non-local anisotropic model for unilateral damage in brittle materials. *Comptes Rendus Mécanique*, 336(3):320–328, 2008.
- [60] GJ Weng. Explicit evaluation of willis' bounds with ellipsoidal inclusions. *International Journal of Engineering Science*, 30(1):83–92, 1992.
- [61] JR Willis. Bounds and self-consistent estimates for the overall properties of anisotropic composites. *Journal of the Mechanics and Physics of Solids*, 25(3):185–202, 1977.
- [62] GK Hu and GJ Weng. Some reflections on the mori-tanaka and ponte castaneda-willis methods with randomly oriented ellipsoidal inclusions. *Acta Mechanica*, 140(1):31–40, 2000.
- [63] L.J. Walpole. Elastic behavior of composite materials: Theoretical foundations. *Advances in Applied Mechanics*, 21:169–242, 1981.
- [64] L. Dormieux and F.J. Ulm. *Applied Micromechanics of Porous Materials*. CISM International Centre for Mechanical Sciences. Springer Vienna, 2007.

- [65] I.M Sobol'. On the distribution of points in a cube and the approximate evaluation of integrals. *USSR Computational Mathematics and Mathematical Physics*, 7(4):86 – 112, 1967.
- [66] John A Nelder and Roger Mead. A simplex method for function minimization. *The computer journal*, 7(4):308–313, 1965.
- [67] Albert Giraud, C Gruescu, DP Do, Françoise Homand, and Djimédo Kondo. Effective thermal conductivity of transversely isotropic media with arbitrary oriented ellipsoidal inhomogeneities. *International Journal of Solids and Structures*, 44(9):2627–2647, 2007.
- [68] DO Duc Phi. *Application des approches d'homogénéisation à l'étude des propriétés thermo-hydro-mécaniques des roches*. PhD thesis, Ecole Nationale Supérieure de Géologie de Nancy, 2008.
- [69] Luc Dormieux and Djimedo Kondo. *Micromechanics of Fracture and Damage*. John Wiley & Sons, 2016.
- [70] Emma Lanoye, Fabrice Cormery, Djimedo Kondo, and Jian-Fu Shao. An isotropic unilateral damage model coupled with frictional sliding for quasi-brittle materials. *Mechanics Research Communications*, 53:31–35, 2013.
- [71] A Abou-Chakra Guéry, Fabrice Cormery, Jian-Fu Shao, and Djimedo Kondo. A micromechanical model of elastoplastic and damage behavior of a cohesive geomaterial. *International Journal of Solids and structures*, 45(5):1406–1429, 2008.
- [72] Vincent Deudé. *Non linéarités géométriques et physiques dans les milieux poreux: apport des méthodes de changement d'échelle*. PhD thesis, Ecole des Ponts ParisTech, 2002.
- [73] Jean-Louis Chaboche. Continuous damage mechanics-a tool to describe phenomena before crack initiation. *Nuclear Engineering and Design*, 64(2):233–247, 1981.
- [74] J.J. Marigo. Modelling of brittle and fatigue damage for elastic material by growth of microvoids. *Engineering Fracture Mechanics*, 21(4):861 – 874, 1985.
- [75] WGRFR Spendley, George R Hext, and Francis R Himsworth. Sequential application of simplex designs in optimisation and evolutionary operation. *Technometrics*, 4(4):441–461, 1962.
- [76] T. Mura. *Micromechanics of Defects in Solids*. Mechanics of Elastic and Inelastic Solids. Springer Netherlands, 1987.

- [77] Qizhi Zhu. *Applications des approches d'homogénéisation à la modélisation tridimensionnelle de l'endommagement des matériaux quasi fragiles : formulations, validations et implémentations numériques*. PhD thesis, 2006. Thèse.
- [78] George B Arfken and Hans J Weber. *Mathematical methods for physicists international student edition*. Academic press, 2005.
- [79] Hsin-Yi Kuo and Tungyang Chen. Steady and transient green's functions for anisotropic conduction in an exponentially graded solid. *International Journal of Solids and Structures*, 42(3):1111 – 1128, 2005.